THE INFLUENCE OF DEFORMATION-INDUCED RESIDUAL STRESSES ON THE POST-FORMING TENSILE STRESS/STRAIN BEHAVIOR OF DUAL-PHASE STEELS

by

Brandon Michael Hance

B.S. Metallurgical Engineering, Illinois Institute of Technology, 1994

M.S. Metallurgical and Materials Engineering, Colorado School of Mines, 1996

Submitted to the Graduate Faculty of the

School of Engineering in partial fulfillment

of the requirements for the degree of

Doctor of Philosophy in Materials Science and Engineering

University of Pittsburgh

2005

UNIVERSITY OF PITTSBURGH

SCHOOL OF ENGINEERING

This dissertation was presented

by

Brandon Michael Hance

It was defended on

September 22, 2005

and was approved by

John A. Barnard, Professor and Department Chairman
Materials Science and Engineering, University of Pittsburgh

Anthony J. DeArdo, Professor
Materials Science and Engineering, University of Pittsburgh

C. Isaac Garcia, Research Professor
Materials Science and Engineering, University of Pittsburgh

Roy D. Marangoni, Associate Professor
Department of Mechanical Engineering, University of Pittsburgh

Henry R. Piehler, Professor
Department of Materials Science and Engineering, Carnegie Mellon University

Dissertation Director: Anthony J. DeArdo, Professor
Materials Science and Engineering, University of Pittsburgh

THE INFLUENCE OF DEFORMATION-INDUCED RESIDUAL STRESSES ON THE POST-FORMING TENSILE STRESS/STRAIN BEHAVIOR OF DUAL-PHASE STEELS

Brandon M. Hance, Ph.D.

University of Pittsburgh, 2005

It was hypothesized that, in dual-phase (DP) steels, strain partitioning between ferrite (α) and martensite (α') during deformation results in a distribution of post-deformation residual stresses that, in turn, affects the subsequent strength, work hardening behavior and formability when the strain path is changed. The post-forming deformation-induced residual stress *state* was expected to depend upon the microstructure, the amount of strain and the prestrain path. The primary objective of this research program was to understand the influence of deformation-induced residual stresses on the post-forming tensile stress/strain behavior of DP steels. Three commercially produced sheet steels were considered in this analysis: 1) a DP steel with approximately 15 vol. % martensite, 2) a conventional high-strength, low-alloy (HSLA) steel, and 3) a conventional, ultra-low-carbon interstitial-free (IF) steel. Samples of each steel were subjected to various prestrain levels in various plane-stress forming modes, including uniaxial tension, plane strain and balanced biaxial stretching.

Neutron diffraction experiments confirmed the presence of large post-forming deformation-induced residual stresses in the ferrite phase of the DP steel. The deformation-induced residual stress state varied systematically with the prestrain mode, where the principal residual stress components are proportional to the principal strain components of the prestrain mode, but opposite in sign. For the first time, and by direct experimental correlation, it was

shown that deformation-induced residual stresses greatly affect the post-forming tensile stress/strain behavior of DP steels. As previously reported in the literature, the formability (residual tensile ductility) of the IF steel and the HSLA steel was adversely affected by strain path changes. The DP steel presents a formability advantage over the conventional IF and HSLA steels, and is expected to be particularly well suited for complex forming operations that involve abrupt strain path changes.

Deformation-induced residual stresses were measured in the IF steel and the HSLA steel; however, the magnitudes of which are such that post-forming tensile stress/strain behavior was not significantly affected. Considering the vast differences in mechanical properties, microstructure, and composition, the IF steel and the HSLA steel showed remarkably similar post-forming tensile stress/strain behavior for all prestrain modes considered.

TABLE OF CONTENTS

LIST OF TABLES

LIST OF FIGURES

ACKNOWLEDGMENTS

I would like to thank my advisors, Professors Anthony J. DeArdo and C. Isaac Garcia, for their guidance and support throughout my research. I also would like to acknowledge Professors J. A Barnard, Roy D. Marangoni and Henry R. Piehler for their contributions as members of my dissertation committee. Your collective insights have been vital to the success of this Ph.D. program.

Thanks also go to the people at the NIST Center for Neutron Research in Gaithersburg, Maryland for their crucial contributions. In particular, I would like to acknowledge Dr. Hank Prask and Dr. Thomas Gnaupel-Herold for running the neutron diffraction experiments that proved to be invaluable support of my hypothesis.

Various people within United States Steel Corporation helped me along the way. Help came in many forms—useful technical references; discussions; a show of flexibility, support and leniency by management; supply of test materials; mechanical testing, sample preparation and metallography assistance; and general encouragement. Specifically I would like to thank the following individuals for their contributions: Mike Bilos, Al Bonfiglio, Jim Calabrese, Joe Defilippi, Bob Fassinger, Joe Gallenstein, Jeff Grimm, Kent Grimm, Dennis Haezebrouck, Dave Hoydick, Chris Ickes, Alex Konieczny, Todd Link, Joe Michalak, Todd Osman, John Paskan, Ed Patula and Don Rensi. Full financial support from United States Steel Corporation is also greatly appreciated.

From the Colorado School of Mines, I would like to thank Professor David Matlock for referring me to Dr. Prask at NIST and Amy Clarke for discussing her TRIP steel X-ray diffraction data with me.

There are a few other people from the University of Pittsburgh MSE Department that were especially important to me on a more personal level. Peter Wray was a constant inspiration to me and helped me stay the course in times of doubt and frustration. I am also truly grateful for my dear friends Meltem and Çağatay Yanar. Finally, I would like to thank my beautiful wife Kıvılcım Önal Hance for her love, encouragement and unremitting patience. I love you, Sweetheart

1.0 INTRODUCTION

Dual-phase steels are a class of high strength, formable steels that evolved from research into high strength, low alloy (HSLA) steels in attempts to increase strength and improve formability. Hayami and Furukawa of Nippon Steel Corporation produced one of the earliest references to dual-phase steels in 1975 (1), where they found that ferrite/martensite microstructures produced by intercritical annealing and sufficiently rapid cooling gave rise to an interesting set of mechanical properties. Some features of Hayami and Furukawa's materials included:

- Low planar anisotropy.
- Higher tensile strengths than their batch-annealed, solution-hardened counterparts of equivalent composition.
- Higher elongation values than other steels at a given tensile strength.
- Low yield strength without a defined yield point (continuous yielding) and a characteristically high initial work hardening rate.

Shortly after Hayami and Furukawa's work was published, a flood of research into these materials emerged as evidenced by several international conferences dedicated to dual-phase steels that took place in the late 1970s and early 1980s (2-5).

The driving force for the application of dual-phase steels today, as it was in the past few decades, is the need to address the worldwide legislation for increased automotive safety and fuel economy standards (6). Dual-phase steels offer an attractive combination of enhanced formability and high strength that allows "down-gaging" (substituting a thinner material for a

certain application) without sacrificing formability or crash energy absorption ability. While many of the composition/ processing/ microstructure/ property relationships of dual-phase steels were extensively studied before the mid-1980s, it was ultimately the perceived variability in composition and mechanical properties (7), and high production cost (8), that depleted the enthusiasm for these materials in the automotive sector. With more recent advances in steelmaking such as ladle metallurgy practices and improved computerized mill feedback control, efficient mass production of hot rolled and cold rolled dual-phase steels with sufficient uniformity is now feasible. With these enablers, and stricter-than-ever automotive environmental and safety government mandates, dual-phase steels are once again being considered for automotive applications where formability and high strength are needed.

The unique mechanical properties of dual-phase steels are closely related to their work hardening characteristics, which are in turn controlled by microstructure. Speich and Miller (9), among others, have shown that the tensile strength and the work hardening rate increase as the martensite content or the carbon content (hardness) of the martensite increases. Balliger and Gladman (10) found that, for a given strength level (*i.e.*, a given martensite content), the work hardening rate increases as the average martensite "island" size decreases. The initially high work hardening rate and continuous yielding behavior are attributed to high ferrite mobile dislocation density near ferrite/martensite boundaries and residual stresses caused by the volume expansion of the intercritical austenite during the austenite-to-martensite transformation (9, 11).

Dual-phase steels also exhibit a relatively large Bauschinger Effect when uniaxial tension is followed by uniaxial compression, for example (12, 13). Also, large deformation-induced residual stresses—approaching the magnitude of the original yield strength before forming—have been measured after straining along various strain paths for dual-phase steels and other

multi-phase steels (14, 15). These deformation-induced residual stresses are attributed to strain partitioning between relatively hard and soft microconstituents (martensite and ferrite, respectively). The residual stress state depends upon the deformation mode (strain path) and increases with increasing prestrain (14). The magnitude of the strain partitioning-induced residual stresses is likely to depend upon the volume fraction and distribution of martensite (16).

For efficient and effective application of dual-phase steels, it is important to understand the evolution of strength along various strain paths and the effects of strain path changes on formability in multi-stage forming processes such as tube hydroforming, where abrupt strain path changes are inherent to the process. Accurate prediction of formability, final part strength and springback depends not only upon the effectiveness of computer simulation codes, but also upon the constitutive relations used to describe material behavior.

The effects of strain path on formability of conventional low-carbon steels have been extensively studied, but a knowledge base for dual-phase steel (and other multi-phase steels) has not been established. It is anticipated that deformation-induced residual stresses affect the work hardening behavior and associated formability of dual-phase steels in complex strain paths (*i.e.*, with at least one strain path change), and that dual-phase steels will behave unlike conventional steels under such conditions. In support of this hypothesis, a review of pertinent historical and recent literature is given in the following Background (Section 2.0).

2.0 BACKGROUND

2.1 CHARACTERISTICS OF DP STEELS

Dual-phase (DP) steels may be produced by a variety of processing routes including continuous annealing, hot rolling and batch annealing. Table I shows the approximate cooling rates and corresponding alloying additions for each process (18).

Table I: Possible Processing Routes for Dual-phase Steels (18).

Details	CAL*	CGL**	Hot Rolling	Batch Annealing
Cooling Type	Water Quench	Gas Quench	Coil Cooled	Furnace Cooled
Cooling Rate	> 2000°C/sec	10-30 °C/sec	~0.1 °C/sec	~0.01 °C/sec
Typical Additions	0.5 Mn, 0.25 Si (+P)	1.5 Mn, 0.5 Si (+Cr/V/Nb/Mo)	1.0 Mn, 1.4 Si, 0.6 Cr, 0.4 Mo	2.5 Mn, 0.5 Si

CAL = continuous annealing line; CGL = continuous galvanizing line

Exact processing conditions and carbon and alloy contents depend on the desired strength level and mill capabilities. Generally, as the expected cooling rate from the intercritical temperature decreases, the alloy content (*e.g.*, Mn, Si, Cr, Mo, *etc*.) must be increased to achieve martensite in the final product. A critical review of the composition/ processing/ microstructure/ property relationships of dual-phase steels is beyond the scope of this review; however several key microstructure/mechanical behavior relationships will be discussed in detail, with appropriate references to composition and processing where applicable. To begin, two distinct

mechanical behavior characteristics of dual-phase steels will be discussed—continuous yielding behavior and high initial work hardening rate.

2.1.1 **Continuous Yielding Behavior**

Hansen and Pradhan (19) explained that three criteria are necessary for a material to exhibit discontinuous yielding behavior: 1) low density of mobile dislocations prior to deformation, 2) rapid dislocation multiplication during deformation, and 3) significant dependence of dislocation velocity on the applied stress. They reasoned that bcc ferrite satisfies conditions 2 and 3, and that a high mobile dislocation density must be responsible for the continuous yielding behavior that was characteristic of DP steels. Hahn (20) predicted for bcc metals that mobile dislocation densities of 10^2-10^4-cm^{-2} lead to discontinuous yielding, while mobile dislocation densities in the range 10^6-10^8-cm^{-2} result in continuous flow. Although total dislocation densities are often in this range for typical hot rolled or annealed steels, Cottrell (21) explained that most of these dislocations are immobile, and Rashid (22) postulated that a high degree of mobile dislocations was introduced by the austenite-to-martensite transformation during DP steel production. More on the ferrite dislocation density of DP steels is given in Section 2.2.2.

Gerbase *et al.* (18) believed that residual stresses caused by the volume expansion of austenite during the transformation to martensite are chiefly responsible for the continuous yielding behavior of DP steels. They surmised that these residual stresses play a significant role in controlling DP steel flow behavior up to strains of the order of 5 pct. They proposed a simple model where the yield strength in the absence of transformation-induced residual stresses, σ_Y is reduced to a flow stress, σ_f by the presence of transformation-induced residual stresses, as

$$\sigma_f = \sigma_Y - f\sigma_R, \qquad [1]$$

where f is volume fraction of material subject to the residual stress, and σ_R is an effective residual stress term (a positive value). By assuming arbitrarily that f varies with imposed strain, ε such that

$$f = f_O \exp(-A\varepsilon), \quad [2]$$

a function of the form

$$\sigma_f = \sigma_Y - \sigma_R f_O \exp(-A\varepsilon), \quad [3]$$

is obtained, where A is a decay constant. Figure 1 shows a schematic diagram that illustrates the effect of the decaying residual stress effect (rounding of the yield point) in reference to an ideal elastic, perfectly plastic material.

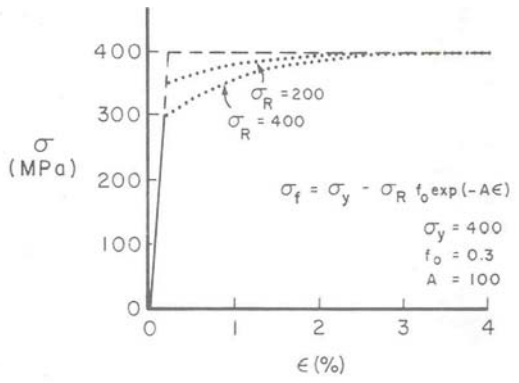

Figure 1: Schematic diagram showing the rounding of the yield point in DP steels due to non-homogeneous deformation of ferrite grains, containing transformation-induced residual stresses, and a gradual decrease with strain of the number of grains containing the residual stress (18).

Crawley *et al*. (23) argued against the speculation of Gerbase *et al*. and concluded, based on calculations of internal stresses in DP steels, that residual stresses are not large enough to lower the effective yield stress, but rather generate mobile dislocations in ferrite adjacent to martensite particles. Speich (24) summarized his understanding of the yielding behavior of DP steels as a combined effect of high mobile dislocation density *and* high residual stresses caused

by the volume expansion of austenite during the transformation to martensite upon cooling from the intercritical temperature. Since plastic flow begins at low strains and applied stresses, and at many sites throughout the specimen, discontinuous yielding is suppressed.

Regardless of the contributions of each proposed mechanism, continuous yielding is certainly a distinct and important feature of DP steels. Hansen and Pradhan (19) showed that, as the cooling rate from the intercritical annealing temperature is increased (*i.e.*, more martensite is formed), the tensile strength increases and the total elongation decreases. As an example, Figure 2 shows stress/strain curves for a 0.11 C, 1.50 Mn, 1.17 Si (wt pct) steel that was intercritically annealed at 815°C for 1 min and cooled at rates ranging from air cooling (5°C/sec) to water quenching (833°C/sec) (19). For this composition, a critical cooling rate around 12°C/sec is reported, where the yield strength is at a minimum, the uniform elongation is at a maximum, and there is a transition from discontinuous to continuous yielding. In addition to the continuous yielding behavior at high cooling rates in Figure 2, note that the initial work hardening rate (slope of stress-strain curve) increases as the cooling rate increases.

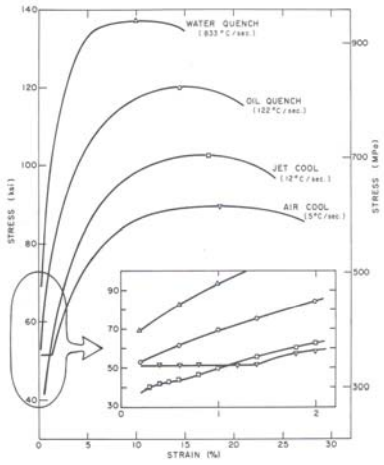

Figure 2: Stress-strain curves for a 0.11 C, 1.50 Mn, 1.17 Si (wt pct) steel that was intercritically annealed at 815°C for 1 min and cooled at the indicated rates (19).

2.1.2 **High Work Hardening Rate and Improved Formability**

Rashid (22) was perhaps the first to illustrate the remarkably high work hardening rates of dual-phase steels in the context of formability in reference to conventional high strength steels. Figure 3 shows a classic series of stress-strain curves from Rashid's work, where a plain carbon steel, two conventional high strength steels (SAE 950X and SAE 980X), and a dual-phase steel (GM 980X) are represented. In Figure 3, SAE 950X and SAE 980X are ferrite/pearlite steels with nominal yield strengths of 50-ksi and 80-ksi respectively, and GM 980X is a version of SAE 980X that has been heat-treated to produce a dual-phase microstructure (intercritically annealed and rapidly cooled). It is clear that the heat-treated version of SAE 980X (*i.e.*, GM 980X) exhibits a much higher initial work hardening rate, lower initial flow stress, and higher uniform and total elongation—at the same approximate ultimate tensile strength level.

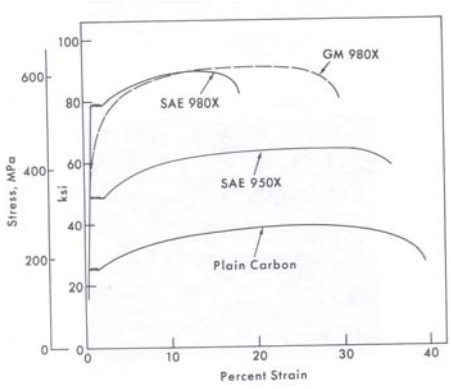

Figure 3: Nominal (engineering) stress-strain curves for a plain carbon steel, two conventional ferrite-carbide steels (SAE 950X and SAE 980X), and a dual-phase steel (GM 980X) produced by heat treating the SAE 980X material (22).

Rashid (22) also introduced the concept of instantaneous n-value (n_i) or incremental work hardening exponent, where n_i is the instantaneous slope of the $\log\sigma$-$\log\varepsilon$ curve (in contrast to the average slope of the $\log\sigma$-$\log\varepsilon$ curve in the conventional definition of n-value). Figure 4 shows

the variation of the n_i-value with plastic strain, ε_p for the as-produced Grade 980X shown in Figure 3, along with several variations of Grade GM 980X (dual-phase) cooled at various rates from the intercritical temperature. Rashid noted that the n_i-value is a relatively stable function of strain for the as-produced Grade SAE 980X; however, n_i varies substantially for the heat treated dual-phase versions. For dual-phase (DP) steels, n_i decreases rapidly as a function of strain after an initial peak. The representation shown in Figure 4 illustrates the basic relationship between work hardening behavior and uniform elongation, where the end of uniform elongation is marked by the intersection of the n_i curve and the line $n_i=\varepsilon_p$ (derived from the condition that $d\sigma/d\varepsilon = \sigma$ at necking). Rashid summarized his findings as follows:

- The heat-treated, dual-phase versions of SAE 980X have significantly higher work hardening coefficients than the non-heat-treated SAE 980X materials over the entire uniform elongation range.
- The true stress-strain curves of DP steels cannot be approximated by the power law ($\sigma=K\varepsilon^n$), while those of conventional ferrite-carbide steels can.

Use of the n-value as a measure of work hardening rate can be misleading. By virtue of the functional form of the power law, the n-value will decrease as strength increases, even if the work hardening rate ($d\sigma/d\varepsilon$) is the same. Davies and Magee (25) discussed the work hardening rates of dual-phase steels in contrast to other high strength steels. They clarified that superior strength/ductility combinations must imply superior work hardening characteristics, especially near instability (diffuse necking) where the true stress equals the work hardening rate. Davies and Magee revealed several important aspects of the work hardening behavior of DP steel in their research:

- In contrast to conventional high strength steels, DP steels show higher work hardening rates at all strains by approximately a factor of two.
- The n-value is physically meaningless in evaluating work hardening behavior, and the work hardening behavior (in terms of work hardening rates) of seemingly very different DP steels is experimentally indistinguishable.
- The wide range of conventional steels shows a degree of variation in work hardening behavior, but all fall in a band that is well below that of dual-phase steels.
- The work hardening rates of dual-phase steels and conventional steels show a similar dependence with strain, and do not immediately suggest different work hardening mechanisms.

The essence of the findings of Davies and Magee is summarized in Figure 5 (25), where the strain hardening rate and true stress are plotted vs. strain for various low-carbon steels and dual-phase steels. They emphasize that the improved strength-ductility balance of DP steels is a direct result of increased work hardening rates throughout deformation. They also mentioned that, if the work hardening rates at higher strains could be improved, ductility could be further enhanced. Davies and Magee compiled a group of ductility and strength data that showed the advantageous strength-ductility balance of DP steels in contrast to other high strength steels. Their compilation is shown in Figure 6 as a plot of tensile strength vs. pct total elongation (25) for various types of high strength steel.

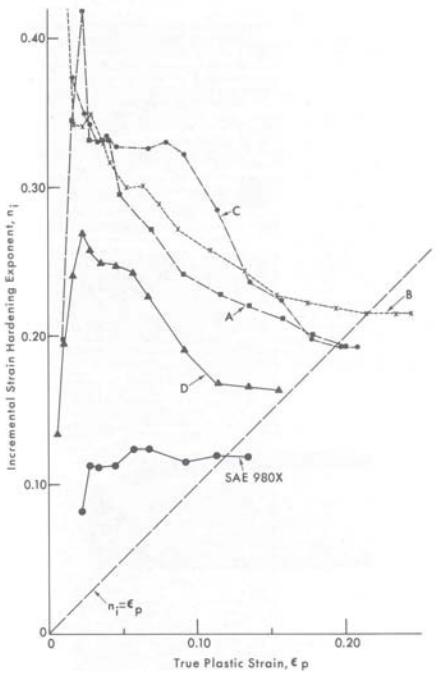

Figure 4: Variation of n_i with ε_p in as-received and heat treated Grade SAE 980X specimens. The intersection of the dotted line and the curves marks the onset of diffuse necking for each condition. SAE 980X is a ferrite-carbide high strength steel, and A through D are dual-phase steels (Grade GM 980X) cooled at rates ranging from 5 to 14°C/sec (increasing from A to D) (22).

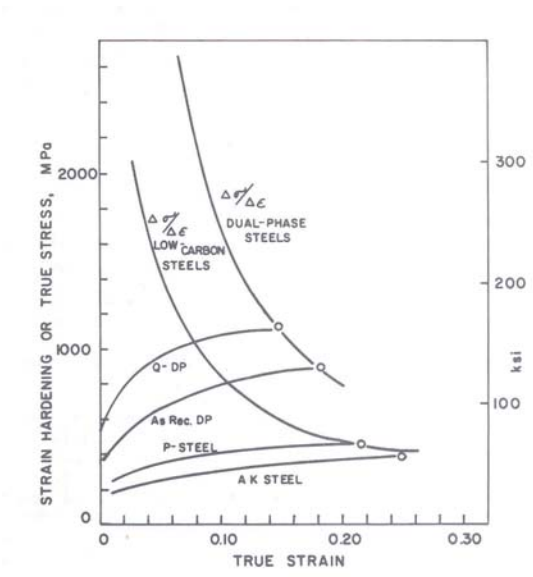

Figure 5: Strain hardening rate and true stress a function of strain for both DP and low-carbon steels. Circles indicate the end of uniform elongation ($\sigma = d\sigma/d\varepsilon$) (25).

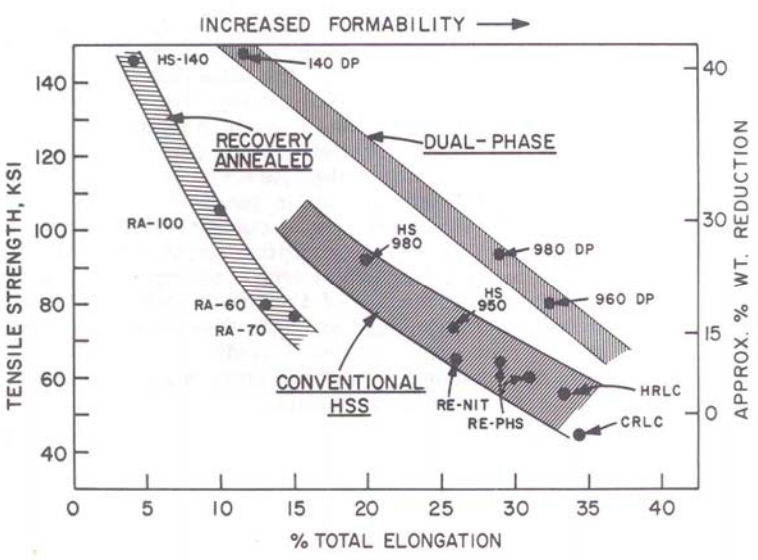

Figure 6: Total elongation as a function of ultimate tensile strength for some commercially available high strength steels. Approximate weight reduction capability was calculated under the assumption that base metal fatigue resistance is the controlling factor (25).

Speich (24) summarized the work of several other researchers (11, 18, 26) that developed an understanding of the various stages of work hardening behavior and helped explain the observation of Rashid (22) that DP steels cannot be described by the simple power law relationship for the entire stress-strain curve. The three stages of work hardening observed for dual-phase steels in uniaxial tensile tests are as follows.

- Stage I – (~0.1 to 0.5 pct strain): Rapid work hardening caused by the elimination of residual stresses and rapid build up of "back stresses" in the ferrite caused by "plastic incompatibility" between α and α' (ferrite and martensite).
- Stage II – (~0.5 to 4 pct strain): The work hardening rate of ferrite is reduced as the plastic flow of ferrite is constrained by the hard, non-deforming martensite particles.

- Stage III – (> 4 pct strain): Dislocation cell structures are formed and further deformation of the ferrite is governed by dynamic recovery and cross-slip and by eventual yielding of the martensite phase.

An example from the work of Cribb and Rigsbee (27) is shown in Figure 7, where the three stages of DP steel work hardening behavior are shown in various ways. Figure 7a shows a true stress-strain curve; Figure 7b shows the non-linearity of the $\log\sigma$-$\log\varepsilon_p$ curve (varying n-value); Figure 7c shows the $\log(d\sigma/d\varepsilon_p)$-$\log\varepsilon_p$, plot (Jaoult-Crussard plot); and Figure 7d shows the $\log(d\sigma/d\varepsilon_p)$-$\log\sigma$ plot that illustrates the onset of diffuse necking ($\sigma = d\sigma/d\varepsilon_p$).

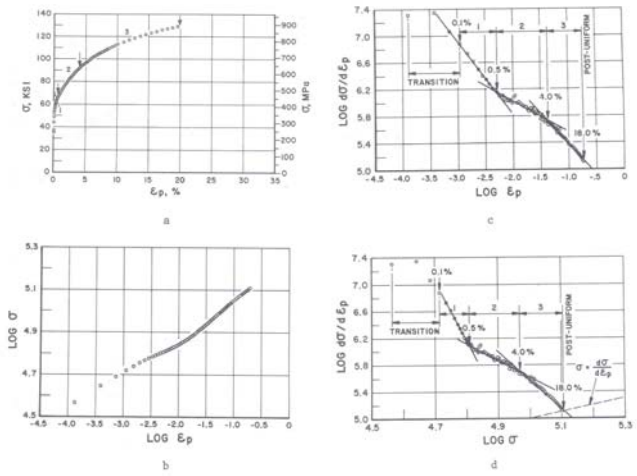

Figure 7: Example of the work hardening behavior of a dual-phase steel. The three stages of work hardening are shown in various ways. A) true stress-strain, σ-ε curve, B) $\log\sigma$-$\log\varepsilon_p$ curve (note the non-linearity), C) Jaoult-Crussard Plot, or $\log(d\sigma/d\varepsilon_p)$-$\log\varepsilon_p$, and D) $\log(d\sigma/d\varepsilon_p)$-$\log\sigma$ (27).

2.2 MICROSTRUCTURAL ASPECTS OF DP STEELS

Dual-phase (DP) steels are a class of high-strength low-alloy (HSLA) steels with microstructures that consist primarily of a dispersion of hard martensite (α') in a soft, ductile ferrite (α) matrix.

Although the term "dual-phase" refers to the two primary microconstituents (α and α'), small amounts of bainite, pearlite and retained austenite may be present (24). The two primary methods of producing DP steels (controlled hot rolling and intercritical annealing) result in inherently different dual-phase microstructures. With the intercritical annealing method, the steel is generally heated to an intercritical temperature (both α and γ are stable), held for some time to form the desired amount of austenite, then subsequently cooled rapidly (quenched) to convert the intercritical austenite to martensite. During the intercritical anneal, austenite nucleates and grows primarily at ferrite grain boundaries, and a microstructure similar to that shown in Figure 8 is obtained (24). Note that the martensite islands (light grey) are much smaller than the ferrite grains (dark grey), and that the martensite islands are situated at the ferrite grain boundaries.

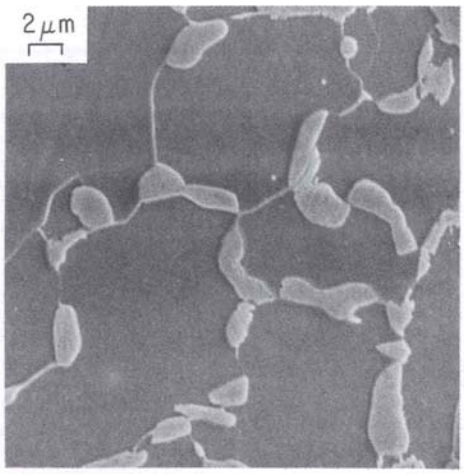

Figure 8: Typical intercritically-annealed dual-phase (α-α') microstructure. (0.06 wt pct C, 1.5 wt pct Mn, water quenched from 760°C) (24).

Repas (28) gave an example of a continuous-cooling-transformation (CCT) diagram for a dual-phase steel—reproduced in Figure 9. To achieve a dual-phase microstructure in a hot rolled

steel, the steel must be cooled sufficiently fast to the coiling temperature to avoid the formation of significant amounts of pearlite, yet slow enough to pass through the ferrite region of the CCT curve. At the appropriate coiling temperature, no additional ferrite will form after coiling, and martensite and bainite will form upon further cooling in the coiled state. The difference between hot rolled and intercritically annealed DP steels is thus the order of phase transformations. Unlike the intercritical case discussed above, ferrite must nucleate and grow in austenite until the desired amount of austenite is *left* in the two-phase, high-temperature microstructure. Once the remaining austenite has transformed to martensite upon cooling, a distinctly different dual-phase microstructure is obtained (in contrast to the intercritically annealed example in Figure 8), where the martensite islands are on the order of the ferrite grain size and are more homogeneously distributed (not concentrated at ferrite grain boundaries). Figure 10 gives examples of hot rolled DP steels with various amounts of martensite (29). A formalized description of two-phase microstructures, given in the next section, helps to define the microstructural distinctions between intercritically annealed and hot rolled DP steels.

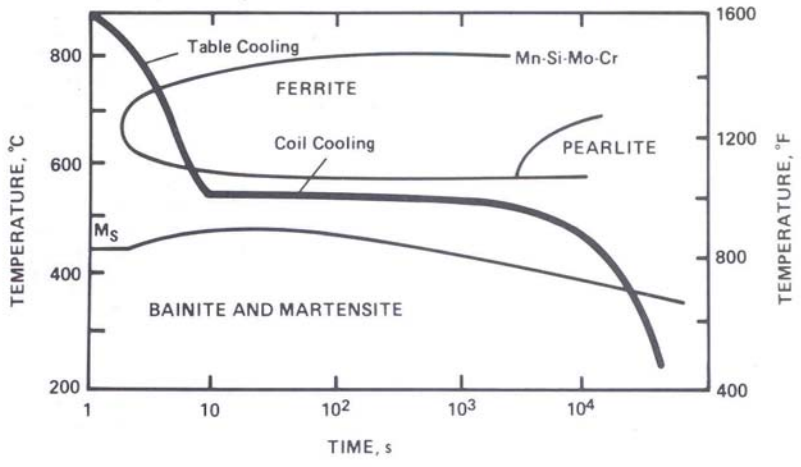

Figure 9: Continuous-cooling transformation behavior in Mn-Si-Mo-Cr steel resulting in a dual-phase microstructure in the as-hot-rolled product (28).

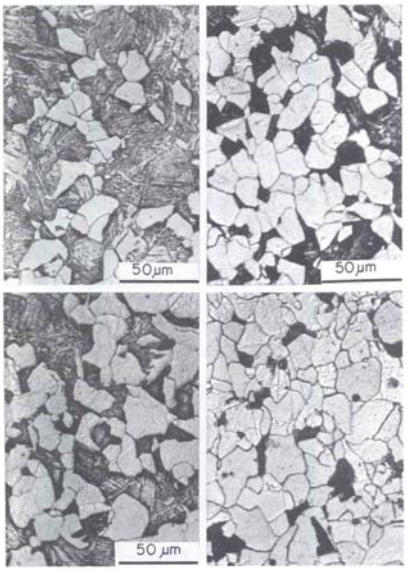

Figure 10: Examples of hot rolled dual-phase steels with different amounts of martensite. Top Left—65 pct martensite, Bottom Left—50 pct martensite, Top Right—35 pct martensite, and Bottom Right—18 pct martensite (29).

2.2.1 **Classification of Two-Phase Microstructures**

Becker *et al*. (30-31) have devised a system whereby two-phase microstructures may be qualitatively described and classified. A complete description in their classification system requires knowledge of the densities of the various types of grain and phase boundaries (*i.e.*, α-α, α'-α' and α-α'), the relative volume fractions (*i.e.*, $f_v\alpha + f_v\alpha' = 1$), and relative grain or island sizes [*i.e.*, d(α) and d(α')]. Figure 11 shows a schematic representation of the basic two-phase microstructures in the classification system developed by Becker *et al*. (31), where the dark phase is martensite (α'), and the light phase is ferrite (α). A dispersion structure has no α'-α' boundaries and consists of a dispersion of α' islands in an α matrix, regardless of the relative volume fractions. An ideal duplex structure has the following characteristics: 1) equal amounts of α-α and α'-α' grain boundaries, 2) equal volume fractions of ferrite and martensite ($f_v\alpha = f_v\alpha' = 0.5$), and 3) the ferrite grain size and the martensite island size are equivalent [d(α) =

d(α')]. A net or network structure has no α-α boundaries and consists of α' surrounding α with the α-α grain boundaries replaced by α-α' phase boundaries.

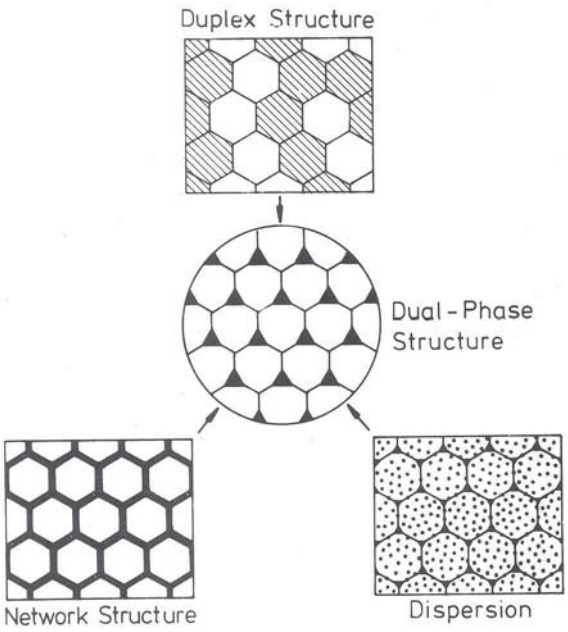

Figure 11: Schematic representation of basic two-phase microstructures (31). For dual-phase steels, the black or shaded regions are martensite, and the white regions are ferrite.

A "dual-phase" microstructure can be defined in the context of the three basic types of two-phase microstructures described above by Becker *et al*. (31). Like a duplex structure, an *ideal* dual-phase structure has the same number of α and α' grains (islands) per unit volume (not true in all real cases, see Figure 8 and Figure 10). Like a dispersion structure, α' islands in a dual-phase steel are completely surrounded by α. At a maximum martensite volume fraction, $f_v(\alpha')$ of 0.3, α'-α' boundaries begin to form (called "percolation"), and at $f_v(\alpha') = 0.5$, an ideal duplex microstructure is formed. Like a network structure, all of the martensite islands in a dual-phase structure are connected by α-α grain boundaries.

Becker *et al*. (30) also defined a parameter $\delta = C_{\alpha\text{-}\alpha'}/C_{\alpha\text{-}\alpha}$ that describes the degree of dispersivity of a dispersion structure, where $C_{\alpha\text{-}\alpha'}$ and $C_{\alpha\text{-}\alpha}$ are the concentrations of ferrite-martensite and ferrite-ferrite boundaries, respectively. Figure 12 shows the effects of δ on the dispersion of martensite islands in a two-phase microstructure. The intercritically annealed specimen in Figure 8 appears to have a higher δ-ratio than the hot rolled specimens shown in Figure 10. Thus, in the classification system of Becker *et al.*, intercritically annealed DP steels may be classified as a fine dispersion that approaches a network structure as martensite content increases, while hot rolled DP steels may be classified as a coarse dispersion that approaches a duplex structure as martensite content increases.

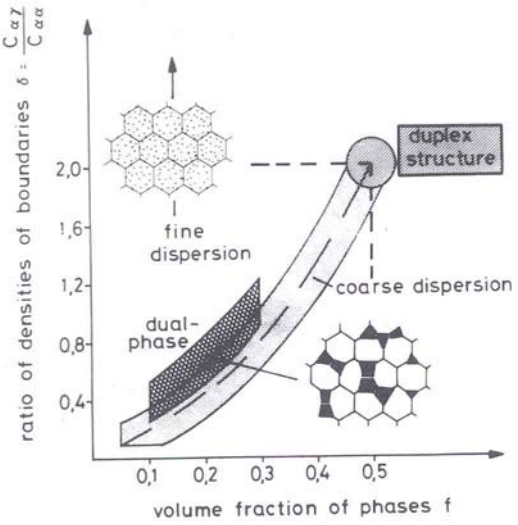

Figure 12: Characterization of different types of two-phase microstructures. In this schematic, α is the ferrite phase as normal, and γ is the martensite phase (*not* austenite) (30).

2.2.2 **Ferrite Dislocation Density of Dual-phase Steels**

As discussed above in Section 2.1.1, DP steels are characterized by high ferrite mobile dislocation density, and this microstructural feature is arguably largely responsible for the

characteristic continuous yielding behavior. Various authors have shown examples of high ferrite dislocation density near ferrite/martensite boundaries in transmission electron microscope analyses (11, 23, 32-34). A particularly illustrative example from the work of Rigsbee *et al*. (34) is given in Figure 13 for a hot rolled dual-phase steel. The dislocation density is relatively low in the ferrite grain interiors and near ferrite/ferrite grain boundaries; however, the ferrite dislocation density is very high near the ferrite/martensite phase boundary.

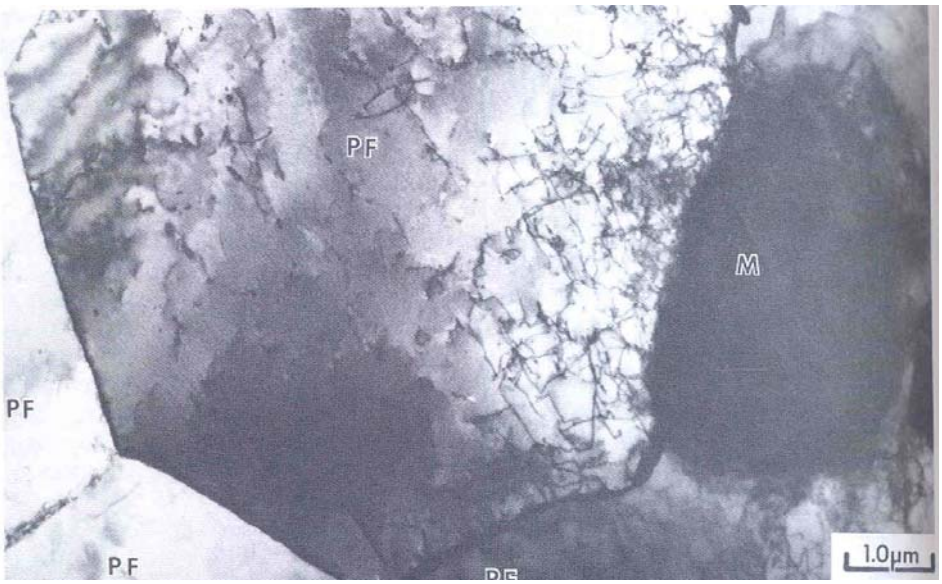

Figure 13: Transmission electron bright field micrograph of a hot rolled dual-phase steel [0.07 C, 0.9 Mn, 1.2 Si, 0.6 Cr, 0.3 Mo (wt pct)]. Note the relatively low dislocation density in the polygonal ferrite (PF) grains and the relatively high ferrite dislocation density near the ferrite/martensite (M) boundary (34).

Sherman *et al*. (32) examined the influence of deformation and martensite content on the ferrite dislocation density of DP steels. They showed that the average ferrite dislocation density increased approximately linearly as a function of martensite content in samples that were quenched from various intercritical annealing temperatures (martensite contents ranging from 16 to 60 pct by volume). The reported dislocation densities ranged from about 0.25×10^{9}-cm^{-2} to

about $1.5x10^{9}$-cm^{-2} in the as-cooled condition. An equivalent set of samples was subjected to 7-pct tensile deformation, and the ferrite dislocation densities increased by a factor between 25 and 40, where dislocation densities between about $1.8x10^{10}$-cm^{-2} and $3.5x10^{10}$-cm^{-2} were reported. In the 7-pct-strain condition, the average ferrite dislocation density is again a nearly linear function of the martensite content. These results are shown graphically in Figure 14 (32). Sherman *et al*. explained that, since the increase in the dislocation density (after 7 pct strain) is higher for larger martensite contents, the partitioning of plastic strain to the ferrite phase increases as martensite content increases.

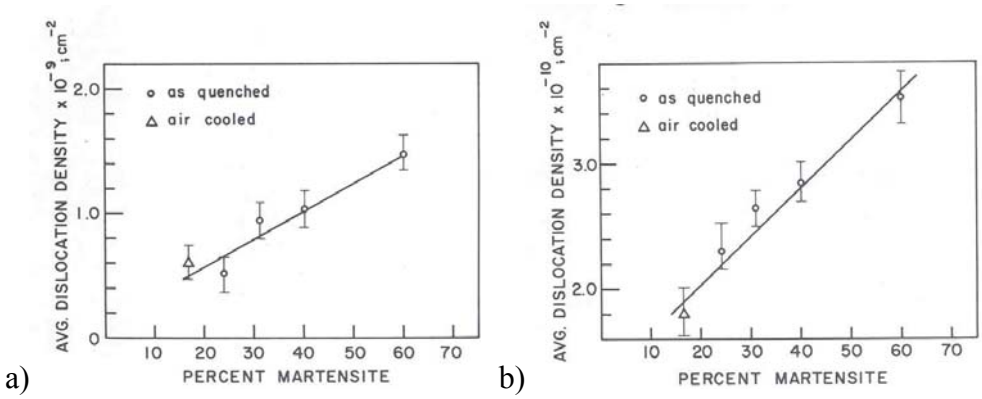

Figure 14: The dislocation density, measured in the ferrite phase, of dual-phase steels as a function of martensite content: a) as cooled from an intercritical temperature, b) after 7 pct tensile deformation [0.11 C, 1.4 Mn, 0.5 Si, 0.08 V (wt pct)] (32).

2.2.3 **Note on Retained Austenite in DP Steels**

Retained austenite may be present in dual-phase steels (less than 10 volume pct) as a result of the incomplete transformation of intercritical austenite to martensite (24). In the early days of DP steel development some researchers argued that retained austenite was necessary to achieve the properties characteristic of dual-phase steels. In fact, Marder (35) concluded from his studies that "…the intercritical annealing treatment must produce a sufficient amount of retained

austenite in the martensite patches in order to obtain the strength-ductility-work hardening relationships necessary for 'dual-phase' alloys." Marder was likely alluding to the transformation-induced plasticity (TRIP) mechanism, whereby retained austenite transforms to martensite during plastic deformation and enhances the work hardening characteristics of the alloy. Today, "TRIP steels" are a separate class of "advanced high strength steels" that optimize the TRIP mechanism for increased formability at high strength levels (36). It is now generally recognized that the transformation of retained austenite to martensite during plastic deformation of DP steels is not an important consideration for work hardening behavior and ductility because of the small volume fractions in "typical" DP steel microstructures (~2 to 4 pct) (9). The factors that control the amount and stability (*i.e.*, against the martensite transformation) of retained austenite are numerous and complex, and beyond the scope of this review. However, it is recognized that increased cooling rate from the intercritical annealing temperature, decreased intercritical annealing temperature, and decreased carbon content all reduce the amount of retained austenite in dual-phase steels (24, 26).

2.3 MICROSTRUCTURE/PROPERTY RELATIONSHIPS IN DP STEELS

Generally for dual-phase steels, as the volume fraction of martensite increases, strength increases and ductility decreases. The exact microstructure/property relationships depend upon various factors including composition, processing history, and martensite volume fraction and distribution. In the following Sections 2.3.1 and 2.3.2 the various empirical microstructural effects on strength and ductility will be discussed for dual-phase steels.

2.3.1 **Correlation between Microstructure and Strength**

Davies and Magee (25) illustrated that the strength (yield strength and ultimate tensile strength) of dual-phase steels is an effectively linear function of martensite content. This relationship is shown in Figure 15 for a series of Fe-Mn-C alloys that were intercritically annealed at temperatures between 730°C and 840°C to create a range of martensite contents from about 5 pct to 95 pct. The 0.2 pct offset flow stress ranged from about 200 to 1000-MPa, while the ultimate tensile strength ranged from about 400 to 1800-MPa. Similar relationships were established by various other researchers (27, 37-39). Tseng and Vitovec (38) showed an interesting representation of the evolution of flow stress with strain for a series of dual-phase steels with martensite concentrations between 20 and 90 pct. Figure 16 shows this representation, where the flow stress, at various strain values also varies linearly with the martensite content. Also evident in Figure 16 is that the majority of the work hardening potential of their materials was achieved at 2 pct strain. Additionally, the total work hardening potential [the difference between the UTS and the elastic limit (σ_p in Figure 16)] increases as the volume fraction of martensite increases.

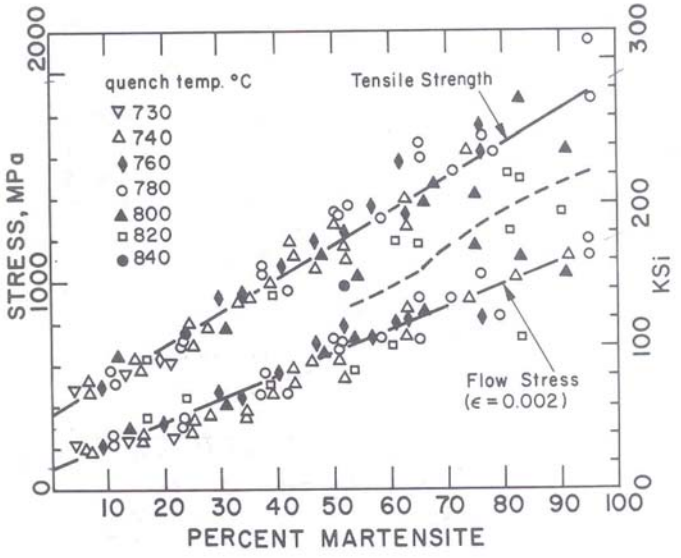

Figure 15: The 0.2 pct offset flow stress and ultimate tensile strength as a function of percent martensite for a series of Fe-Mn-C alloys (25).

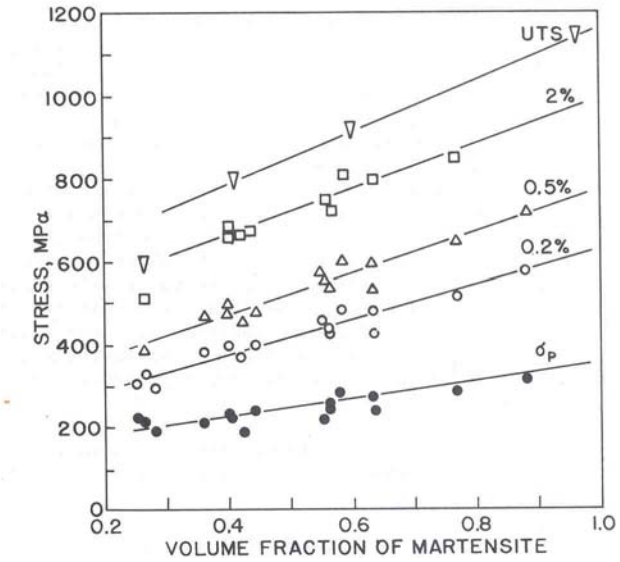

Figure 16: Flow stress at various strains as a function of the volume fraction of martensite (38) in a dual-phase steel. Specimens were intercritically annealed at temperatures between 730°C and 865°C for 30 minutes and water quenched. Composition: 0.1 C, 1.6 Mn, 0.014 P, 0.3 Si, 0.04 Nb, 0.035 V, and 0.03 Al (wt pct).

While Davies and Magee (25) insisted that the strength of dual-phase steels is a linear function of martensite content [*i.e*, does not depend upon the carbon content (strength) of the martensite], Speich *et al*. (9, 24) and Tamura *et al*. (40) felt otherwise. The results of Speich *et al*. (24) are shown in Figure 17, where a clearly non-linear relationship between strength and martensite content and a dependence upon the strength of the martensite are shown. As the experimental approaches of Davies and Magee (25) and Speich *et al*. (24) are nominally similar, the reason for the discrepancy (contrast Figure 15 and Figure 17) is uncertain, but may be related to variations in analytical technique. Also, the data in Figure 15 show considerable scatter, and the non-linear behavior may have been simply overlooked. Microstructure-based strength prediction of dual-phase steels is discussed in more detail in Section 2.4.1.

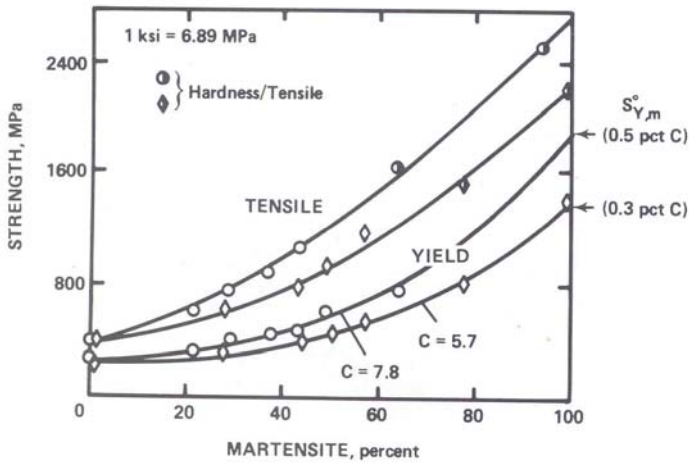

Figure 17: Yield and tensile strength of ferrite-martensite mixtures in 1.5 wt pct Mn steels (24). C is the ratio between the yield strength of martensite to that of ferrite, and $S°_{Y,m}$ is yield strength corresponding to 100 pct martensite.

2.3.2 **Correlation between Microstructure and Ductility**

Balliger and Gladman (10) considered not only the influence of martensite content, but also the influence of the martensite *distribution*. Their results showed that, while the tensile strength of a dual-phase steel is determined primarily by the volume fraction of martensite, the work hardening rate ($d\sigma/d\varepsilon$) at a given strain is affected by the distribution of martensite [*e.g.*, the average martensite "island" diameter, $d(\alpha')$]. Specifically, they showed that the work hardening rate depends on a factor, $\sqrt{f/d}$, where f is the volume fraction of second phase (martensite), and d is the average island diameter. Figure 18 shows this relationship for a series of dual-phase steels at a nearly constant volume fraction of martensite (0.19 to 0.23). Ranging from just over 5.5 μm to just under 8 μm, d has a tremendous influence on the work hardening rate (at $\varepsilon = 0.2$) and corresponding uniform elongation value, with very little influence on ultimate tensile strength. Balliger and Gladman (10) explained that the key to optimizing dual-phase steels for maximum formability at a given strength level (martensite content) is to refine the martensite

distribution. The theoretical basis for understanding the work hardening behavior of dual-phase steels is discussed in Section 2.4.2.

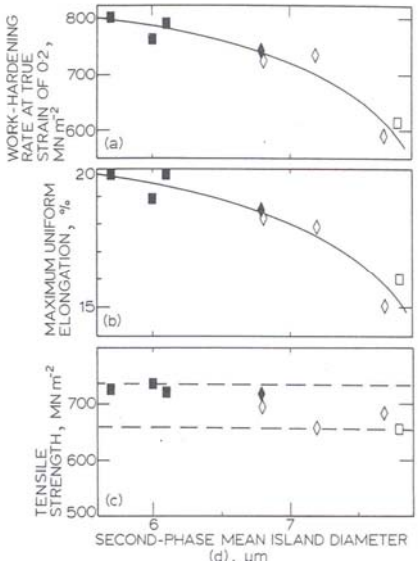

Figure 18: Effect of mean martensite island diameter on tensile properties and work hardening behavior at a nearly-constant volume fraction of martensite [$f_v(\alpha') = 0.19 - 0.23$] for a series of dual-phase steels (10). Note the significant influence of martensite distribution on uniform elongation and work hardening rate and the relative independence of strength.

Speich and Miller (9) developed empirical relationships that relate the uniform and total elongation values of dual-phase steels to the carbon concentration in the martensite and the volume fraction of martensite. In the original nomenclature of Speich and Miller (9), the prediction of uniform elongation is given as

$$e_u / e^{O}_{u,\alpha} = 1 - 2.2 C_m \left(P_m / 100 \right)^{1/2}, \qquad [4]$$

where $e_u / e^{O}_{u,\alpha}$ is the ratio between the uniform elongation value of the composite dual-phase material and that for 100 pct ferrite, C_m is the carbon content in the martensite, and P_m is the martensite content (volume pct). The martensite carbon content is determined simply by

$$C_m = 100\left(C_O / P_m\right), \qquad [5]$$

where it is assumed that the total carbon, C_0 has partitioned to the austenite at the intercritical temperature and that the ferrite carbon content in the finished product is negligible. A similar relationship was developed for the total elongation value, where

$$e_t / e_{t,\alpha}^{O} = 1 - 2.5C_m\left(P_m / 100\right)^{1/2}, \qquad [6]$$

and $e_t / e_{t,\alpha}^{O}$ is the ratio between the total elongation value of the composite dual-phase material and that for 100 pct ferrite. Figure 19 shows the excellent correlation between the regression analysis results (Equations 4 and 6) to the experimental data. Apparently, the distribution of martensite (mean island diameter) is nearly constant for the series of alloys shown in Figure 19, or perhaps the effects of second phase distribution were absorbed in the coefficients of the regression analyses given in Equations 4 and 6.

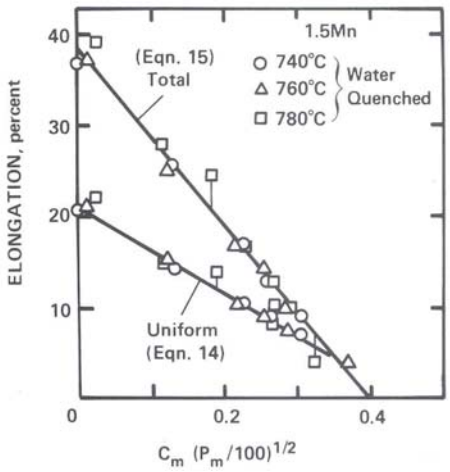

Figure 19: Effect of martensite content and martensite carbon content on uniform and total elongation (9) for a series of dual-phase steels. In this figure, "Eqn. 14" is Equation 4 in the text, and "Eqn. 15" is Equation 6 in the text.

For the same series of alloys represented in Figure 17 and Figure 19, Figure 20 shows uniform elongation and total elongation as a function of tensile strength (9). As for most steels, the ductility decreases as strength increases. However, it appears that lower-carbon martensite (*i.e.*, lower strength martensite) favors improved formability. One interpretation is that, for lower carbon martensite, cracking of the martensite particles and/or decohesion of the ferrite/martensite interface is suppressed (24). Rashid (22) offered the explanation that the enhanced ductility of dual-phase steels (in contrast to ferrite-carbide steels) is a result of the relatively higher plasticity of the martensite phase over pearlite and grain boundary carbides. Tseng and Vitovec (38) gave examples of both deforming and non-deforming martensite particles. For steels of a single composition [0.1 C, 1.6 Mn, 0.3 Si, 0.04 Nb and 0.04 V (wt pct)] intercritically-annealed to produce 26 pct martensite (higher carbon martensite) and 56 pct martensite (lower carbon martensite), non-deformed martensite and deformed martensite, respectively, were found in regions of high deformation (tensile specimens).

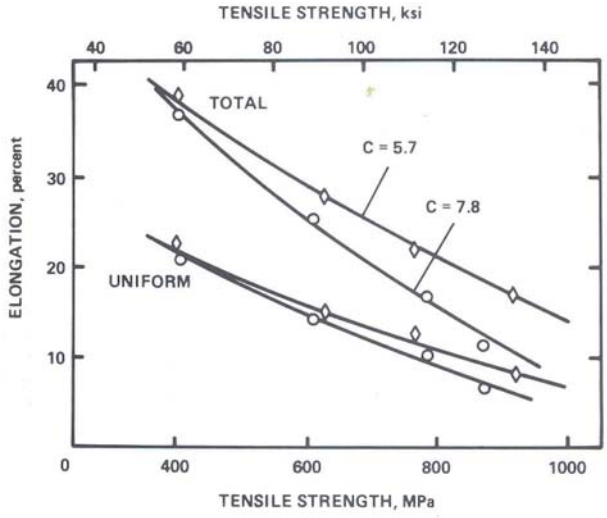

Figure 20: Relation between ultimate tensile strength and elongation for a series of intercritically-annealed, water quenched 1.5 wt pct Mn dual-phase steels (same series as shown in Figure 17 and Figure 19) (9). Note the dependence upon C, the ratio between the martensite yield strength and the ferrite yield strength.

The effects of martensite distribution or size dispersion [*e.g.,* the classification system of Becker *et al.* (30-31) and the experimental observations of Balliger and Gladman (10)] apparently were largely overlooked in most of the early developments of DP steels. It is likely that a more detailed description of two-phase microstructures—beyond martensite volume fraction and martensite carbon content—is needed to understand the mechanical properties of dual-phase steels. In the next section (Section 2.4), various methods to describe and predict the mechanical properties and work hardening behavior of dual-phase steels are reviewed.

2.4 MODELING THE MECHANICAL BEHAVIOR OF DP STEELS

2.4.1 **Predicting the Strength of DP Steels**

Tamura *et al*. (40, 41) estimated the strength of two-phase alloys with a simple rule of mixtures model, where the yield strength, S_Y and tensile strength, S_T of the composite material are given as

$$S_Y = S_{Y,\alpha} P_\alpha /100 + S_{Y,m} P_m /100 \text{ , and} \quad [7a]$$

$$S_T = S_{T,\alpha} P_\alpha /100 + S_{T,m} P_m /100 , \quad [7b]$$

where P is the volume percentage of a particular phase, and the subscripts α and m refer to the partial properties of the ferrite and martensite phases, respectively, for dual-phase steels. They found that Equation 7a was not obeyed except when the yield strengths of the two phases are nearly equal [*e.g.*, a well-tempered ferrite-martensite mixture (24)]. Tamura *et al*. (40) then reasoned that the relationship between S_Y and P_m depends on the ratio of the yield strengths of martensite and ferrite, C where

$$C = S_{Y,m} / S_{Y,\alpha} . \quad [8]$$

They found that, if C<3 then the law of mixture was nearly obeyed. For C>3, S_Y increased linearly with P_m at low P_m-values, then deviated strongly from the prediction at a P_m-value that increased as the value of C increased. This relationship is shown graphically in Figure 21 (40).

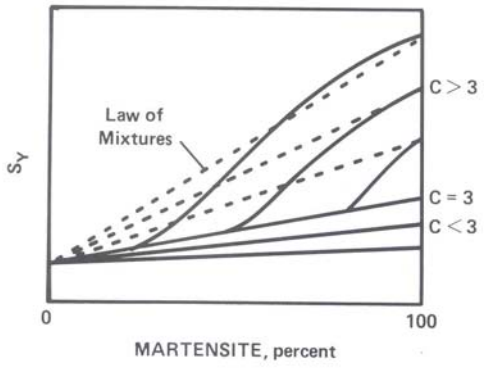

Figure 21: Effect of the parameter C (ratio between martensite and ferrite yield strength) on the variation of yield strength with percent martensite (40). See text for details.

Speich and Miller (9) further developed the relationship established by Tamura *et al.*, and proposed the following predictions for the yield and tensile strengths of dual-phase steels:

$$S_Y = S_{Y,\alpha} + \left(\tfrac{1}{3} S_{Y,m} - S_{Y,\alpha}\right) P_m / 100 , \text{ and} \quad [9a]$$

$$S_T = S_{T,\alpha} + \left(S_{Y,m} - S_{T,\alpha}\right) P_m / 100 . \quad [9b]$$

Equations 9a and 9b are similar to Equations 7a and 7b, but use much lower effective stress values for the martensite phase where $S_{Y,m}$ is replaced by $(1/3)S_{Y,m}$, and $S_{T,m}$ is replaced by $S_{Y,m}$. The yield strength of the martensite phase is used in Equation 9b, as it was estimated that, at the composite tensile strength, the martensite is strained just beyond yielding, and little work hardening of the martensite occurred. The yield strength of the martensite phase ($S_{Y,m}$ in Equations 9a and 9b) was calculated based on the work by Leslie and Sober (42), where

$$S_{Y,m}(MPa) = 620 + 2585C_m \quad [10]$$

and C_m is the carbon content of the martensite (Equation 5). Values of 214 MPa and 400 MPa were determined for $S_{Y,a}$ and $S_{T,\alpha}$, respectively, for a series of 1.5 wt pct Mn dual-phase steels (same series represented in Figure 17 and Figure 19 through Figure 21), and the predictions of Equations 9a and 9b are shown in Figure 22. It appears that the modified rule of mixtures model developed by Speich and Miller (9) closely represents the yield and tensile strengths of ferrite-martensite mixtures when the martensite content is below 50 pct. They explain that, the marked increase in both yield and tensile strength above 50-pct martensite occurs because martensite now becomes the matrix phase and supports a major fraction of the load with little or no deformation of the occluded ferrite.

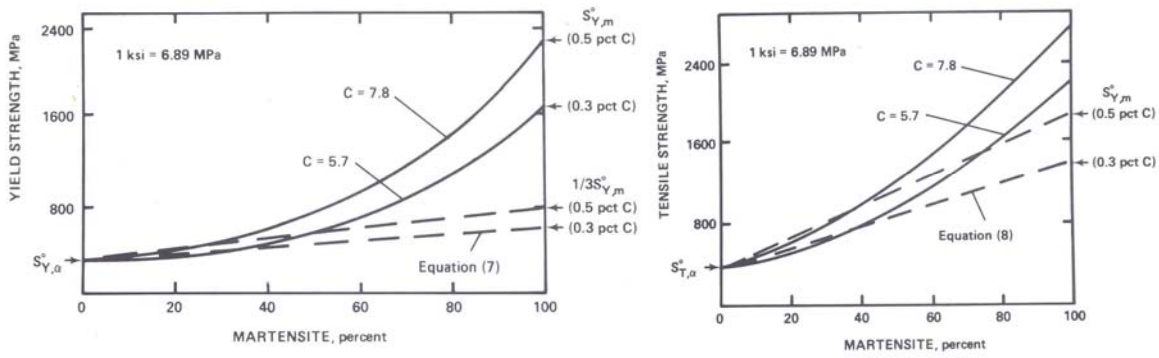

Figure 22: Linear approximations for yield strength (left) and tensile strength (right) of ferrite-martensite mixtures (9). In this figure, "Equation (7)" is Equation 9a in the text, and "Equation (8)" is Equation 9b in the text.

2.4.2 **Modeling the Stress-Strain Curves of DP Steels**

Rios *et al.* (43) extended the analyses of Tamura *et al.* (40-41) and of Speich and Miller (9) to model the stress-strain curves of dual-phase steels with consideration of stress and strain partitioning. They began by assuming that the elastic modulus of ferrite is equivalent to that of martensite, and that the material deforms uniformly up to the point where ferrite begins to

deform plastically. This situation is shown schematically in Figure 23 (43) as the line from the origin, O to point A (slope = 1) in the plot of S^m vs. S^α (engineering stress in the martensite phase and the ferrite phase, respectively).

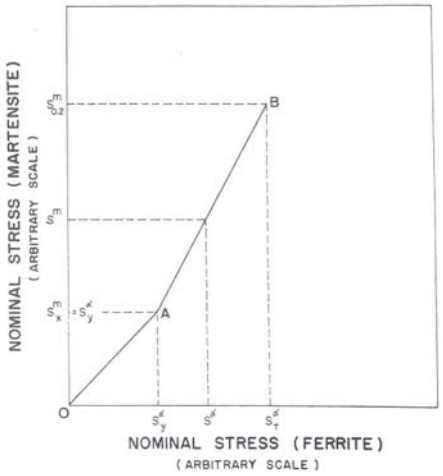

Figure 23: Stress partitioning between martensite and ferrite in dual-phase steels, after Rios *et al.* (43).

Assuming that the martensite phase yields when the ferrite phase has reached its ultimate tensile strength (UTS) [after Speich and Miller's suggestion (9)], a second point B was placed on the S^m vs. S^α plot in Figure 23. At B, the ferrite has reached its UTS, and the martensite is at its 0.2 pct offset flow stress as shown. The greater slope from A to B than from O to A represents the stress partitioning effect, where, at any given plastic strain, the martensite is subjected to higher stresses than the ferrite phase. Rios *et al.* explained that, for lack of deeper understanding, the path from point A to point B is assumed linear. So, between points A and B, the stress level in the martensite phase may be expressed as

$$S^m = S_y^\alpha \left(\frac{S_u^\alpha - S_{0.2}^m}{S_u^\alpha - S_y^\alpha} \right) + S^\alpha \left(\frac{S_{0.2}^m - S_y^\alpha}{S_u^\alpha - S_y^\alpha} \right) \qquad [11]$$

in the notation of Rios *et al.* (43), as shown in Figure 23. The general stress and strain partitioning expressions are

$$S = S^{\alpha}V^{\alpha} + S^{m}V^{m}, \text{ and} \qquad [12a]$$

$$e = e^{\alpha}V^{\alpha} + e^{m}V^{m} \qquad [12b]$$

where S and e are the nominal stress and nominal strain of the composite material; V^{α} and V^{m} are the volume fractions of ferrite and martensite, respectively; e^{α} and e^{m} are the partial (partitioned) strains in the ferrite and martensite, respectively; and S^{α} and S^{m} are as above.

The approach to predicting the stress-strain curves of dual-phase steels was to solve Equations 11, 12a and 12b simultaneously with prior knowledge of the stress-strain curves of the individual martensite and ferrite components. The relation of the individual stress-strain curves of ferrite and martensite to that of the composite dual-phase steel is shown schematically in Figure 24. The tie line between the UTS of the ferrite phase and the 0.2 pct offset flow stress of the martensite phase passes through the UTS of the dual-phase steel, and the composite stress-strain curve lies between those of the individual-phases.

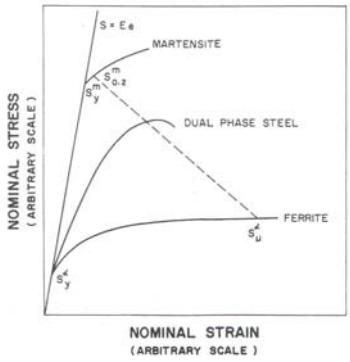

Figure 24: Schematic stress-strain curves for individual-phases martensite and ferrite, in addition to the predicted stress-strain curve of a composite dual-phase steel (43). Note the tie-line between the UTS of the ferrite phase and the 0.2 pct offset flow stress of the martensite phase, that passes through the UTS of the dual-phase steel at an effective composite strain between the partial (partitioned) strains of the individual-phases.

The individual stress-strain curves of ferrite and martensite were taken "from the literature", and the results of the estimations of Rios *et al.* (43) are shown in Figure 25. Also in Figure 25 is a predicted stress-strain curve based on the assumption of Tamura *et al.* (41) that *strain* partitioning (rather than *stress* partitioning) is constant throughout deformation. The strain partitioning constant, $K = e^m/e^\alpha$ was chosen such that good agreement was obtained at the ultimate tensile strength (*i.e.*, K = 0.56). It is clear that, for the particular case reported by Rios *et al.*, the linear stress partitioning model (Equation 11) provides a good description of the stress-strain behavior of the dual-phase steel—far better than that provided by the linear strain partitioning model.

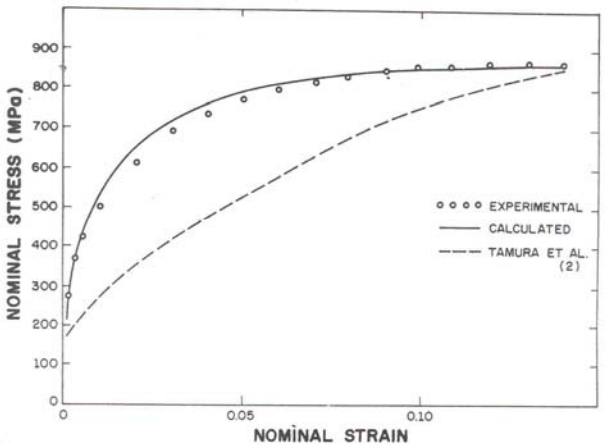

Figure 25: Experimental and calculated engineering stress-strain curves for a dual-phase steel. The continuous curve shows the prediction of Rios *et al.* (43), while the dashed curve shows the prediction based on the work of Tamura *et al.* (41). See text for details.

Finally, by virtue of the linear stress partitioning assumption, the resultant calculated strain partitioning response is necessarily non-linear, as shown in Figure 26 in contrast to the linear strain partitioning model. The measured martensite content in the material examined by Rios *et al.* was about 32 pct. The yield strength (~300 MPa) and the tensile strength (~850 MPa)

are consistent with the strength/ martensite content relationships shown by Davies and Magee in Figure 15 (25).

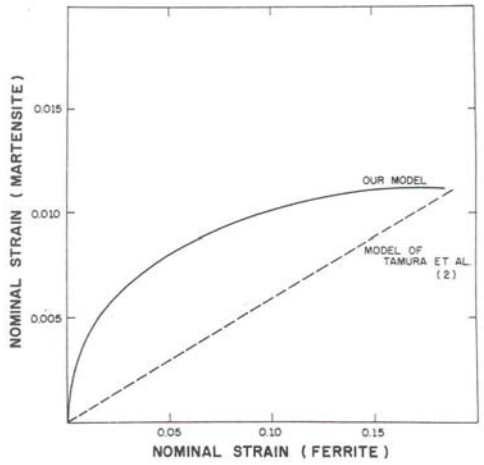

Figure 26: Linear and non-linear strain partitioning estimations for dual-phase steels given by Tamura *et al.* (41) and Rios *et al.* (43), respectively. In this figure, "OUR MODEL" refers to that of Rios *et al.* Note the difference in ordinate and abscissa scales.

Chang and Asaro (44) suggested that the flow stress, σ_f of spheroidized ferrite-carbide steels might be viewed as a combined effect of various strength components, as

$$\sigma_f = \sigma_0 + \sigma_B + \sigma_D \qquad [13]$$

where σ_0 is the initial flow stress (related to yield strength), σ_B is a back stress or residual stress (related to plastic incompatibility between relatively hard and soft microconstituents), and σ_D is the total true work hardening of the system (the subscript D in Equation 13 refers to dislocation based mechanisms). For dual-phase steels, the total work hardening may be expressed as a root-squared summation of the matrix effects, σ_{WHM} and the extra work hardening caused by the presence of the martensite, σ_{WHP}, where

$$\sigma_D = \left(\sigma_{WHM}^2 + \sigma_{WHP}^2\right)^{1/2}. \qquad [14]$$

In the original notation of Chang and Asaro (44), the subscript M refers to the matrix (not martensite), and the subscript P refers to particles or precipitates (*i.e.*, martensite in dual-phase steels). Gerbase *et al.* (18) expanded Equation 13 (with σ_D as in Equation 14) to include the contributions of Brown and Stobbs (45) in regard to the back stress, σ_B and of Ashby (46) in regard to σ_D to obtain

$$\sigma_f = \sigma_0 + \alpha_1 \mu f \varepsilon^*_p + \left\{ \left(\alpha_2 \mu b \varepsilon_p^{1/2} \right)^2 + \left(\alpha_3 \mu b \varepsilon_p^{1/2} \right)^2 \right\}^{1/2} \quad [15]$$

where α_1, α_2 and α_3 are constants, μ is the shear modulus of the matrix, b is the Burgers vector of the matrix dislocations, f is the volume fraction of martensite, ε_p is the total plastic strain, and ε^*_p is the unrelaxed strain associated with the plastic incompatibility between ferrite and martensite. The origin of the back stress, σ_B is discussed in detail in Section 2.5. The general form of the Ashby work hardening model (46) for hard, non-deforming particles in a soft matrix is

$$\sigma_f = \sigma_0 + \alpha \mu \left(\frac{bf\varepsilon_p}{d} \right)^{1/2} \quad [16]$$

where α is a constant, and d is the average particle diameter (or average effective martensite island diameter in dual-phase steels). It is not clear how Gerbase *et al.* (18) applied Ashby's model to arrive at Equation 15, but the constants α_2 and α_3 are somehow related to the volume fractions of ferrite and martensite, respectively. However, the σ_B values were determined experimentally with tension/reverse compression tests at various levels of strain (*i.e.*, Bauschinger Effect tests—see Section 2.5.2). An example of the development of back stress in dual-phase steels is given in Figure 27 (18). Gerbase *et al*. explained that the back stress, σ_B rises very rapidly at small strains and saturates at the onset of an alternative mechanism such as

yielding or fracture of the martensite phase. The rapidly increasing back stress is likely partly responsible for the very high work hardening rate of dual-phase steels in the early stages of plastic deformation. Thus, the initial work hardening rate reflects the volume fraction of martensite, and the limit of the contribution of σ_B is determined by the onset of competitive processes. Although vaguely described, Gerbase *et al.* (18) used measured σ_B values, along with Equation 15, to predict the stress-strain behavior of several dual-phase steels quite successfully, as shown in Figure 28.

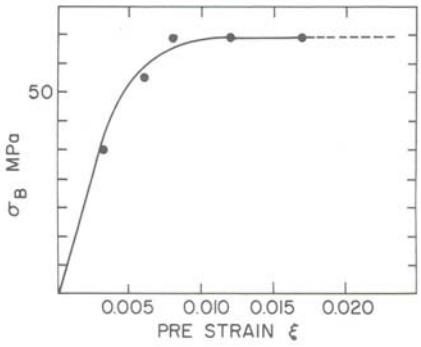

Figure 27: Example of the development of back stress, σ_B in dual-phase steels as a function of tensile strain (18).

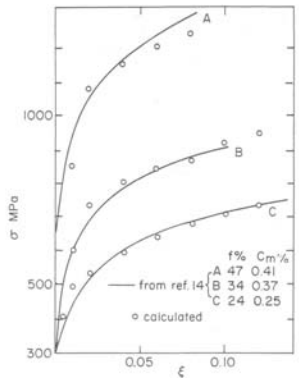

Figure 28: Predicted and experimental true stress-true strain curves for dual-phase steels with various martensite contents—after Gerbase *et al*. (18). In this figure, "ref. 14" refers to Reference 47 of this document. Also, f % is the volume percent martensite of each steel, and C_m % is the wt pct carbon in the martensite of each steel.

Interestingly, Balliger and Gladman (10) did not consider the back stress when evaluating the microstructure effects on the work hardening behavior of dual-phase steels (see Section 2.3.2 and Figure 18). They considered only the Ashby work hardening model (Equation 16)—note the $\sqrt{f/d}$ dependence of the flow stress and the work hardening rate in Ashby's classical model. As the back stress, σ_B saturates at a low strain value, σ_B is not expected to affect the work hardening rate at higher strains, as examined by Balliger and Gladman (10). It is likely that, because of the initially rapidly-increasing back stress reported by Gerbase *et al.* (18), Balliger and Gladman would have been less satisfied with their predictions had they considered the work hardening behavior of dual-phase steels at *low* plastic strains.

2.5 THE BAUSCHINGER EFFECT IN DP STEELS

The aforementioned back stress contribution to the flow stress of dual-phase steels, σ_B may be illustrated by a simple reverse strain experiment, as shown in Figure 29 (48). After an initial uniaxial tension prestrain, a sample is uniaxially compressed such that the uniaxial compression flow curve (σ_R vs. ε) may be contrasted with the original uniaxial tension flow curve (σ_F vs. ε). Note that the compression flow curve has been rotated 180° about its intersection with the strain axis, and that the subscripts F and R refer to forward and reverse deformation, respectively. In Figure 29, the difference between σ_F and σ_R is equal to twice the back stress, σ_B, and, in the absence of a back stress, σ_F and σ_R would both be equal to $\frac{1}{2}(\sigma_F + \sigma_R)$. The lowered flow stress after a load reversal is the essence of the Bauschinger Effect, or "BE" [after J. Bauschinger—1881 (49)]. In the following, the mechanisms responsible for the BE, the most common ways to measure the BE, and various observations of the BE in dual-phase steels will be discussed.

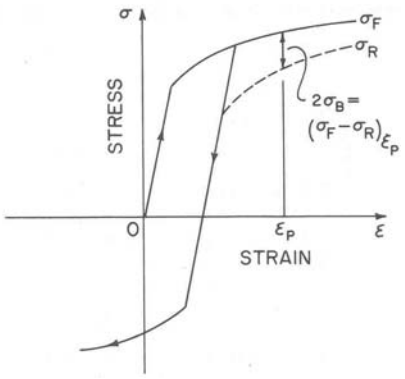

Figure 29: Schematic diagram that relates the back stress, σ_B to the forward flow stress, σ_F and reverse (compression) flow stress, σ_R after a uniaxial tension prestrain. In the absence of a back stress, the forward and reverse flow stresses at a plastic strain of ε_P would equal $\frac{1}{2}(\sigma_F+\sigma_R)$ in the diagram (48).

2.5.1 **Mechanisms of the Bauschinger Effect**

Zhonghua and Haicheng (16) described the Bauschinger Effect as "…a manifestation of anisotropic plasticity induced in an isotropic material by plastic deformation," and divided the responsible Bauschinger Effect mechanisms into two classes, namely short-range effects and long-range effects. Short-range dislocation interactions occur in even the purest of monocrystalline metals, and Orowan (50) explained that, during plastic deformation, dislocations accumulate (*i.e.*, in a pile-up) at barriers in tangles, and eventually form cells. When the load is removed, dislocations do not move appreciably because the structure is mechanically stable (*i.e.*, arranged in a low-energy dislocation structure). Once the loading path is reversed (opposite the original deformation or prestrain), some dislocations move easily at a low shear stress since the barriers behind the dislocations are fewer and farther between—in contrast to the barriers ahead of the dislocations. The net result is plastic flow at a lower stress level when the loading direction is reversed. As this mechanism of the Bauschinger Effect lies in the structure of the

cold-worked state, the Bauschinger Effect is expected to occur in all metals that store cold-work energy.

Deformation also induces long-range internal stresses in single- and multi-phase materials. The primary sources of such long-range internal stresses are reportedly dislocation pile-ups at grain boundaries and at subgrain boundaries; plastic incompatibility among neighboring grains; and plastic incompatibility between second phase particles and matrices (16). In polycrystalline metals, geometrically necessary dislocations (GNDs) are generated near grain boundaries during deformation to maintain physical continuity between neighboring grains of different orientation as they undergo slip-related shape distortions (17). Without GNDs, voids and nonsensical spatial overlaps between grains would occur in the aggregate (hence the name "geometrically *necessary* dislocations"). GNDs produce localized strain gradients within individual grains that result in an additional source of deformation-induced internal stresses. GNDs are typically distinguished from statistically stored dislocations (SSDs). SSDs are those dislocations that encounter and trap one another randomly, as in a single crystal. Furthermore, SSDs have no net effect on lattice curvature, and a Burgers circuit taken around a group of SSDs has no net Burgers vector (17).

It is generally recognized that the Bauschinger Effect is much more pronounced in two-phase alloys than in single-phase alloys. It has been surmised (16) that the long-range internal stresses in each microconstituent, caused by the misfit strains between them, are much higher in contrast to the long-range internal stresses acting over the scale of the grain size in single-phase materials. Stress and strain partitioning (see Section 2.4.2) lead to long-range residual stresses in two-phase microstructures (14, 16, 51). Figure 30 shows various ideal models for stress and strain partitioning (51).

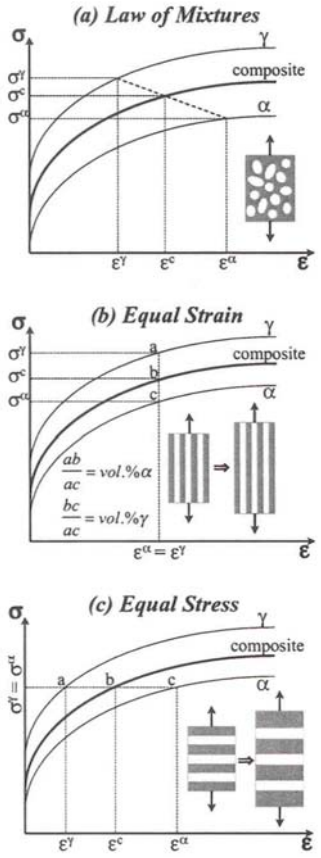

Figure 30: Various ideal models for stress and strain partitioning in two-phase alloys (51). In this figure, γ is the relatively hard phase (martensite), and α is the relatively soft phase (ferrite). The law of mixtures is a more realistic model, as it allows partial load partitioning and partial deformation partitioning.

The Law of Mixtures model (Figure 30a) shows the most realistic representation of stress and strain partitioning in dual-phase steels where partial load transfer and partial strain transfer are shown. The Equal Strain and Equal Stress models (Figure 30b and Figure 30c, respectively), although oversimplified, are useful in understanding the development of deformation-induced residual stresses in dual-phase steels. For the Equal Strain model, the hard and soft phases are strained together in tension, while the stresses are partitioned according to the respective work hardening behavior of the individual-phases. Once the load is removed, full elastic recovery of the harder phase is constrained by the limited elastic recovery of the softer phase (assuming

similar elastic properties). So, the Equal Strain model predicts that, for uniaxial tension prestrain, the deformation-induced residual stress distribution will be tension in the harder phase (martensite) and compression in the softer phase (ferrite). For the same applied tensile prestrain, the Equal Stress model predicts that both phase are under the same local stress conditions, and the strains are partitioned according to the respective work hardening behavior of the individual-phases. With the assumption that the interfaces between martensite and ferrite remain intact, the strain gradients near the interfaces must result in a distribution of residual stresses. In the schematic 2-dimensional layered microstructure shown in Figure 30c, the residual stresses would develop normal to the applied tensile axis because the limited strain in the harder phase restricts the width-wise contraction of the softer phase. Thus, both the Equal Strain and Equal Stress models (and hence the combined Law of Mixtures model) predict the development of deformation-induced residual stresses that contribute to the Bauschinger Effect in dual-phase steels. Examples of calculated and measured deformation-induced residual stresses are given in Sections 2.5.3 and 2.6, respectively.

2.5.2 **The Bauschinger Effect Test**

As shown in Figure 29, the Bauschinger Effect (BE) is normally regarded as a decreased flow stress in reverse deformation (*e.g.*, uniaxial tension followed by uniaxial compression, or vice versa). As the BE is a complex interaction of several possible residual back stress mechanisms, the BE can be manifested in different ways in different materials. Correspondingly, there are several different ways to quantify the BE, as shown in Figure 31 (16), where most of the common Bauschinger Effect quantification parameters are defined.

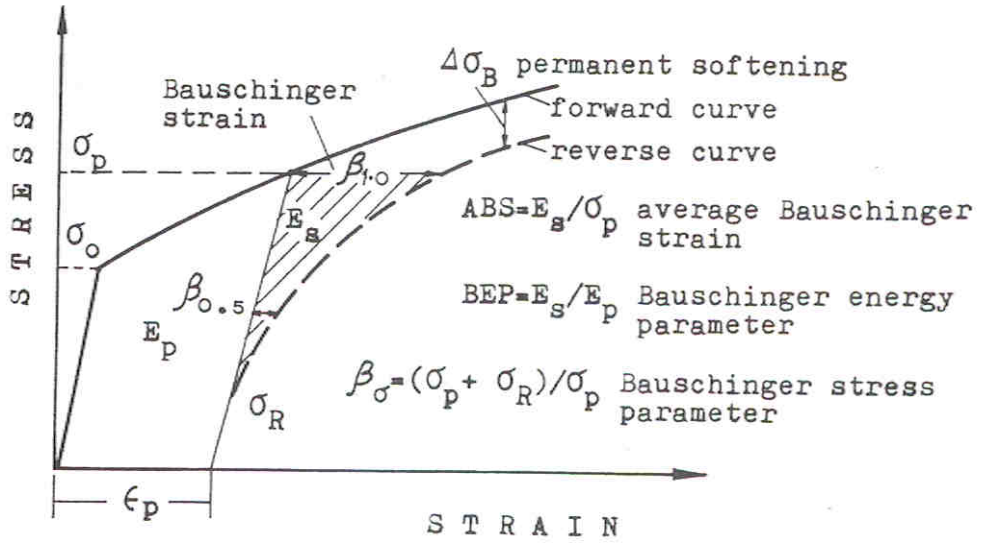

Figure 31: Schematic diagram of the Bauschinger Effect with its various quantification terms (16). See text for details.

The important features of Figure 31 are:

- σ_0: Initial yield strength in uniaxial tension.
- σ_p: Flow stress at the end of prestrain, ε_p in uniaxial tension ("prestress").
- σ_R: Yield strength in reverse deformation (compression)—note that the compressive flow curve has been rotated 180° about its intersection with the abscissa.
- $\beta_{1.0}$: The strain required in reverse loading to achieve the prestress, σ_p. $\beta_{0.5}$ is used when the entire reverse flow curve lies below σ_p.
- ε_p: Prestrain energy (area under the stress-strain curve up to ε_p).
- E_s: Energy gained in reverse deformation by straining to $\beta_{1.0}$ (cross-hatched area).
- $\Delta\sigma_B$: Permanent softening parameter defined as the difference between the forward and reverse flow stress when the forward and reverse flow curves are "parallel" (note:

$\Delta\sigma_B$ is sometimes defined as $2\sigma_B$, or two times the back stress; see for example Figure 29).

- ABS: Average Bauschinger Strain defined as the energy gain (E_s) normalized by the prestress, σ_p.
- BEP: Bauschinger Energy Parameter = E_s/E_p.
- β_σ: Bauschinger Stress Parameter = $(\sigma_p + \sigma_R)/\sigma_p$, where $\beta_\sigma = 0$ means no BE ($\sigma_R = -\sigma_p$).

Tseng and Vitovec (38) noted that, in the absence of permanent softening ($\Delta\sigma_B = 0$) it may be useful to define a term, ε_{RC} that defines the amount of reverse deformation required to achieve (intersect) the initial forward flow curve. Other Bauschinger Effect parameters may also exist, but those shown in Figure 31 are most common.

2.5.3 **Observations of the Bauschinger Effect in Dual-phase Steels**

Tseng and Vitovec (38) showed for a series of dual-phase steels (see Figure 16) that the Bauschinger Effect (BE) increases as prestrain increases (represented by ABS defined above). They also showed that, in general, dual-phase steels do not exhibit permanent softening (*i.e.*, reverse curve always intersects the initial forward flow curve). The ε_{RC}-values ranged from less than 1 pct to about 5 pct strain for uniaxial tension prestrains up to about 10 pct, as shown in Figure 32 (38). In reporting BE data, it is extremely important to convert all stresses and strains to true values (not nominal or engineering values). In many cases it is not specified (as in the work by Tseng and Vitovec). By using engineering values, uniaxial tension stresses would be too low, while uniaxial compression stresses would be too high, possibly masking the permanent softening effect, if present.

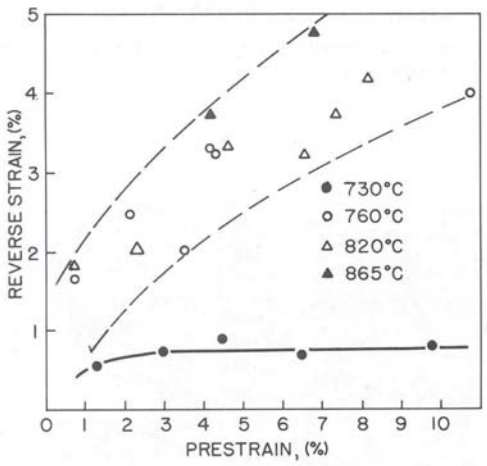

Figure 32: Reverse plastic strain to the point of intersection with the initial forward curve as a function of tensile prestrain for a series of dual-phase steels (38).

Zhonghua and Haicheng (16) examined the Bauschinger Effect in a series of ferrite-martensite steels with conventional reverse deformation (tension/ compression) tests. The forward and reverse curves for their materials are shown in Figure 33. Included in Figure 33 are BE test results for (a) a 100 pct ferrite steel, (b) a 100 pct martensite steel, (c) a 16 pct martensite dual-phase steel, and (d) a 40 pct martensite steel. Their initial observations were:

- Although all four steels exhibited the Bauschinger Effect, the BE is generally much more pronounced in dual-phase steels than in single-phase steels.
- The dual-phase steels exhibit permanent softening.
- The 100-pct ferrite steel exhibits no permanent softening.
- The 100 pct martensite steel exhibits permanent strengthening (negative $\Delta\sigma_B$) at low prestrains, but permanent softening at high prestrains.

Again it was unspecified whether nominal or true stress-strain data were used for the curves shown in Figure 33.

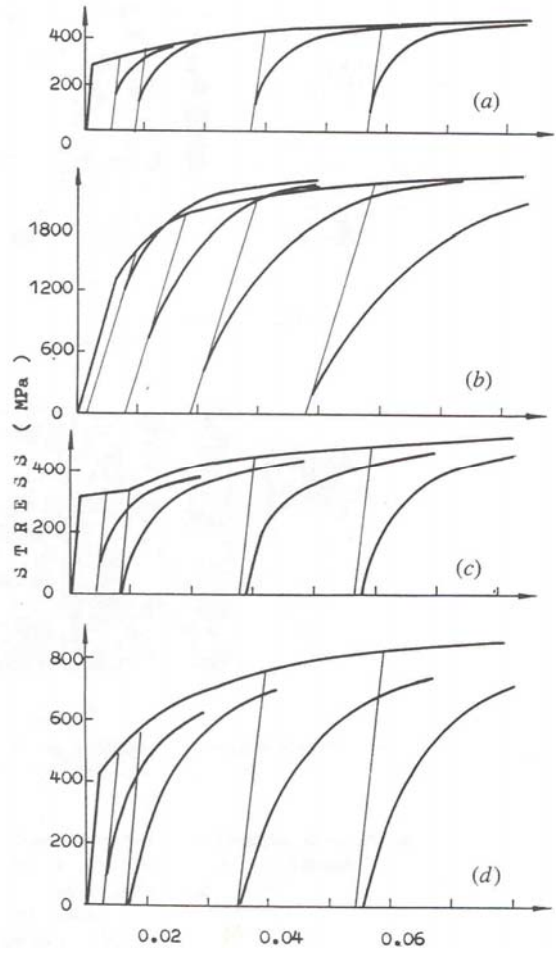

Figure 33: Forward and reverse stress-strain curves for various ferrite-martensite steels: (a) 100 pct ferrite, (b) 100 pct martensite, (c) 16 pct martensite dual-phase steel, and (d) 40 pct martensite dual-phase steel (16). Note the abscissa is plastic strain.

Zhonghua and Haicheng (16) developed a rather insightful and illustrative finite element method (FEM) model that was used to show the development of "phase stresses" in ferrite and martensite during plastic deformation of dual-phase steels. Their model is based on the von Mises yield criterion for effective stress and effective strain (see Section 5.1), and the FEM mesh was created to mimic the geometric features of the dual-phase steel microstructures. Stress and strain partitioning were modeled in a way similar to that of Rios *et al.* (43) shown in Figure 23. The details of the FEM model were not disclosed; however, an excellent correlation between

calculated residual stresses (phase stresses) and BE parameters was shown. They concluded that the deformation-induced residual stresses were the unique factor that controls the BE in dual-phase steels. During tensile prestraining, the internal "phase stresses" promote hardening of the ferrite and softening of the martensite. When the tensile prestrain load is released, residual compressive stresses develop in the ferrite, and residual tensile stresses develop in the martensite. Upon reloading in reverse tension, the deformation-induced residual stresses cause effective softening of the ferrite and effective hardening of the martensite. These residual stress effects result in the well-rounded nature of the reverse flow curve, yielding at a low flow stress, and high work hardening rate. Unfortunately Zhonghua and Haicheng (16) have placed more faith in their FEM predictions than in their experimental results, as one of their conclusions is that "…the residual-phase stresses produced by prestraining do not lead to permanent softening. Instead, the phase stresses are progressively relaxed during reverse loading. After a whole relaxation of these stresses during further reverse loading, the distribution of phase stresses in the two phases is similar to those developed in the forward plastic prestrain stage leading to reverse hardening." This message is not only unclear, but also in direct contradiction to their own experimental results. Regardless of the interpretation, their FEM modeling exercise predicts some interesting features of dual-phase steels, as follows.

- Figure 34 shows the calculated residual effective stress in the ferrite phase, along with the experimental β_σ parameter, for two-dual-phase steels as a function of prestrain. The effective ferrite residual stress is compressive and increases with strain and martensite content. The functional form of the dependence of β_σ (experimentally determined) on prestrain is the same as that of the calculated residual stress.

- Figure 35 shows various calculated and experimental Bauschinger Effect parameters, including ferrite residual stress calculations, as a function of martensite content. Regardless of the measure of BE, it is predicted that the BE will be a maximum at around 50 pct martensite, while the ferrite residual stress is expected to increase monotonically. When normalized by the prestress, the ferrite residual stress follows a similar relationship with martensite as the other BE parameters.
- Figure 36 shows that the ferrite residual stress level is expected to increase monotonically with strain for all martensite contents, and the residual stress level increases as martensite content increases.
- Figure 37 shows the anticipated effects of martensite island size. It is expected that refining the martensite islands will lead to a higher ferrite residual stress level, for a given prestrain and martensite content. These results are consistent with the results of Balliger and Gladman (10).

In a recent analysis of the Bauschinger Effect in high strength steels, Sriram *et al.* (12) reported that the BE depends upon: the amount of plastic prestrain, strength level, and microstructure. They found that "advanced high strength steels" (fancy name for DP and TRIP steels) showed the largest BE of all of the steels studied. In contrasting DP and TRIP steels, Sriram *et al.* explained that DP steels show a larger BE because of the ferrite + martensite microstructure, and that the lower BE in TRIP steels is related to the presence of retained austenite (or more appropriately, related to the strain-induced transformation of retained austenite to martensite). The development of significant residual stresses during deformation was offered as an explanation for the enhanced BE in dual-phase steels. Also, similar to the experimental findings

of Zhonghua and Haicheng (16), a fully martensitic high strength steel showed a reduced BE in contrast to dual-phase steels.

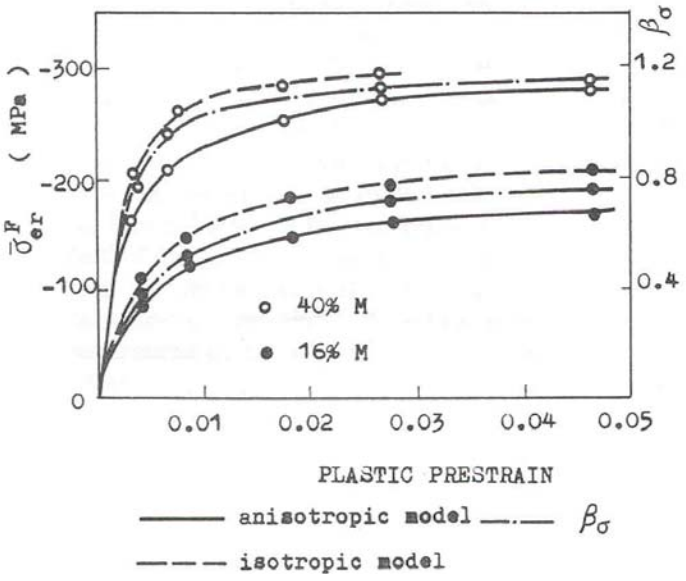

Figure 34: Calculated residual effective stress, $\bar{\sigma}^F_{er}$ in the ferrite phase and experimental Bauschinger Stress Parameter, β_σ as a function of plastic prestrain for two dual-phase steels (16).

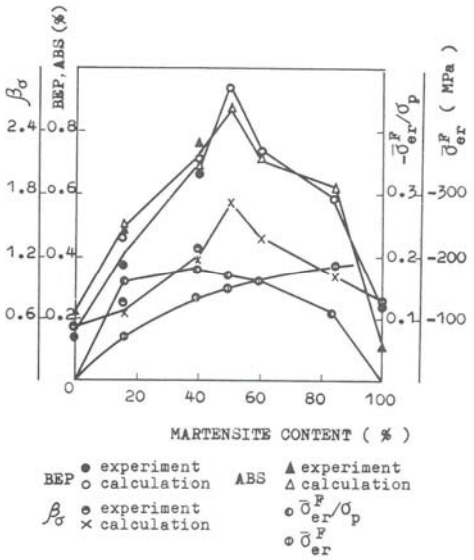

Figure 35: Experimental and calculated Bauschinger Effect parameters for dual-phase steels as a function of martensite content at a prestrain, $\varepsilon_p = 0.008$ (16).

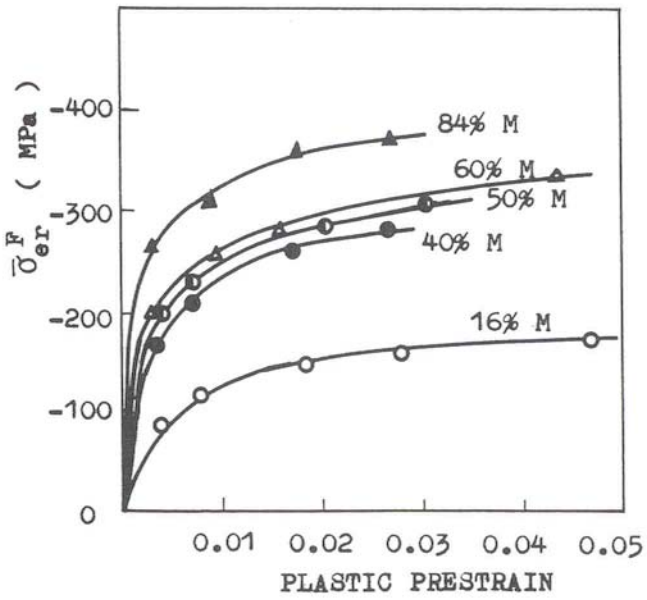

Figure 36: Effects of martensite content and prestrain on the calculated residual effective stress, $\overline{\sigma}^{F}_{er}$ in the ferrite phase of dual-phase steels (16).

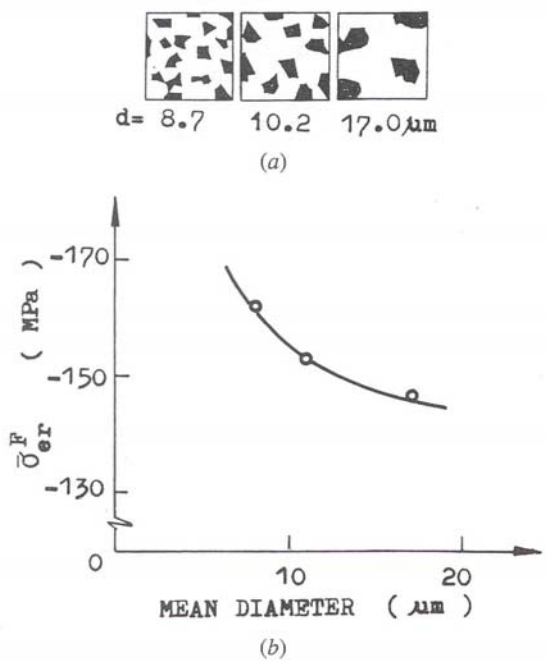

Figure 37: Calculated average residual effective stress, $\overline{\sigma}^{F}_{er}$ in ferrite (b) as a function of martensite island diameter (a) for 25 pct martensite dual-phase steels (16).

2.6 RESIDUAL STRESS MEASUREMENTS IN DP STEELS

While Zhonghua and Haicheng (16) performed a detailed simulative analysis, actual experimental deformation-induced residual stress data for dual-phase steels are scarce, and a literature search on this topic has proved disappointing. In fact, the only two pertinent references found to date discuss x-ray residual stress calculations on deformed TRIP-steels (see Section 2.2.3 for more on TRIP steels). Sugimoto *et al.* (52) showed that if the retained austenite is stable against the martensite transformation during deformation (at higher deformation temperatures), high tensile residual stresses develop in the austenite particles, while compressive residual stresses develop in the ferrite. Thus, the relatively harder austenite particles act like martensite in a dual-phase steel. These results of Sugimoto *et al.* are summarized in Figure 38 (unfortunately, the paper is in Japanese, and of poor reproduction quality). The σ_X values shown in Figure 38 are effective X-ray residual stresses (hence the "X") calculated from diffraction data.

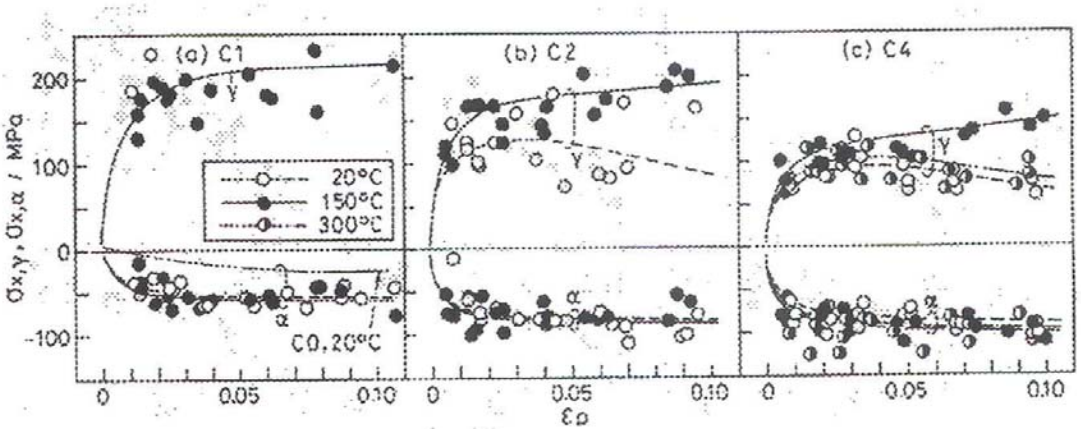

Figure 38: Residual stresses determined by X-ray analysis, σ_X for austenite (γ) and ferrite (α) in three TRIP-assisted dual-phase steels prestrained in tension (52). See text for discussion.

Streicher (14) showed perhaps the most interesting and important (for this research program) X-ray residual stress data, where strain paths other than uniaxial tension were considered. Figure 39 summarizes Streicher's data, where the evolution of deformation-induced ferrite residual stresses is shown in plane strain and balanced biaxial deformation modes. The experimental technique is a bit unclear, however, the data suggest that the residual stresses develop differently along different strain paths and that the residual stress distribution has directional qualities—as shown by the plane strain prestrained specimens evaluated in the major strain axis direction ($\Phi = 90°$) and in the minor strain axis direction ($\Phi = 0°$). Streicher reported significant experimental difficulties in obtaining "reasonable" residual stress measurements for the uniaxial tension prestrain condition; however, the reason is not known.

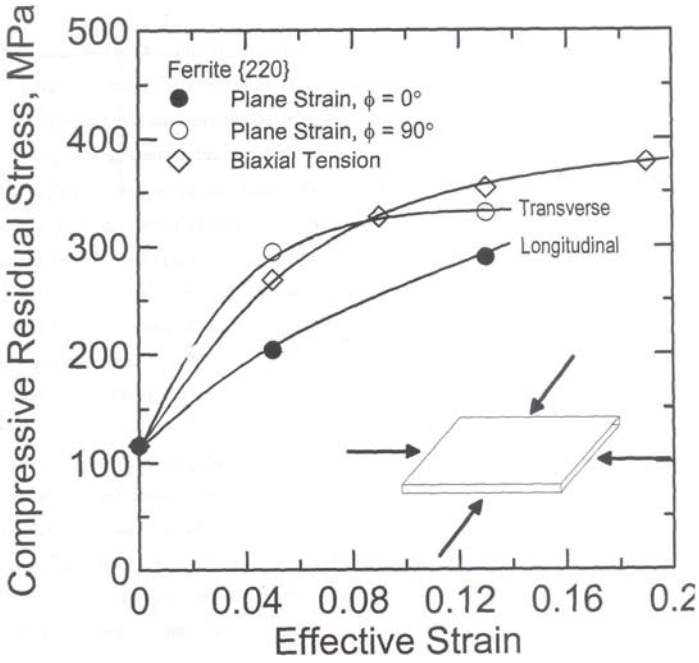

Figure 39: Residual stresses determined by X-ray analysis for ferrite in a TRIP steel (mixture of ferrite, bainite, retained austenite, and martensite) for plane strain and balanced biaxial stretching prestrain (14).

2.7 STRAIN PATH EFFECTS IN SHEET METAL FORMING

2.7.1 **The Concept of Strain Path**

During metal forming, the strain path may be defined as the locus of successive strain increments followed by an element of material as it undergoes plastic deformation. For sheet metal forming, the strain path is often represented in two-dimensional "surface strain" space. The surface strains are the larger (major strain, ε_{maj}) and smaller (minor strain, ε_{min}) principal strains in the plane of the sheet metal. For any given combination of major and minor strain, the thickness strain is known by virtue of the constant volume assumption [*i.e.*, thickness strain = -($\varepsilon_{maj} + \varepsilon_{min}$)]. The strain path during forming is a complex function of material properties (*e.g.*, normal and planar anisotropy) and externally applied loads, or more generally: Strain Path = f_1(material response) · f_2(imposed stresses). Imposed stress variables include loading conditions, specimen and die geometry and interfacial friction (53). Crystallographic-texture-based material deformation models have advanced to the point where adequate prediction of plastic anisotropy and strain path response to applied stresses has been achieved. For example, Chan and Lee (53) have developed such a model that predicts nearly linear strain paths in uniaxial tension and "curvilinear" (non-linear) strain paths under applied biaxial tension stress states. This behavior implies that the annealing or recrystallization texture (before forming) is more stable under uniaxial tension and that biaxial tension leads to altered deformation textures that are different from the annealing texture. Chung and Lee (54) showed such texture changes in a low carbon steel. The results of their analysis are summarized in Figure 40, where deformation textures resulting from uniaxial tension, plane strain and balanced biaxial stretching deformation are shown in contrast to the annealing texture. In a similar manner, Lopes *et al*. (56) showed that

preferred orientation (annealing texture) is the chief contributor to anisotropic work hardening behavior in aluminum alloys.

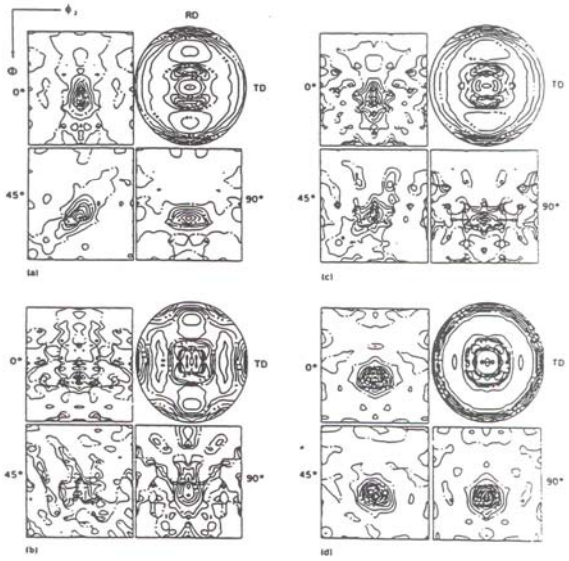

Figure 40: Orientation distribution function (ODF) "slices" and (110) pole figures showing the recrystallization texture (a) and deformation textures (b through d) of a low carbon steel prestrained in various deformation modes (54). For uniaxial tension (b) and plane strain (c) prestrain, the (111) fiber texture (intensity at $\Phi = 55°$, $\phi_2 = 45°$) of the as-produced material is disturbed, while, for balanced biaxial stretching (d), it is strengthened. The angles 0°, 45° and 90° indicate the ϕ_1 angle for each ODF slice [ϕ_1, Φ and ϕ_2 are Euler angles (55)].

Strain paths in sheet metal forming are often simplified as linear relations between principal surface strains. The principal surface strain ratio, $\beta = \varepsilon_{min}/\varepsilon_{maj}$, is a convenient way to approximate a strain path during deformation (assumed linear) (54). In practice [in the context of forming limit diagrams (FLDs), for example—see Section 2.7.3], ε_{maj} is commonly plotted against ε_{min} for practical and conceptual reasons, and as such, the "slope" of the strain path is $1/\beta$. The problem arises, however, that the "slope" of the plane-strain strain path ($\varepsilon_{maj}/\varepsilon_{min}$) is infinity ($\infty$), and this singularity makes strain path representation difficult and awkward. For this

reason, when dealing with experimental data obtained for different deformation modes, β is usually the preferred index of strain path, in the academic environment.

Figure 41 illustrates the major/minor strain relationships for three ideal linear strain paths that are commonly considered in sheet metal forming analyses—uniaxial tension (UT), plane strain (PS) and balanced biaxial stretching (BB). This group of strain paths represents the range of plane stress ($\sigma_3 = 0$) forming conditions from $\sigma_2 = 0$ to $\sigma_2 = \sigma_1$. Subscripts 1, 2 and 3 refer to the principal directions, where σ_1 is applied in the direction of ε_1 (ε_{maj}), σ_2 in the direction of ε_2 (ε_{min}), and σ_3 (zero for plane stress conditions) in the direction of ε_3 (sheet normal or thickness direction). The plane strain deformation path is a special case of unbalanced biaxial tension ($\sigma_1 > \sigma_2$), where ε_{min} (ε_2) is zero. Note that the strain path associated with uniaxial tension (UT) depends on normal anisotropy ($R = \varepsilon_2/\varepsilon_3$) as shown in Figure 41. The required principal stress ratios ($\alpha = \sigma_2/\sigma_1$) for plane strain and balanced biaxial stretching deformation also depend on material anisotropy. In terms of the principal strain ratio, the strain path associated with plastic deformation under an applied uniaxial tension stress state is $\beta = -0.5$, for an isotropic material. Plane strain deformation is described by $\beta = 0$, and balanced biaxial stretching is described by $\beta = 1$. The characteristics of these primary plane-stress strain paths are summarized in Table II.

Table II: Ideal Linear Strain Paths for Plane Stress Deformation ($\sigma_3 = 0$)

Strain Path	ε_{maj} (ε_1)	ε_{min} (ε_2)	Thickness Strain (ε_3)	$\beta = \varepsilon_{min}/\varepsilon_{maj} = \varepsilon_2/\varepsilon_1$
Uniaxial Tension*	ε_1	$-\varepsilon_1 R/(R+1)$	$-\varepsilon_1/(R+1)$	$-R/(R+1)$
Plane Strain	ε_1	0	$-\varepsilon_1$	0
Balanced Biaxial	ε_1	ε_1	$-2\varepsilon_1$	1

*For isotropic material ($R = 1$), $\varepsilon_{min} = \varepsilon_2 = \varepsilon_3 = -0.5\varepsilon_1$ ($\beta = -0.5$).

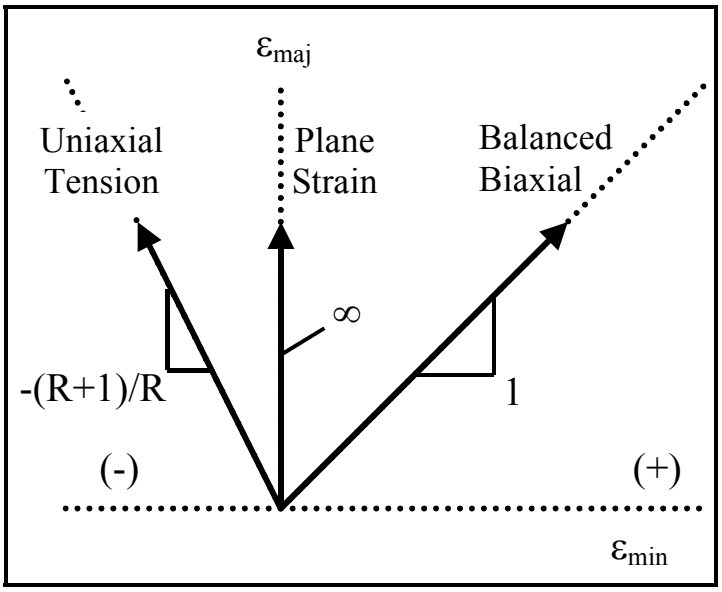

Figure 41: Various ideal linear strain paths for plane stress stretch-forming.

2.7.2 **Complex Strain Paths**

Deformation modes that involve at least one strain path change may be generalized as complex strain paths. There are two basic types of complex strain paths: 1) continuous, and 2) sequential (53). Continuous complex strain paths occur in almost every sheet metal forming operation, and are characterized by gradual or "continuous" strain path changes with no interruption in the forming process. A clear example is the application of draw beads in stretch forming binders. While the material is pulled through the draw bead configuration, it is bent and unbent, then bent again in the opposite direction. Sequential complex strain paths in real forming operations are less common, yet certainly not rare.

A sequential complex strain path is one that consists of abruptly changing imposed stress conditions with a break in the deformation between "sequences". The various processing steps in tube hydroforming are a good example of a real world sequential complex forming operation (tube making, pre-bending, hydroforming, etc.). Also, continuous complex strain paths are

experimentally difficult to analyze, and thus sequential complex strain paths are usually evaluated in experimental analyses of sheet metal forming. The effects of sequential complex strain paths (hereafter: complex strain paths) on material properties have been extensively studied for low-carbon steels and other conventional materials.

2.7.3 **Complex Strain Path Effects on Forming Limits**

An example of the effects of complex strain paths on forming limits is shown in Figure 42 from the classic FLD representation of Kikuma and Nakazima (59). This figure shows the drastic influence of prestrain path on the subsequent stretch-forming limits of low-carbon steel. It is generally regarded that biaxial tension prestrain lowers the subsequent formability after an abrupt strain path change and that uniaxial tension prestrain raises the subsequent formability after a strain path change. Note that in Figure 42, the curve marked "Forming limits of simple deformation path" shows the characteristic "V" shape of the forming limit curve (FLC) of steel, with the plane-strain forming limit (FLC_0) at the minimum. By "simple deformation paths", Kikuma and Nakazima are referring to proportional or linear strain paths as discussed in Section 2.7.1. The "Maximum forming limits curve" shows the influence of uniaxial tension prestrain on the subsequent forming limit along a balanced biaxial stretching strain path. The "Minimum forming limits curve" shows the influence of balanced biaxial stretching prestrain on the subsequent forming limit in uniaxial tension. Ronde-Oustau and Baudelet (60) generalized this behavior by recognizing that, for a given prestrain condition, the subsequent forming limit is diminished more as the secondary strain path deviates further from the primary strain path on the tension side of the FLD (negative minor strain—see Figure 41). As a corollary, they explained that the effects of prestrain are less important when the secondary strain path is far from the primary strain path on the biaxial stretching side of the FLD (positive minor strain).

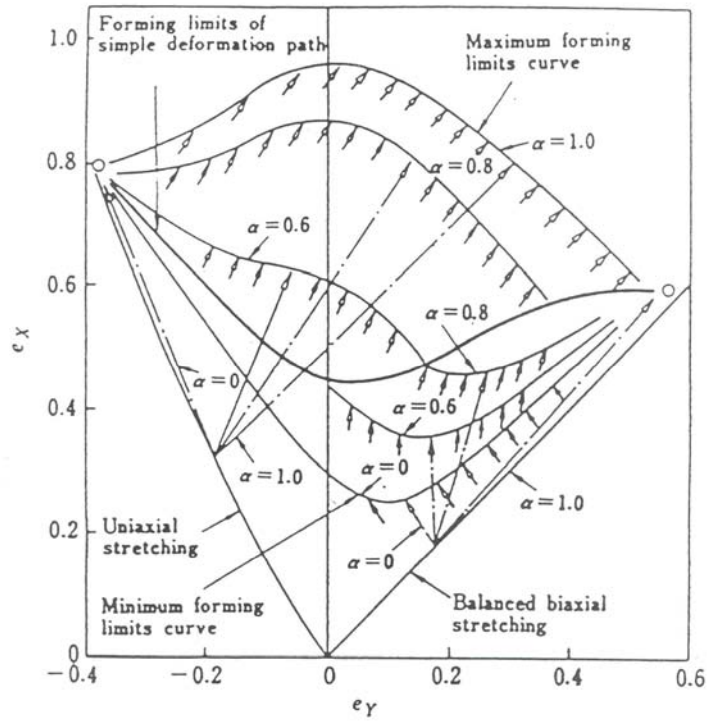

Figure 42: Schematic forming limit diagram for low-carbon steel that shows the effects of primary strain path on forming limits in two-stage sequential complex strain paths. The α parameter is the ratio of principal applied stresses within the plane of the sheet, σ_2/σ_1, where $\alpha=0$ corresponds to uniaxial tension, and $\alpha=1$ corresponds to balanced biaxial stretching (59). In this figure, e_Y is the minor strain, and e_X is the major strain.

Ronde-Oustau and Baudelet (60) also revealed distinctly different dislocation substructure and cell development along different strain paths. The transmission electron microscope (TEM) images in Figure 43 give examples of cell networks that develop during uniaxial tension and during balanced biaxial stretching. Regular, elongated bricklike cells with thin walls tend to form during uniaxial tension deformation, while equiaxed cells with thick, densely tangled walls are characteristic of balanced biaxial deformation. While the terminal cell size for both deformation modes is similar (dimensions on the order of 1 to 2 microns), the mean free path of mobile dislocation motion is intrinsically different. It was explained that the dislocation configuration generated by biaxial stretching leads to shorter mean free dislocation

paths (the effective cell diameter) with up to four slip systems activated. The development of these highly tangled, multiple-slip-system structures hinders subsequent deformation in tension, which requires longer mean free paths to be sustainable—with only two primary active slip systems. The cell structures associated with biaxial stretching are also mechanically stable. Ronde-Oustau and Baudelet commented that the cell structures of biaxially stretched samples remained visible near the very edges of TEM foil specimens, while the substructures of uniaxial tension prestrained samples tend to disappear or "run out" near the edges. Additionally, after balanced biaxial stretching (large enough to establish a cell network), the equiaxed nature of the cells does not change with subsequent deformation in uniaxial tension.

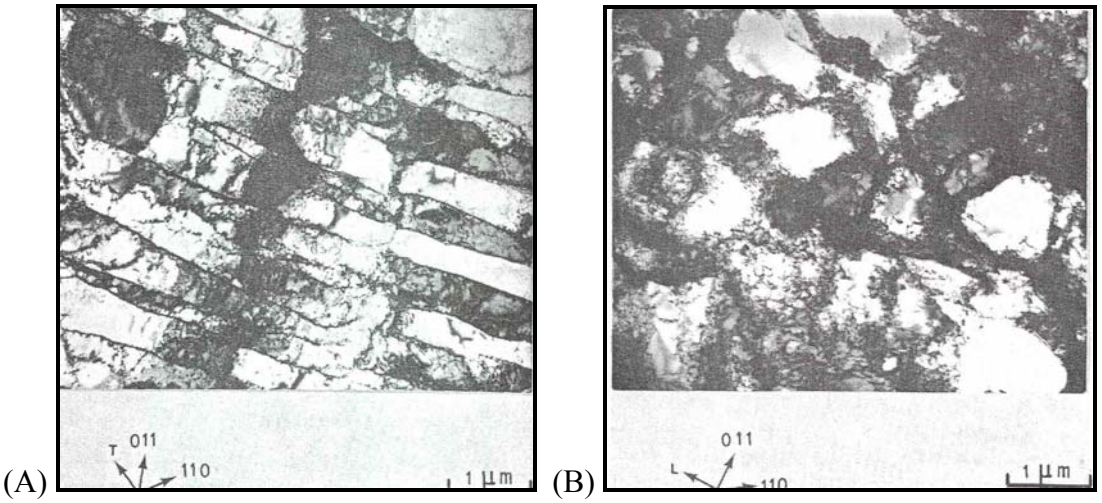

Figure 43: Distinctly different dislocation substructures (cell networks) formed by (A) uniaxial tension deformation and (B) balanced biaxial stretching (60).

Examples of the influence of biaxial stretching prestrain on subsequent tensile flow behavior are given in Figure 44 and Figure 45 (61). Figure 44 shows the rapid work hardening (strength evolution) and loss of tensile ductility in low-carbon steels caused by balanced biaxial stretching prestrain. In this figure, the tensile flow curves (true stress/strain curves) of the prestrained samples have been shifted to account for the forming strain (see Section 5.2) and are

plotted to the end of uniform deformation. For a given amount of effective strain, balanced biaxial stretching results in a much higher subsequent tensile flow stress than does uniaxial tension deformation. Figure 45 shows the effect of balanced biaxial stretching on the residual uniform strain in tension for the same low carbon steel shown in Figure 44. The top curve in this figure represents the predicted values based on consideration of effective strain (again, see Section 5.2). The middle curve shows the adjusted prediction after the flow curves were shifted to coincide tangentially with the reference flow curve (the true stress/strain curve in the as-produced condition). The lowest curve (experimental data) reveals the severe reduction in residual tensile ductility of low-carbon steels caused by balanced biaxial tension prestrain (61).

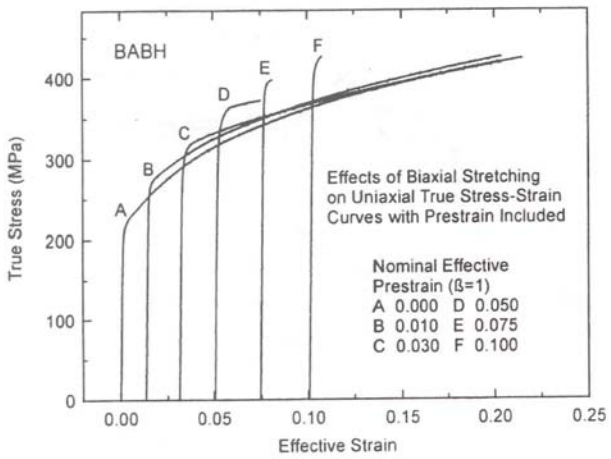

Figure 44: Effects of balanced biaxial stretching on subsequent tensile flow behavior of a low-carbon steel (batch-annealed bake-hardenable, BABH). The flow curves of the prestrained samples are shifted along the strain axis to account for the forming strain (effective strain) (60).

2.7.4 **Differential Hardening Behavior**

The relationships shown in Figure 44 and Figure 45 are expected to be relatively independent of the direction of applied tension after forming in the balanced biaxial stretching mode. That is, as the forming strain is radially symmetric within the plane of the sheet metal, it

follows that the subsequent response in uniaxial tension be symmetric within the plane of the sheet. This extrapolation is certainly made in the context of assumed planar isotropy. Crystallographic texture variations and other directional microstructural features would alter the symmetry of the subsequent forming response, even when the pre-strain mode is nominally symmetric.

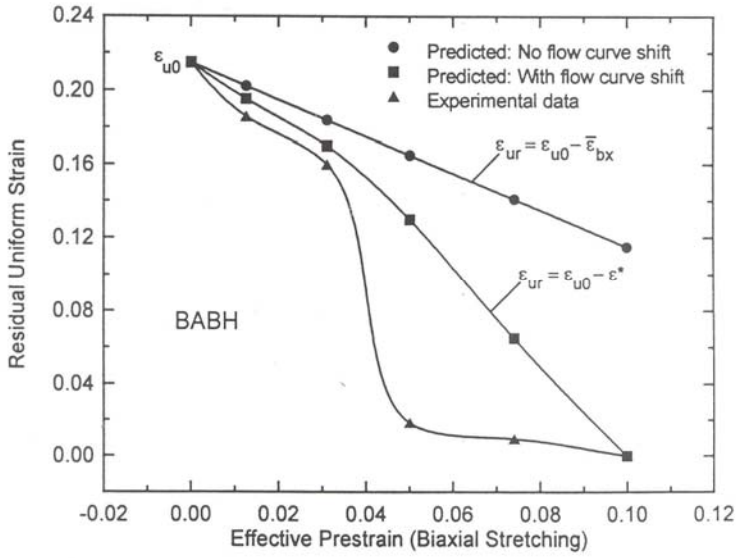

Figure 45: Effects of balanced biaxial stretching on the residual uniform strain in tension for a low carbon steel (same as in Figure 44). The top curve represents the predicted values based on consideration of effective strain. The middle curve shows the prediction after the flow curves are shifted to coincide with the reference flow curve (*i.e.*, shifted so that the flow curve is tangent to that of the as-produced material). The lowest curve shows the actual experimental data that reveal the severe reduction in residual ductility of low-carbon steels caused by biaxial tension prestrain (60).

Just as balanced biaxial stretching ($\varepsilon_{maj} = \varepsilon_{min}$) leads to a symmetric subsequent deformation response, unbalanced stretching ($\varepsilon_{maj} > \varepsilon_{min}$, including uniaxial tension) leads to an asymmetric subsequent deformation response. An example of this differential hardening behavior from the recent work of Yan *et al.* (62) is shown in Figure 46. In this figure there are five stress/strain curves shown on a single plot. The "As-Received" curve represents the

behavior of an interstitial free (IF) steel in the as-produced condition (no prestrain). The other curves represent tensile stress strain behavior after plane strain deformation with the major strain axis aligned in the sheet rolling direction or longitudinal (L) direction. Two prestrain conditions are shown, where "8x0" is 8% major strain, and "12x0" is 12% major strain. The designations (L) and (T) refer to the directions of subsequent tensile deformation. Clearly, when the material is tested in the T direction (90° to the major prestrain direction), the yield strength is greater, and the residual ductility is diminished, in contrast to the case of tension applied in the L direction. This behavior could not be attributed solely to intrinsic material anisotropy.

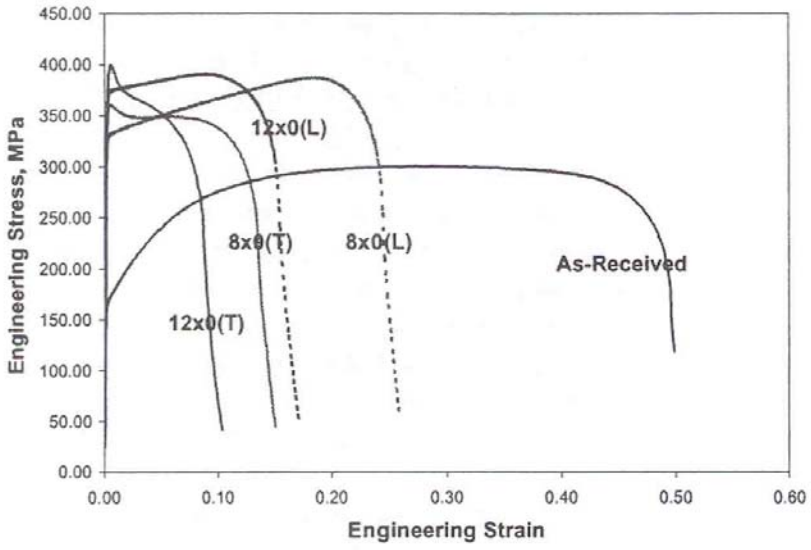

Figure 46: Example of differential hardening in low carbon steel (62) after plane strain prestrain (major strain in the longitudinal, L direction). Tensile tests are in the L direction and the T direction (90° to the L direction). Prestrain conditions are 8% (8x0) and 12% (12x0) major strain. Note the higher flow stress and the diminished residual ductility in the T direction.

Toyoda *et al*. (63) showed similar results for rolling prestrain (also plane strain deformation) and explained the behavior qualitatively with a macroscopic simplification of dislocation interaction mechanisms. Figure 47 (63) illustrates schematically the interpretation of Toyoda *et al*. Shown in Figure 47A are tensile stress/strain curves in the rolling direction (RD)

and transverse direction (TD) after cold rolling in the RD (unspecified amount of reduction). Note the very different behavior in the orthogonal directions. The slab diagrams above the stress/strain diagram show the different tensile direction orientations with respect to the prestrain path. The TD tensile test (labeled "C" for "cross") is marked by the phrase "Hard to slip", while the RD tensile test (labeled "L" for "longitudinal") is marked by the phrase "Easy to slip". The "maximum shear stress planes" are also shown in each slab diagram and represent the active slip planes during cold rolling. If tension is applied in the RD, further slip is possible on the previously activated slip planes. For tension applied in the TD, new slip planes must be activated, as those activated during cold rolling are not properly aligned for continued slip under perpendicularly applied tension. The associated phenomenon shown in the stress/strain curves is called latent work hardening or cross-hardening. Also labeled in Figure 47A are σ_1 values (engineering stress in tension at 1% tensile strain) in both the RD and TD orientations. Toyoda *et al*. (63) used

$$\Delta\sigma_1 = \sigma_{1,TD} - \sigma_{1,RD} \qquad [17]$$

as the index of differential hardening caused by latent work hardening, where $\Delta\sigma_1 > 0$ implies "cross-hardening" and $\Delta\sigma_1 < 0$ implies "cross-softening".

The implications of such cross-hardening are further illustrated schematically in Figure 47B, where the observed stress/strain behavior is a combination of "normal" work hardening with superimposed latent work hardening. In essence, the latent work hardening presents a barrier to uniform deformation in the early stages of plastic deformation that must be "pulled through" to establish "normal" stress/strain behavior. The type of behavior shown in Figure 47B is truly unusual in the context of typically observed stress/strain curves. Specifically, the stress at maximum load (ultimate tensile strength) occurs at a very low strain value and is followed by

a region of upward curvature and another local maximum on the engineering stress/strain diagram at a larger strain value. With these nuances, the definition and meaning of uniform and post-uniform elongation should be carefully reconsidered (this is discussed further in Section 6.1.7).

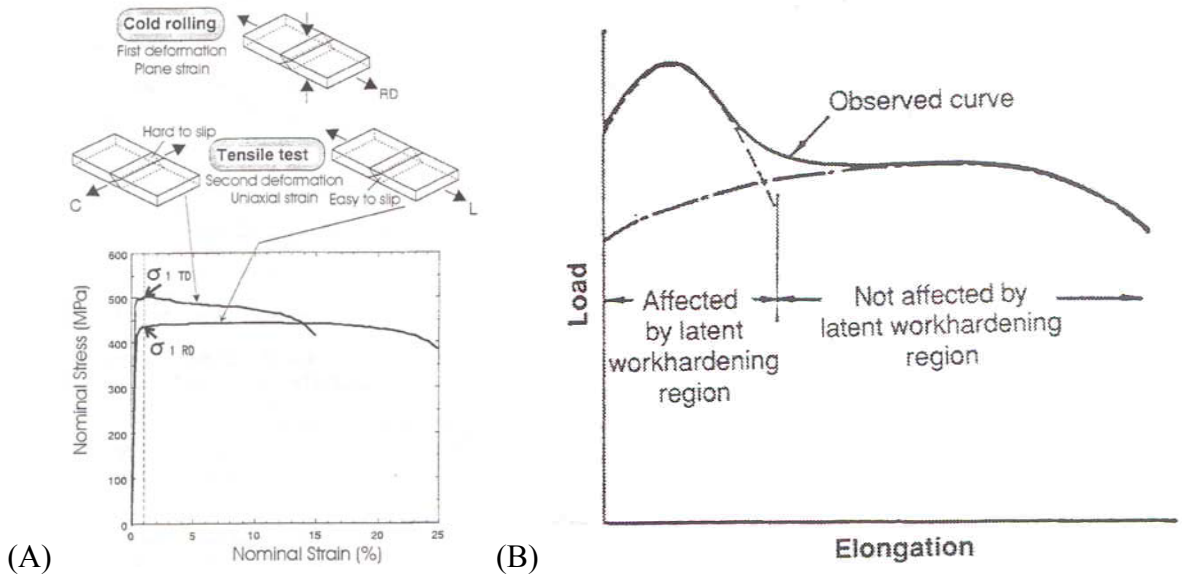

Figure 47: Illustration of the cross-hardening effect caused by latent work hardening (63).

Hasebe (64) showed similar results for IF steel, where uniaxial tension prestrain was followed by secondary tension in the original prestrain direction and in various other directions within the plane of the sheet. It was shown that the cross-hardening effect is itself a directional property. It was shown that the maximum latent hardening effect for uniaxial tension prestrain is observed when the subsequent tensile direction is about 45° to the tensile axis of the primary deformation (although a measurable effect was observed in the 90° orientation). It was explained that, for tensile prestrain followed by transverse tension, there is a "Bauschinger-like" effect, caused by the strain reversal in the orthogonal direction that partially alleviates the cross-hardening in this orientation.

Sugimoto *et al*. (65) illustrated perhaps the most important and interesting results, with respect to this current research program. The experimental setup was similar to that of Toyoda *et al*. (63) and that of Hasebe *et al*. (64) above, but the test material was a dual-phase (DP) steel with approximately 10 vol. pct martensite. Sheet samples of the DP steel were prestrained various amounts in both uniaxial tension and rolling (plane strain) deformation modes. Then, sub size tensile specimens were extracted from the prestrained panels at various angles with respect to the original major prestrain axis. Figure 48 illustrates the tensile stress/strain behavior in various orientations with respect to the rolling direction (major prestrain direction). In Figure 48, ε_p is the amount of prestrain (effective strain—see Section 5.2), and α is the angle between the major prestrain axis (ε_{maj}) and the subsequent applied tension axis. In contrast to the results of Toyoda *et al.* (63) (Figure 47) and Hasebe (64) for "single-phase" low carbon steels, the DP steel exhibits a unique response with respect to differential hardening, where the transverse (90°) direction flow stress is significantly *lower* than the longitudinal (0°) flow stress, especially in terms of the initial yielding behavior. Thus, rather than "cross-hardening", DP steels show a "cross-softening" response. Sugimoto *et al.* (65) noted that the cross-softening effect increases as the amount of prestrain increases, and that the effect is more pronounced for uniaxial tension prestrain than for plane strain (rolling) prestrain. They also noted that the difference in flow stress between the 0° and 90° direction diminishes as tensile deformation continues beyond yielding. That is, the 0° and 90° tensile flow curves tend to converge. The specific differential hardening behavior of DP steels was attributed to deformation-induced residual stresses imparted to the ferrite and the martensite during prestraining.

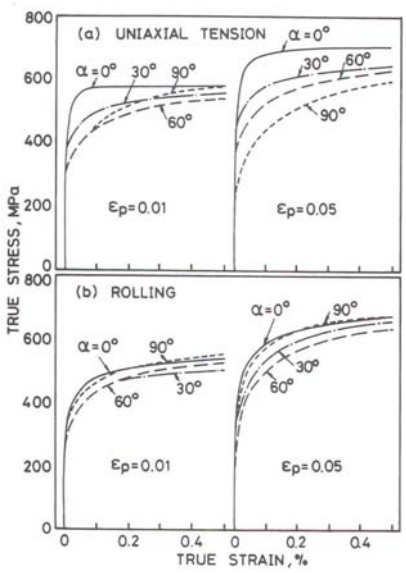

Figure 48: Resultant tensile stress/strain curves for a dual-phase steel after (a) uniaxial tension prestrain and (b) plane strain rolling prestrain (65)]. In this figure, ε_p is the amount of prestrain (effective strain), and α is the angle between the direction of the secondary applied tension and the major strain axis of the primary deformation (prestrain).

More recently, Wasilkowska *et al*. (66), showed similar results for a TRIP steel (see Section 2.2.3) that was prestrained in uniaxial tension [$\varepsilon_{maj} = 0.1 = \varepsilon_{TD}$ (transverse direction)]. Their results are summarized in Figure 49. In this figure, $R_{p0.2}$ is the tensile yield strength (0.2% offset flow stress), σ_n is the ultimate tensile strength, ε_n is the necking strain (true uniform strain), n is the work hardening exponent, and the angles (degrees) represent the difference between the applied tension axes in the prestrain step and the secondary tension step. In this unorthodox yet effective representation, the dashed curve shows the directional properties of the as-produced material (before prestraining); the continuous curve shows the corresponding properties of the prestrained sample; and the shaded regions show changes in each parameter caused by the uniaxial tension prestrain. While there exists a mild directionality of the subsequent formability parameters (ε_n and n), the greatest deformation-induced anisotropy is seen in the yield strength ($R_{p0.2}$), and to a lesser extent, in the ultimate tensile strength (σ_n). For

example, the 0.2% offset tensile flow stress in the original prestrain direction is about 850 MPa, while that in the orthogonal direction is about 600 MPa (a cross-softening effect of about 250 MPa).

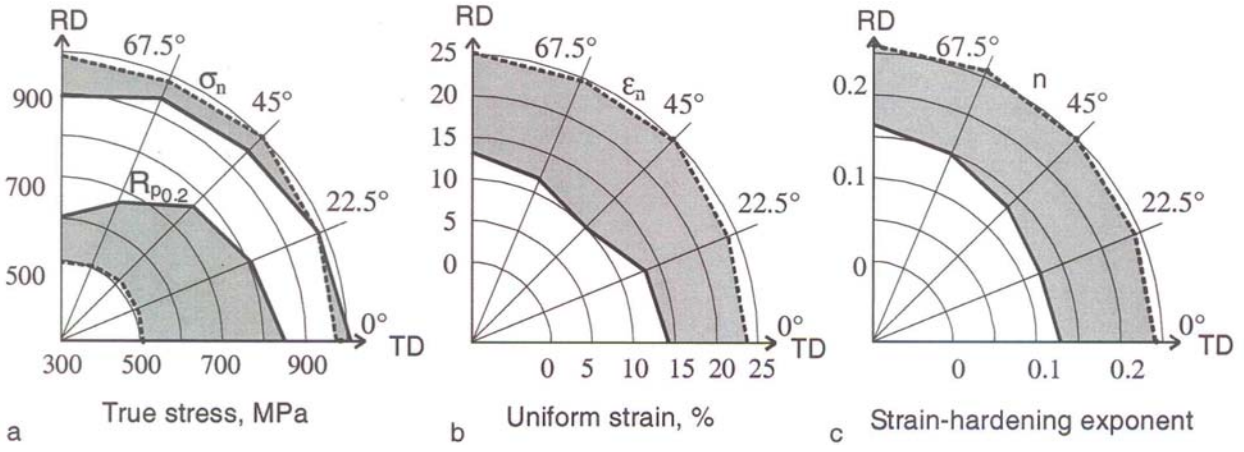

Figure 49: Anisotropic tensile properties in a TRIP steel induced by pre-deformation in uniaxial tension (66). The angles (degrees) mark the difference in the directions of applied tension during the prestrain step and during the secondary tensile deformation. See text for explanation.

Wasilkowska *et al*. (66) mentioned that the strongly anisotropic flow behavior could not be attributed to measured crystallographic texture changes induced by forming, and they loosely attributed this cross-softening effect to the austenite-to-martensite transformation characteristics of the metastable retained austenite. A corresponding strain-path-dependent dislocation substructure was cited as another possible contributing factor. No evidence was presented, however, to support this claim, or to suggest that dissimilar mechanisms are responsible for the observations of Wasilkowska *et al*. (66) and of Sugimoto *et al.* (65) [recall the significant presence of deformation-induced residual stresses in TRIP steels reported by Streicher (14) and by Sugimoto *et al.* (52)]. Further discussion about the development of residual stresses in DP steels during forming, based on the theoretical treatment of Sugimoto *et al.* (65), is given in Section 6.2.1.

2.7.5 **Flow Softening Behavior**

Cross-hardening (latent work hardening) behavior in low carbon steels has been linked to differences in slip plane activity during primary (prestrain) and secondary deformation modes [Toyoda *et al.* (63)]. Often in the literature, the peculiar "cross-hardening" stress/strain behavior illustrated in Figure 47 is referred to as *flow softening*, *work softening*, or simply *softening*, thus adding to the potential of confusion. This paradox in nomenclature arises from the particular experimental approach and emphasis that each group of researchers has applied toward its investigations. Some researchers (primarily Japanese) have examined the in-plane directionality of subsequent tensile properties after prestrain in a particular deformation mode, such as in the works of Toyoda *et al.* (63) and Hasebe (64), where "cross-hardening" describes the relative tensile yield strength difference in the directions of the major and minor prestrain axes. A separate group of researchers (mostly European) has focused more on the apparent negative work hardening rate or "softening" that occurs *after* the initial "cross-hardening" effect. Thus, as a point of clarification, the cross-hardening effect is subsequently followed by flow softening, as shown by the transition region in Figure 47B.

Van Houtte *et al.* (67) described this flow softening behavior as potentially "disastrous" in sheet metal forming, as it would trigger a plastic instability that would likely lead to failure immediately after a strain path change. It was also generalized that this type of behavior occurs when the strain path change is intermediate between a full strain reversal (Bauschinger Effect) and monotonic loading (*i.e.*, where the secondary deformation mode is a continuation along the prestrain path). This distinction is shown schematically in Figure 50, where the "cross effect" (cross-hardening followed by flow softening) is shown in reference to monotonic loading and reverse loading (67).

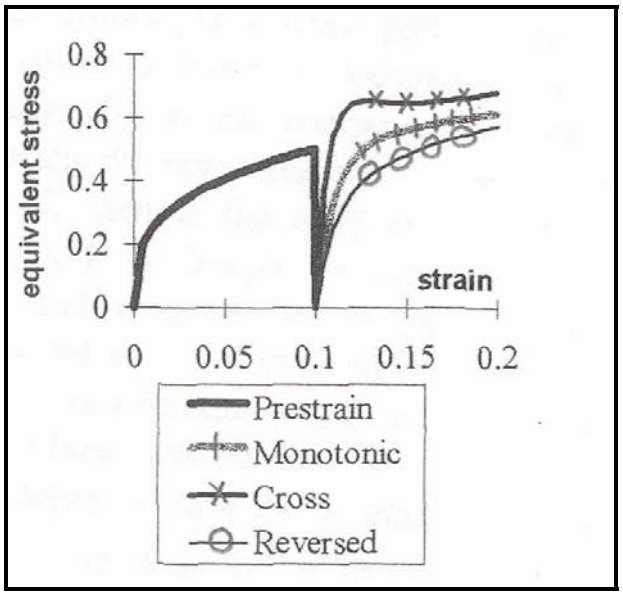

Figure 50: Schematic illustration of the influence of strain path changes on flow behavior [after (67)—modified]. The "Monotonic" curve represents continued deformation along the same strain path as the "Prestrain" step. The "Reversed" curve illustrates the Bauschinger Effect, where a complete strain reversal results in a lowered flow stress. The "Cross" curve shows the initial hardening and subsequent flow softening commonly observed in orthogonal strain path sequences.

An example of the evolution of flow softening behavior in a low carbon steel, from the work of Lopes *et al*. (68), is shown in Figure 51. Shown are shear stress/strain (τ/γ) curves for the complex strain path of plane strain rolling ($\varepsilon_{min} = 0$) followed by pure shear deformation (zero thickness strain) in the transverse direction (90° to the rolling direction). Clearly, as the amount of rolling prestrain increases, the tendency for flow softening and negative work hardening increases. It is important to realize that, for pure shear deformation, true stress/strain data are obtainable over a large range of plastic strain, as geometric necking instabilities (as observed in tension tests) are not physically possible. Thus, the shear stress/strain curves in Figure 51 are indeed a real reflection of the work hardening behavior that is unperturbed by sample thinning during tensile deformation. As such, shear stress/strain tests may be more appropriate for a mechanistic analysis of work hardening behavior at large strains, albeit

conceptually more difficult to appreciate. On the other hand, as most sheet metal failures occur by excessive thinning and strain localization, it is more practical to consider stretching modes of deformation in the context of forming limits and general formability.

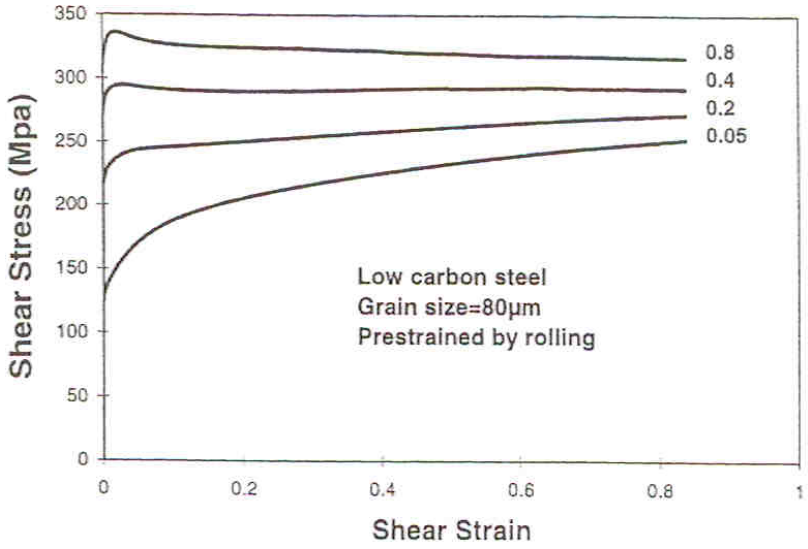

Figure 51: Orthogonal shear stress/strain curves for a low carbon steel prestrained by rolling (68). The shear direction is perpendicular to the rolling direction.

While Sharp and Makin (69) may have been the first to illustrate latent work hardening and flow softening in copper single crystals, Rauch and G'Sell (70) were likely the first to identify a possible contributing mechanism of flow softening in complex strain paths involving polycrystalline engineering metals. They attributed this phenomenon to the concurrence of shear microband localization and destabilization of the dislocation substructure established during the prestrain step. Examples of such shear band localization are shown in Figure 52 from the works of Lopes *et al.* (68) and of Bacroix *et al*. (71). Figure 52A, shows a TEM micrograph of shear band localization for the case of rolling prestrain followed by shear strain ($\gamma = 0.15$) in the direction perpendicular to the prior rolling direction, as indicated by the diagram in the bottom right corner. For this particular image, it is explained that two adjacent ferrite grains share the

same (101) slip plane, as indicated by the white line parallel to the localized shear bands. The offset or jog in the grain boundary reflects the sharp strain localization associated with the microbanding (68) (note: the grain boundary is the irregular feature situated approximately 45° from the white line and the corresponding shear microbands). The microbands are aligned parallel to the slip planes, and correspond to single slip on a severely stressed slip system. Unfortunately, the dislocation substructure generated during the rolling prestrain step is barely visible in this particular image.

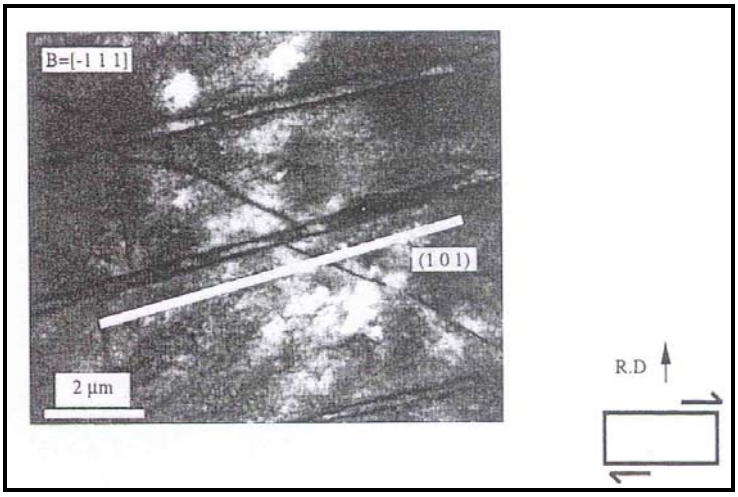

(A)

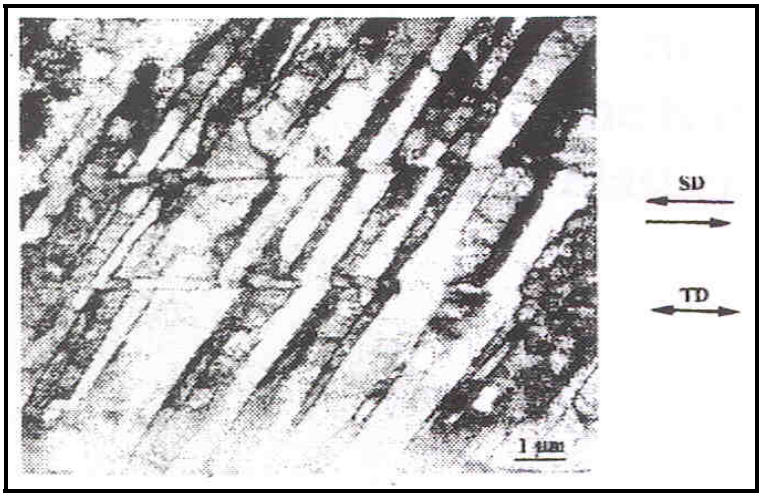

(B)

Figure 52: Examples of shear band localization in complex deformation modes—(A) plane strain rolling followed by orthogonal shear (68) and (B) uniaxial tension followed by shear applied parallel to the original tensile axis (71). See text for details.

A similar situation is shown in Figure 52B for the sequence of uniaxial tension prestrain (10% strain) followed by applied simple shear (10% strain) parallel to the major prestrain direction (original tensile axis). For clarity, the small diagram in the lower right corner of Figure 52B illustrates the direction of applied tension during the prestrain step (TD), and the subsequent applied shearing direction (SD) is shown parallel to TD. In this figure, the regular, brick-like dislocation cell structure typical of uniaxial tension deformation (see Figure 43A) is aligned approximately 55° from TD, and the shear microbands are parallel to TD and SD. This particularly clear example shows that the array of dislocations established during the prestrain step is not suited for sustained deformation in the secondary pure shear deformation mode, and that a micro-deformation mode of lesser resistance was assumed in response to the applied shear. It is not known whether such shear band localizations occur for other types of subsequent deformation (*e.g.*, subsequent uniaxial tension rather than simple shear).

Although it is generally accepted (68-74) that flow softening effects (negative work hardening rates) occur after an initial latent work hardening effect (see Figure 47 and Figure 51), there is considerable disagreement regarding the conditions under which this phenomenon occurs, and regarding the responsible mechanisms. Rauch and G'Sell (70), in 1989, observed shear microband localization in steel (and associated flow softening) in orthogonal strain path changes only at very high prestrain levels; while at low prestrains, only a "transient stagnation of the stress/strain curve" (an inflection in the stress/strain curve, but no negative work hardening rate) was observed—with no associated shear band localization. Recall that an orthogonal strain path change is one where the major strain axis of the primary and secondary deformation modes are perpendicular, or at least unparallel. Rauch (74) recently proclaimed, in 1997, that such behavior is strictly unrelated to dislocation substructure, but rather that dislocation *density* is

most important. More recently (in 1999), Lopes, Rauch and Gracio (68) concluded that flow softening has a structural (dislocation based) origin in steels, but is related to crystallographic texture effects in aluminum alloys. Just a few years later, in 2005, the same group of researchers (73) concluded that texture effects are *not* responsible for flow softening in aluminum alloys. The point of the preceding summary of contradictory statements is to illustrate the lack of a definitive explanation for the observed behavior illustrated in Figure 47 and Figure 51 and to emphasize the fertility of this particular aspect of material behavior in terms of future research. Additionally, and perhaps more importantly, is the observation made by Sugimoto *et al*. (65) and by Wasilkowska *et al*. (66) (section 2.7.4) that multiphase steels (DP steels and TRIP steels) are apparently devoid of latent work hardening effects and subsequent flow softening effects in orthogonal strain path changes.

3.0 STATEMENT OF OBJECTIVE

It is hypothesized that, in dual-phase steels, strain partitioning between ferrite (α) and martensite (α') during deformation results in a distribution of post-deformation residual stresses that, in turn, affects the subsequent strength, work hardening behavior and formability when the strain path is changed. The deformation-induced residual stress *state* is expected to depend upon the microstructure, the amount of strain and the strain path associated with the primary deformation (prestrain). In complex forming processes that involve strain path changes, it is anticipated that the effects of the residual stresses formed during primary deformation will depend upon the strain path of the subsequent deformation (secondary strain). The primary objective for this research program is given below.

PRIMARY OBJECTIVE

To understand the influence of deformation-induced residual stresses on the post-forming tensile stress/strain behavior of dual-phase steels.

4.0 EXPERIMENTAL PROCEDURES

4.1 MATERIAL SELECTION

Selection of an appropriate group of test materials was the important first step toward reaching the objectives of this research program. Although the focus of this study is on the behavior of dual-phase (DP) steels, it is important to have control materials as a basis for comparison and contrast. A dual-phase (DP) sheet steel, a conventional high-strength low-alloy (HSLA) sheet steel, and a conventional ultra-low-carbon interstitial free (IF) steel—all produced commercially by United States Steel Corporation (USS)—were included in this analysis. Commercially produced materials were chosen, as a large amount of material with uniform properties was required for the experiments. The nominal compositions of the test materials are given in Table III.

Table III: Nominal Steel Compositions (weight percent)

Steel	C	Mn	Al	N	Ti	Nb	Cr	Mo
IF	0.003	0.1	0.04	0.003	0.06	--	--	--
HSLA	0.070	0.5	0.03	0.007	--	0.04	--	--
DP	0.075	1.9	0.05	0.006	--	--	0.2	0.2

The IF steel has a soft, single-phase ferrite microstructure (inasmuch as a DP steel has a two-phase microstructure), and represents the ferrite behavior in the absence of martensite. If the effects of a dual-phase microstructure are to be understood, the single-phase case must be

appreciated first. The as-produced mechanical properties of the IF steel and the DP steel are very different, as they were developed to meet two very different engineering needs. That is, the IF steel is designed for maximum formability, while the DP steel is designed to achieve a compromised strength/ductility balance to meet the safety and environmental demands discussed in the Introduction (Section 1.0). It is therefore necessary to consider a conventional high strength steel at a similar strength level as the dual-phase steel. The HSLA steel (strengthened primarily by grain size refinement) was selected as the second control material. Like the IF steel, the HSLA steel has essentially a single-phase microstructure (in contrast to the DP steel), albeit with a finer ferrite grain size; a dispersion of fine, spheroidized cementite particles; a solid solution strengthening addition of Mn; and a dispersion of very fine microalloy (Nb) carbo-nitrides (various conventional strengthening mechanisms employed during the grade development).

The IF steel [gage: 2 mm (0.079 in)] and the HSLA steel [gage: 1.7 mm (0.067 in)] were continuously cast, hot rolled, cold rolled, batch annealed and temper rolled at USS Gary Works in Gary, Indiana. The DP steel [gage: 1.6 mm (0.063)] was processed through cold rolling at Gary Works, and subsequently in-line annealed, coated and temper rolled on a continuous hot-dip galvanizing line at PRO-TEC Coating Company of Leipsic, Ohio. A general description of each steel is given in Table IV, and further characterization of the IF, HSLA and DP steels is provided in Section 5.1. The presence of the hot-dip galvanized Zn coating is not expected to influence the behavior of the DP steel significantly, in terms of tensile stress/strain behavior. The relatively soft Zn coating (~ 7 μm thick on each surface) comprises less than 1% of the total cross section of the DP steel. The surface characteristics of each material influence primarily the practical limits of deformation in the prestraining stage of the analysis (next section).

Table IV: Description of Commercially Produced Steels

Steel	Gage (mm)	Coating Type	Annealing Process	Average Ferrite Grain Diameter	General Description
IF	2.0	None	BA	15 μm	Ultra-low carbon, Ti-stabilized interstitial free steel.
HSLA	1.7	None	BA	5 μm	Low-carbon steel microalloyed with Nb. Uniform low-volume-fraction dispersion of spheroidized cementite (<0.5 μm).
DP	1.6	HDGI	CA	7 μm	Dual-phase steel alloyed with C, Mn, Cr and Mo. About 15 vol. % martensite (~1μm) primarily concentrated at ferrite grain boundaries.

HDGI = hot dip galvanized; BA = batch annealed; CA = continuous annealed (CGL)

4.2 PRESTRAINING

Prestraining was achieved by binder-constrained stretch forming on an MTS Systems Corporation Model 866 Metal Formability System at the U.S. Steel Research & Technology Center, Monroeville, Pennsylvania. The forming tools consist of a cylindrical Marciniak-type 200 mm (8-in) diameter recessed punch and a 305 mm (12 in) outer diameter lock bead binder. All tests were run with an 890 kN (200 kip) binder clamp force with a servo-hydraulic punch (actuator) displacement rate of 12.7 mm/min (0.5 in/min). MoS_2 grease was used as lubricant between the punch and the testpiece.

For the balanced biaxial stretching (BB) condition, a 305 x 305 mm (12 x 12 in) square specimen was used (fully constrained in the binder). Trial-and-error was used to determine the appropriate specimen dimensions for uniaxial tension (UT) and plane strain (PS) prestrain. For the PS deformation mode, a 305 x 264 mm (12 x 10-3/8 in) rectangular panel was used; and for the UT deformation mode, a 305 x 152 mm (12 x 6 in) rectangular panel was used. For all

prestrain conditions, the sheet rolling direction (or longitudinal, L, direction) was aligned with the major deformation axis ($\varepsilon_{maj} = \varepsilon_L$), and the major and minor surface strains (ε_L and ε_T) were determined from the dimensional changes of a 50 mm diameter circle scribed in the center of each panel before deformation. Samples were prestrained to various levels along each strain path, and Table V lists the maximum achievable major strain for each material/strain path combination (*i.e.*, the limit above which splitting failures were observed at the forming punch shoulder radius). After prestraining, tensile specimens were machined from the center of each panel in the longitudinal (rolling), L, direction or the transverse, T, direction. A compilation of all the prestrain conditions is given in Table VI. The general testing methodology is shown schematically in Figure 53, and Figure 54 shows the complex strain paths associated with this methodology in surface strain space (ε_{maj}-vs-ε_{min})—see Sections 2.7.1 and 2.7.2.

Table V: Summary of Prestrain Conditions

Prestrain Mode ($\varepsilon_{maj} = \varepsilon_L$)*	Code	Specimen Width mm (in)	Maximum ε_{maj}		
			IF	HSLA	DP
Uniaxial Tension	UT	152 (6)	0.180	0.074	0.096
Plane Strain	PS	264 (10.375)	0.127	0.092	0.099
Balanced Biaxial	BB	305 (12)	0.103	0.071	0.073

*ε_L = Strain in the longitudinal (L) direction (sheet rolling direction)

4.3 TENSILE TESTING

Sub size ASTM-E8 tensile specimens were used for all tensile tests. Specimen length is 152-mm (6-in), and the width of the grip section is 12.7-mm (0.5-in). The reduced section is 31.8-mm (1.25-in) long and 6.4-mm (0.25-in) wide with a 0.025-0.076-mm (0.001-0.003-in) taper (to encourage localized necking within the gage section). The gage length is 25.4-mm (1-in), and the servo-hydraulic actuator speed during testing was 2.5-mm/min (0.1-in/min) to failure. R-

values (normal anisotropy parameters) were determined at 10% tensile elongation with non-tapered specimens according to ASTM Standard E517. For each test stress/strain data were recorded digitally with commercially available MTS data acquisition/test control software.

Table VI: Compilation of Prestrained Specimens*

Steel	Secondary Tension in L-direction						Secondary Tension in T-direction					
	UT Prestrain		PS Prestrain		BB Prestrain		UT Prestrain		PS Prestrain		BB Prestrain	
	ε_{maj}	ε_{min}	ε_{maj}	ε_{min}	ε_{maj}	ε_{min}	ε_{maj}	ε_{min}	ε_{maj}	ε_{min}	ε_{maj}	ε_{min}
IF	0.028	-0.021	0.016	0.002	0.011	0.013	0.031	-0.018	0.018	0.001	0.012	0.012
	0.053	-0.038	0.035	0.002	0.027	0.029	0.053	-0.039	0.036	0.002	0.029	0.028
	0.090	-0.062	0.065	0.001	0.053	0.052	0.088	-0.061	0.067	0.004	0.051	0.050
	0.134	-0.090	0.090	0.002	0.074	0.077	0.135	-0.089	0.088	0.001	0.079	0.075
	0.176	-0.115	0.126	0.001	0.103	0.101	0.180	-0.113	0.127	0.001	0.101	0.100
β-ave	-0.70		0.05		1.05		-0.66		0.05		0.98	
HSLA	0.017	-0.009	0.012	0.000	0.010	0.009	0.020	-0.011	0.014	0.000	0.009	0.009
	0.043	-0.020	0.031	0.001	0.023	0.023	0.045	-0.018	0.034	0.000	0.022	0.020
	0.054	-0.028	0.054	0.000	0.035	0.029	0.055	-0.026	0.054	0.000	0.031	0.031
	0.073	-0.035	0.080	0.000	0.041	0.033	0.074	-0.037	0.080	0.000	0.052	0.037
	--	--	0.089	-0.002	0.071	0.054	--	--	0.092	0.000	0.066	0.064
β-ave	-0.51		0.01		0.87		-0.49		0.00		0.92	
DP	0.020	-0.013	0.012	0.000	0.006	0.006	0.020	-0.013	0.012	0.000	0.006	0.006
	0.039	-0.023	0.040	0.000	0.024	0.019	0.041	-0.024	0.039	0.000	0.022	0.019
	0.064	-0.032	0.057	0.000	0.031	0.032	0.060	-0.034	0.057	0.000	0.034	0.031
	0.076	-0.043	0.073	-0.001	0.045	0.042	0.080	-0.041	0.074	0.000	0.047	0.046
	0.095	-0.052	0.099	0.001	0.070	0.070	0.096	-0.051	0.092	-0.001	0.073	0.071
β-ave	-0.57		0.00		0.94		-0.56		-0.01		0.94	

*For all conditions, the major strain (ε_{maj}) is in the longitudinal (L) direction (rolling direction).

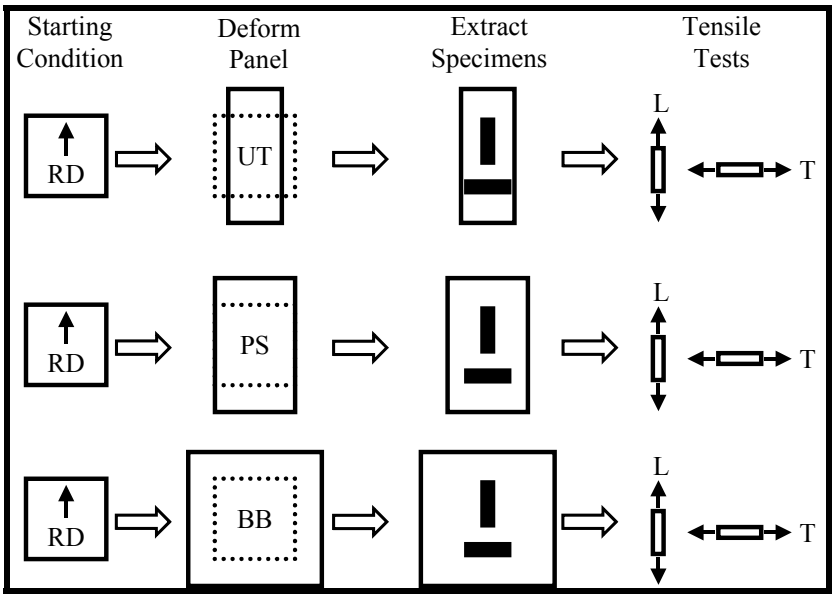

Figure 53: Test methodology for complex deformation sequences. For each prestrain condition, the major strain (ε_{maj}) is in the longitudinal, L direction (sheet rolling direction or RD). The prestrain deformation modes are uniaxial tension (UT), plane strain (PS) and balanced biaxial stretching (BB). Subsequent tensile tests were run in L direction and in the transverse, T direction (90° to the sheet rolling direction).

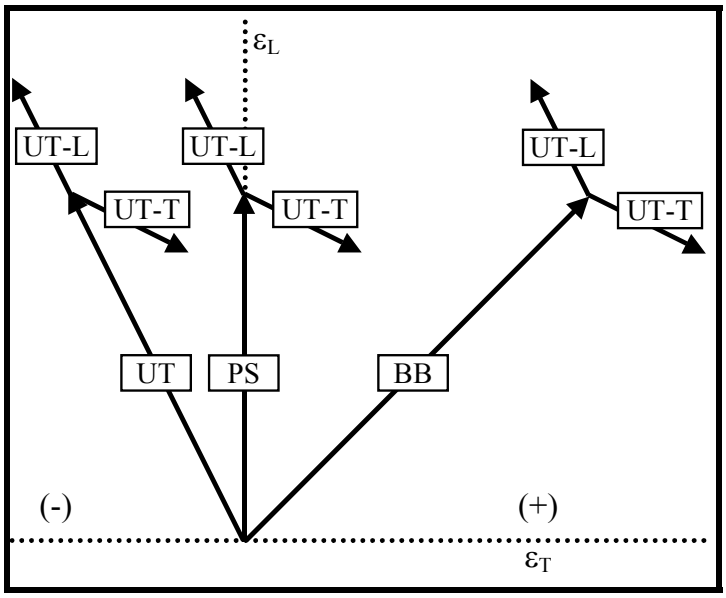

Figure 54: Schematic illustration, in surface strain space, of the various complex (2 stage) deformation modes considered in this analysis. The primary deformation (prestrain) modes are uniaxial tension (UT), plane strain (PS) and balanced biaxial stretching (BB). Note that, for the various prestrain modes, the major strain is in the longitudinal (sheet rolling) direction ($\varepsilon_{maj} = \varepsilon_L$) by convention. Correspondingly, the minor strain is in the transverse direction ($\varepsilon_{min} = \varepsilon_T$). These complex strain paths are represented in the test methodology in Figure 53 above.

4.4 RESIDUAL STRESS DETERMINATION BY NEUTRON DIFFRACTION

4.4.1 **Brief Background on Neutron Diffraction**

Neutron diffraction stress measurement utilizes the phenomenon of neutrons scattering in crystalline media. If a neutron beam with wavelength λ passes through a crystalline material it produces so-called Bragg reflections (or peaks) at specific angles (measured relative to the direction of the incident beam), described by Bragg's law

$$n\lambda = 2d_{hkl} \sin\theta \qquad [18]$$

where d_{hkl} is the lattice plane spacing, θ is the angle of incidence to the reflecting planes, and n is the order of reflection (79). Stresses affect lattice spacing by stretching or contracting the lattice so that slight changes of lattice plane spacings (not more than the elastic limit of the material—usually <0.1% change) causes a corresponding small shift in position of a diffraction peak (*i.e.*, Bragg's law is satisfied at a different angle, θ). Modern neutron diffraction techniques allow routine measurement of these small shifts with an accuracy of 0.001% or better (80). Stress estimates can be made with an uncertainty of a few MPa. Depending on experimental requirements, the neutron sampling (gage) volume can be changed from several tenths of mm^3 to several hundreds of mm^3 to provide the necessary accuracy over the required material mass.

The measurement of stress by means of neutron diffraction has several advantages over other methods. Thermal neutrons (with wavelength on the order of 1 Å) have very high penetration with respect to typical diffraction-regime X-rays. In steel, for example, the half-value thickness (or the thickness for half-attenuation) for a thermal neutron beam is approximately 6 mm (in contrast to 3 μm for 1.54Å x-rays) while aluminum is even more neutron transparent with a half-value thickness around 70 mm (50 μm for 1.54 Å X-rays).

Because of this high penetration, subsurface measurements (up to 10 cm) are possible with neutrons, while conventional X-ray diffraction is limited to surface measurements (several tenths of a micron deep). This makes neutron stress measurements a more attractive nondestructive method, compared with destructive relaxation methods that involve cutting and drilling (80).

High penetration also allows determination of the entire strain tensor by measuring changes in lattice plane spacing and calculating elastic strains as

$$\varepsilon = \ln(1+e) \approx e = \frac{d}{d_0} - 1 \text{, (small e)} \qquad [19]$$

in various directions in the sample (d_0 is some reference state value normally regarded as the "stress free" lattice plane spacing). From the measured strains, the complete stress tensor can be reconstructed by employing (81)

$$\sigma_{ij} = \frac{E_{hkl}}{1+\nu_{hkl}}\varepsilon_{ij} + \frac{\nu_{hkl}E_{hkl}}{(1+\nu_{hkl})(1-2\nu_{hkl})}\varepsilon_{kk}\delta_{ij}\,. \qquad [20]$$

Expansion of Equation 20 gives three equations for normal stress and six equations for shear stress (77). In contrast, X-ray techniques, being surface methods, are planar and thus provide information only on normal and shear stresses in the surface plane of the sample (80).

The appropriate choice of E (Young's modulus) and *v* (Poisson's ratio) in Equation 20 is not a trivial matter. The subscript "hkl" refers to the specific set of lattice planes (Laue indices) for which the d-spacings were determined for strain calculations. E_{hkl} and ν_{hkl} are the elastic proportionality constants for a stress that is applied normal to a particular set of {hkl} planes. For cubic-lattice crystals, a lattice direction [uvw] is normal to a lattice plane (hkl) when u = h, v = k, and w = l. As an example, E_{211} is the Young's modulus in any of the <211> directions, and the d-spacings (for strain calculations) are for the {211} family of reflecting planes. The so-

called “diffraction elastic constants” are typically measured experimentally, estimated or calculated (80).

4.4.2 **Neutron Diffraction at NIST**

Neutron diffraction experiments were performed at the National Institute of Standards and Technology (NIST) in Gaithersburg, Maryland. Samples were sent to the NIST Center for Neutron Research (NCNR) where the BT8 Residual Stress Neutron Diffractometer and the reactor are housed. One sample of each material (IF steel, HSLA steel and DP steel) was prepared in each of the following conditions:

- As-produced (no prestrain)
- Prestrained to 5% major strain in uniaxial tension (UT)
- Prestrained to 5% major strain in plane strain (PS)
- Prestrained to 5% major strain in balanced biaxial stretching (BB).

For each of the prestrain conditions above, the major strain axis was aligned with the sheet rolling direction [or longitudinal (L) direction] and was prepared according to the procedures outlined in Section 4.2 above. The reflecting plane spacings in ferrite for the {200} and {211} families of planes were determined by NIST in the assumed principal directions: 1 – longitudinal (L) direction or sheet rolling direction, 2 – transverse (T) direction (90° to the rolling direction), and 3 – the sheet normal or thickness direction. Altogether, seventy-two d-spacings were determined (3 materials x 4 conditions x 3 principal directions x 2 reflection types = 72 d-spacings). An approximate gage volume of 7 mm^3 was sampled for each measurement.

4.4.3 **Calculation of Deformation-Induced Residual Stress**

In addition to selecting the appropriate diffraction elastic constants, it is also important to determine the appropriate reference d-spacing (d_0) of the often hypothetical "unstressed lattice" (in Equation 19), especially when one is interested in absolute values of residual stresses. Unfortunately, for neutron diffraction the d_0-value is usually unknown or cannot always be easily measured precisely (82). This condition is made worse by the inevitable elemental compositional variability within a phase within a material. However, for this analysis, *deformation-induced* residual stress components are of specific interest. Assuming linear elasticity, the d-spacings of each of the "as-produced" samples of each material in each respective principal direction may be used as the respective reference d_0-values. In addition, if one is primarily interested in the deviatoric residual stress components that affect yielding behavior, then the selection of d_0-values is actually arbitrary. In perspective, as long as "appropriate" diffraction elastic constants are used for stress calculations, any "reasonable" d_0-value may be used as long as it is used consistently and as long as hydrostatic or mean stress values are not needed for the analysis. With this simplification, Equation 19 becomes

$$\varepsilon = \ln(1+e) \approx e = \frac{d}{d_{as-produced}} - 1, \text{ (small e).} \qquad [21]$$

Once the strains in each of the assumed principal directions are determined, Equation 20 leads to the following equations for the principal stress components:

$$\sigma_{dr,1} = \frac{E_{hkl}}{(1+\nu_{hkl})}\left[\varepsilon_1 + \frac{\nu_{hkl}}{(1-2\nu_{hkl})}(\varepsilon_1+\varepsilon_2+\varepsilon_3)\right], \qquad [22a]$$

$$\sigma_{dr,2} = \frac{E_{hkl}}{(1+\nu_{hkl})}\left[\varepsilon_2 + \frac{\nu_{hkl}}{(1-2\nu_{hkl})}(\varepsilon_1+\varepsilon_2+\varepsilon_3)\right], \text{ and} \qquad [22b]$$

$$\sigma_{dr,3} = \frac{E_{hkl}}{(1+\nu_{hkl})}\left[\varepsilon_3 + \frac{\nu_{hkl}}{(1-2\nu_{hkl})}(\varepsilon_1+\varepsilon_2+\varepsilon_3)\right], \quad [22c]$$

where the subscripts 1, 2 and 3 again refer to the assumed principal directions defined by sample symmetry [1 – longitudinal (L) or rolling direction, 2 – transverse (T) direction, and 3 – sheet normal (thickness) direction]. Alternatively, principal directions 1, 2 and 3 may be called the x, y and z directions. The subscript prefix "dr" refers to deformation-induced residual stresses. This designation will be propagated throughout the discussion to distinguish these calculated stresses from more general residual stress components that exist in the materials in the as-produced condition. For calculating the σ_{dr} components, the following diffraction elastic constants were reported by NIST (80):

For {200} reflections: E_{200} = 175,199 GPa, ν_{200} = 0.331

For {211} reflections: E_{211} = 224,593 GPa, ν_{211} = 0.284.

5.0 RESULTS

5.1 AS-PRODUCED MATERIAL CHARACTERIZATION

5.1.1 **Microstructures**

Example scanning electron microscope (SEM) images of the microstructures of each test material are given in Figure 55 at 400X and 1000X original magnification. Clearly, the IF steel microstructure is much coarser than those of the HSLA steel and DP steel, as the latter microstructures are barely resolvable at the lower magnification. The average ferrite grain diameter of the IF steel is about 15 microns, while the HSLA has an average grain diameter of about 5 microns, and the DP steel ferrite grain structure is slightly coarser at about 7 microns average grain diameter. The average ferrite grain diameters were determined by Jeffries' Planimetric method (75) from the average of five independent fields of view at 1800X magnification (HSLA and DP steel) and 700X magnification (IF steel). Figure 56 shows higher magnification images of the HSLA steel and the DP steel (5000X original magnification), where the microstructural features are clearly observed. The HSLA steel consists of equiaxed ferrite of non-uniform size distribution with a low-volume-fraction dispersion of spheroidized Fe_3C (cementite) particles. The cementite (light gray/white) is distributed evenly throughout the ferrite matrix (dark gray) at both intragranular and intergranular locations. The DP steel in

Figure 56B has a similar ferrite structure (dark gray) as the HSLA steel with a significant presence of martensite (lighter grey) that nearly occludes the ferrite grains. The volume fraction of martensite in the DP steel is approximately 0.15 (15 pct)—determined by 100-point counting with a 90 mm by 90 mm translucent square grid at 1800X magnification (average of five independent fields of view). A similar analysis for the HSLA steel determined that the volume fraction of cementite is less than 1 pct. It is anticipated that the fine grain size and dispersion of spheroidized cementite in the HSLA steel will enhance the work hardening behavior in contrast to the coarser-grained, carbide-free IF steel (76).

5.1.2 **Tensile Properties and Work Hardening Behavior**

The as-produced tensile properties in both the longitudinal (rolling) direction and the transverse direction are given in Table VII. The IF steel is significantly softer and more ductile than both the HSLA and DP steel with lower yield strength and ultimate tensile strength; and higher uniform elongation and total elongation. The HSLA steel and the DP steel have similar yield strengths with higher yield strength in the T direction. The HSLA has slightly higher uniform and total elongation values than the DP steel. The major difference between the HSLA and DP steel is that the DP steel has a much higher ultimate tensile strength (YS/UTS = 0.6) than the HSLA steel (YS/UTS = 0.8). In the strain interval from 10 pct elongation to the end of uniform elongation (10/U), the work hardening exponents (n-values) of the DP steel and the HSLA steel are similar, but, in the interval from 4 pct to 6 pct elongation (4/6), the n-value of the DP steel is noticeably greater—a reflection of the high initial work hardening rate of the DP steel at low strains. In practice, n-values are typically determined and specified for DP steels in the 4 pct to 6 pct strain interval as an arbitrary measure of "dual-phase" behavior.

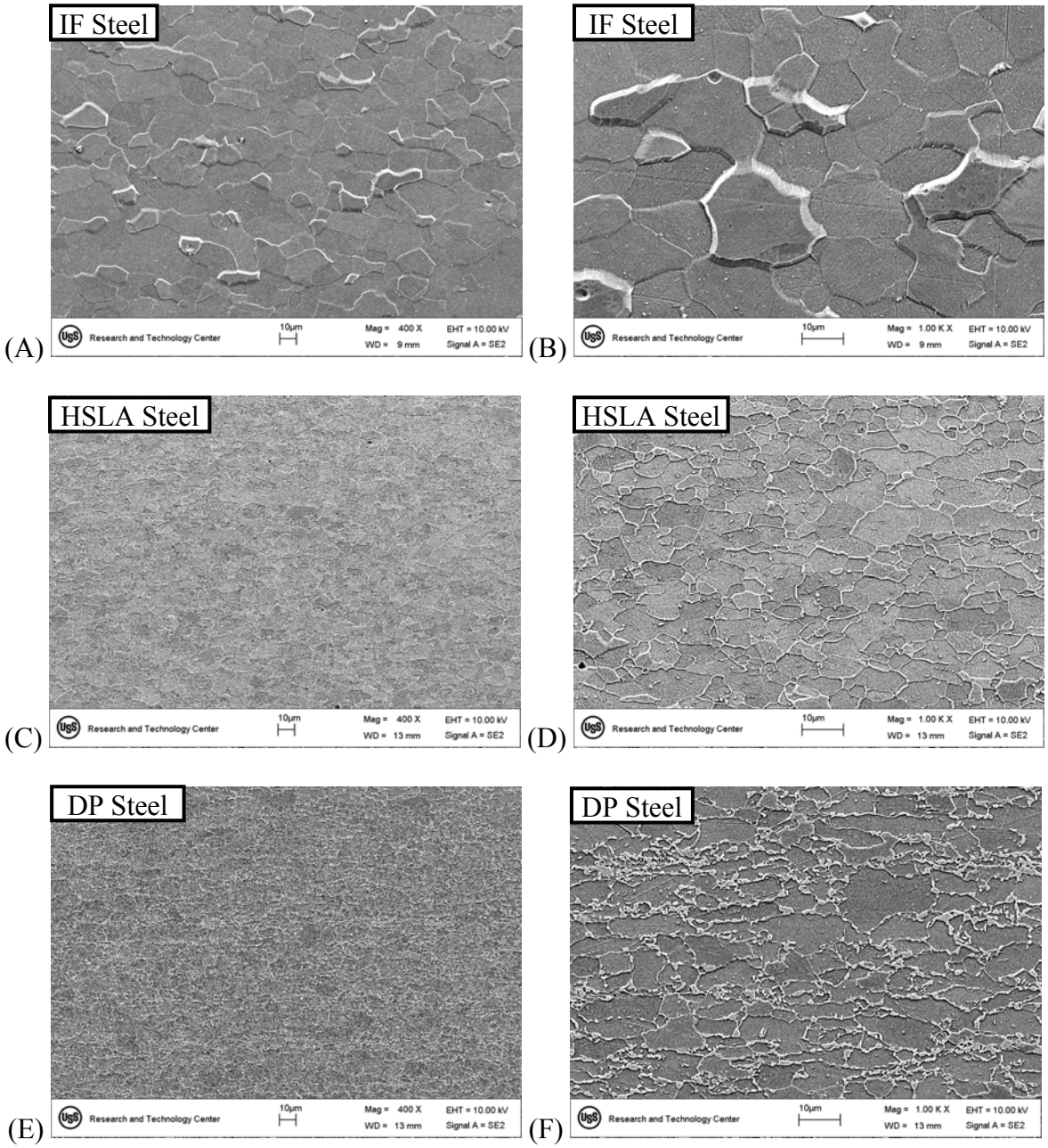

Figure 55: Microstructures of (A and B) IF Steel, (C and D) HSLA Steel, and (E and F) DP steel. Left column: 400X original magnification; Right column: 1000X original magnification. Polished longitudinal cross-sections etched with nital/picral mixture. SEM secondary electron images.

(A)

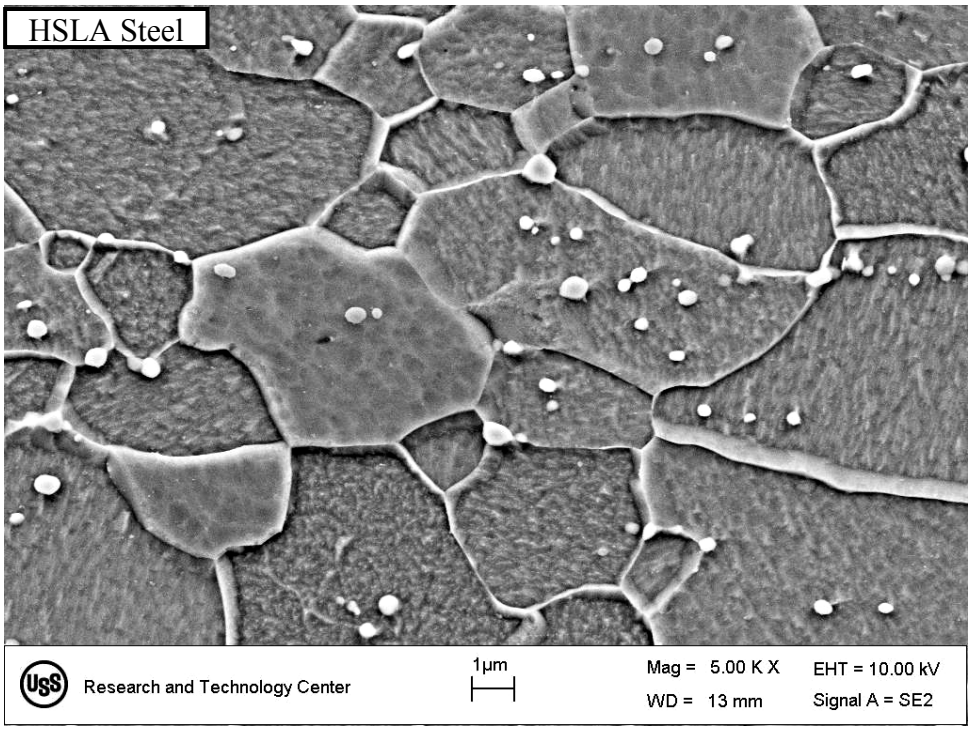

(B)

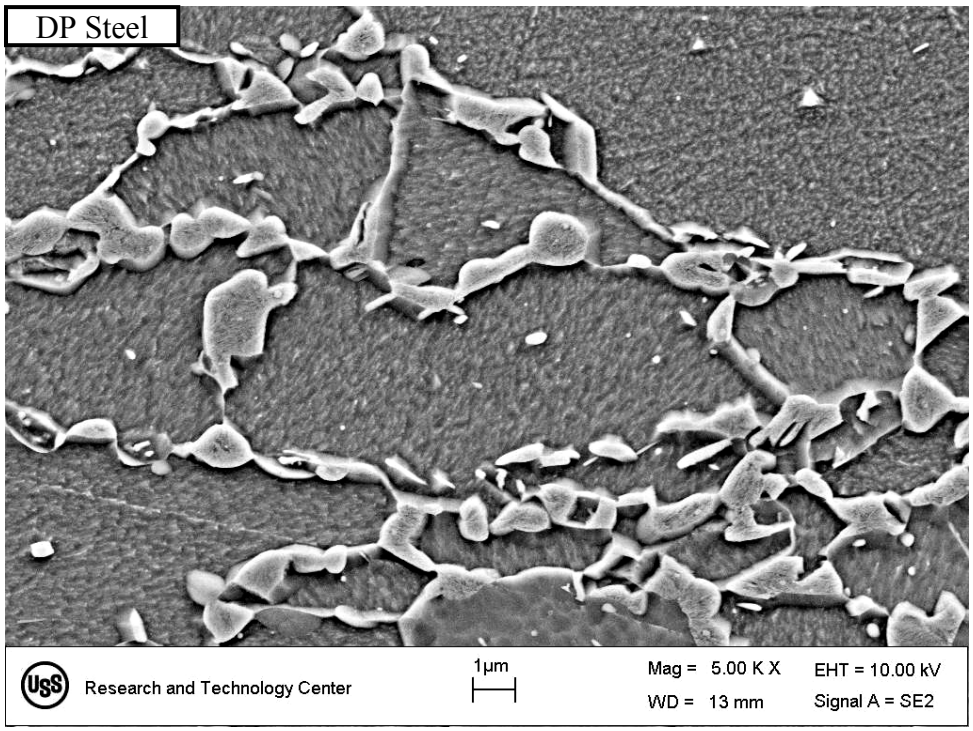

Figure 56: Higher magnification images of (A) HSLA steel and (B) DP steel. 5000X original magnification. Same sample preparation as in Figure 55.

Table VII: As-Produced Basic Tensile Properties

Steel	Direction	YS (MPa)	UTS (MPa)	YPE (%)	UEL (%)	TEL (%)	n (4/6)	n (10/U)
IF	L	161	299	0.0	27.7	49.3	0.30	0.25
	T	166	298	0.0	26.9	48.8	0.30	0.24
HSLA	L	350*	462	0.5	18.0	29.9	0.18	0.17
	T	387*	478	1.9	16.9	29.4	0.17	0.16
DP	L	344	612	0.0	16.9	26.5	0.21	0.16
	T	368	620	0.0	16.6	26.6	0.20	0.16

L = longitudinal (rolling) direction; T = transverse direction
YS = yield strength [0.2% offset flow stress or (*) lower YS]; UTS = ultimate tensile strength
UEL = uniform elongation; TEL = total elongation
n(4/6) = work hardening exponent ($\sigma = K\varepsilon^n$) from 4 to 6% elongation; n(10/U) = work hardening exponent from 10% elongation to the end of uniform elongation

Example engineering tensile stress/strain (s/e) curves of the IF steel, the HSLA steel and the DP steel in the as-produced condition are shown for the longitudinal (L) direction in Figure 57 and for the transverse (T) direction in Figure 58. Overall, the materials appear to be reasonably isotropic in terms of stress/strain behavior in the L and T directions. Minor differences are observed upon closer inspection at lower strains, especially for the HSLA material, where the yield point is more sharply defined in the T direction. Both the IF steel and the DP steel exhibit continuous yielding (no inflection in the s/e curve after yielding). Table VII also shows the greatest degree of L-vs-T anisotropy for the HSLA steel in terms of the reported tensile properties. The measured normal anisotropy parameters (R-values) are listed in Table VIII, where the anisotropy of the HSLA material is further exemplified. The DP steel is the least anisotropic material in terms of R-values with an R_m-value near 1.0 and ΔR value near 0.0, thereby epitomizing the essence of normal and planar isotropy. The IF steel is the most anisotropic in terms of average R-value ($R_m = 1.8$), while the HSLA steel shows the largest (*i.e.*, in magnitude) planar anisotropy ($\Delta R = -0.4$). It is likely that inherent anisotropy will play a role

in determining the post-forming properties of the HSLA steel and the IF steel. The low planar anisotropy exhibited by the DP steel is consistent with the early experimental results reported by Hayami and Furukawa (1) in 1977.

(A)

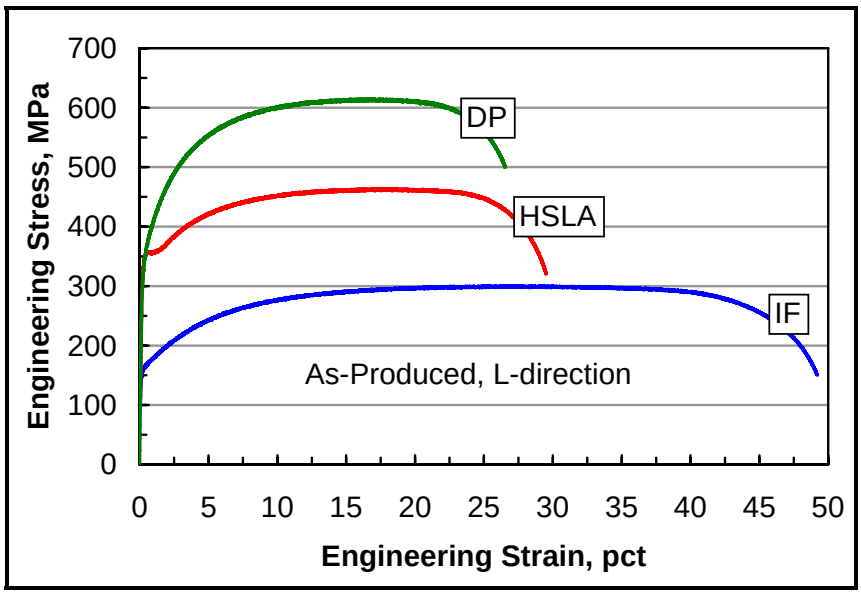

(B)

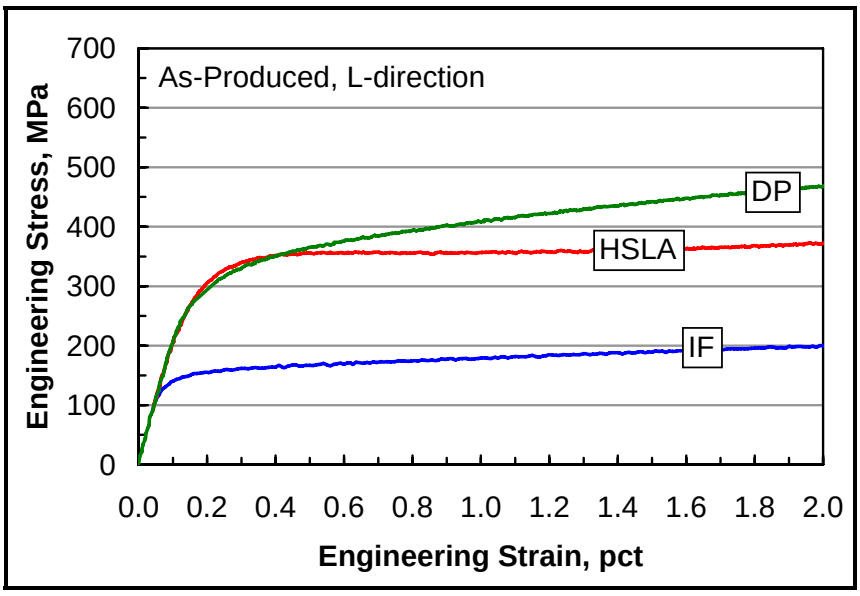

Figure 57: As-produced tensile engineering stress/strain curves in the longitudinal (L) direction (rolling direction, RD)—(A) full curves to failure, and (B) magnified at yielding.

(A)

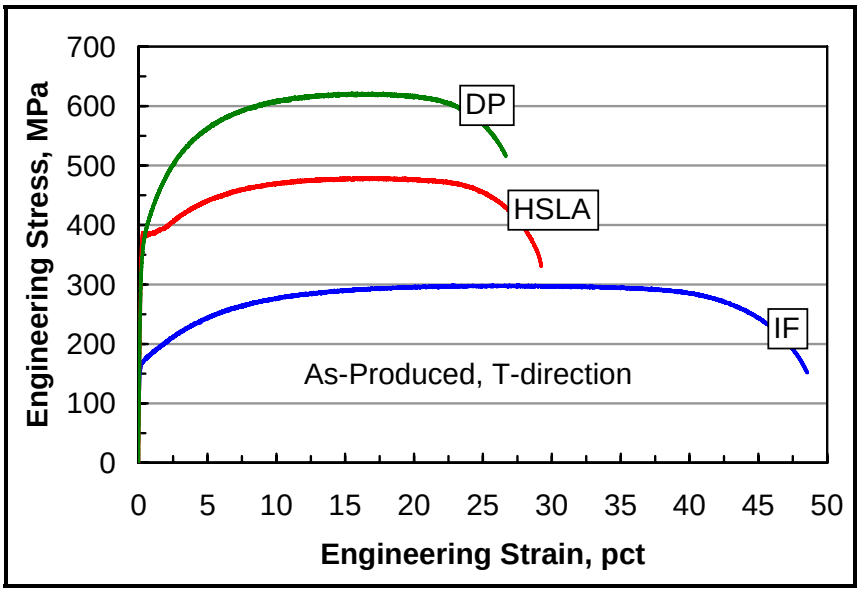

(B)

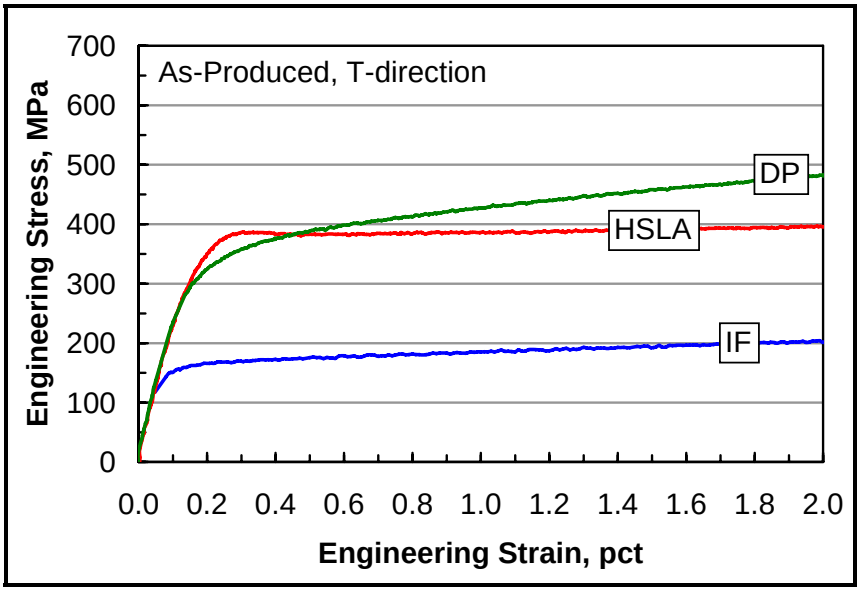

Figure 58: As-produced tensile engineering stress/strain curves in the transverse (T) direction (90° from the RD)—(A) full curves to failure, and (B) magnified at yielding.

Table VIII: Normal Anisotropy Parameters (R-Values*)

Steel	R_0	R_{45}	R_{90}	Mean Normal Anisotropy $R_m = ¼(R_0+2R_{45}+R_{90})$	Planar Anisotropy $\Delta R = ½(R_0-2R_{45}+R_{90})$
IF	1.74	1.66	2.14	1.80	0.28
HSLA	0.70	1.29	1.02	1.08	-0.43
DP	0.97	1.04	1.07	1.03	-0.02

*Determined at 10% elongation

Subscripts 0, 45 and 90 refer to the angle with respect to the sheet rolling direction

The characteristic "dual-phase" behavior of the DP steel is shown in Figure 59 where the work hardening rate (WHR) or tangent modulus ($d\sigma/d\varepsilon$) is plotted against true tensile strain, ε, up to the end of uniform deformation (necking). Note that at low strains (< 0.05), the WHR is several times greater than that of either the HSLA steel or the IF steel. At higher strains, the WHR of the DP steel decreases in a similar way as the other materials, albeit still higher at all strains. As expected from grain size and microstructure differences, the HSLA steel shows a slightly higher WHR than the IF steel at all strain levels.

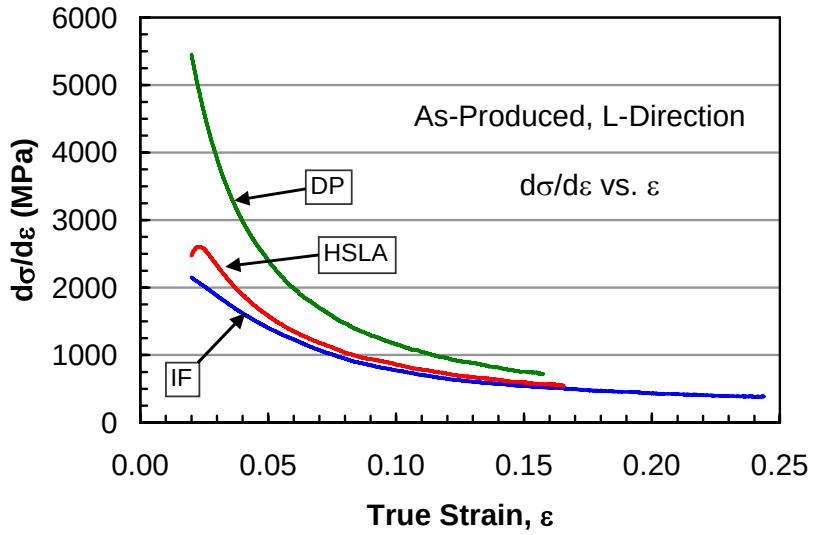

Figure 59: Work hardening rate ($d\sigma/d\varepsilon$) or tangent modulus as a function of tensile strain.

As the diffuse necking condition in a sheet tensile test is satisfied when the WHR is equal to the flow stress, $d\sigma/d\varepsilon = \sigma$ (77), the WHR may be normalize to the flow stress to determine the "work hardening potential". Higher work hardening potential indicates the ability to sustain uniform plastic deformation at high strength levels. Figure 60 shows the normalized WHR of each material as a function of true tensile strain, condensed on log-log scale for clarity. Shown in this way, $\ln[(d\sigma/d\varepsilon)/\sigma] = 0$ means that the necking condition, $d\sigma/d\varepsilon = \sigma$ has been satisfied

since ln(1) = 0 (*i.e.*, the work hardening potential is zero). This representation shows that the work hardening potential of the IF steel is initially high and remains high because of its low yield strength and low ultimate tensile strength. The actual (non-normalized) WHR of the IF steel is lowest among the three materials for all strain levels (Figure 59), but the high normalized WHR results in the large uniform elongation value for this material. The work hardening potential of the HSLA steel is initially low and remains low because of its high YS/UTS ratio. The DP steel initially exhibits a high work hardening potential at low strains because of its low YS/UTS ratio and extremely high actual work hardening rate ($d\sigma/d\varepsilon$). The combination of high tensile strength and rapidly diminishing WHR results in a rapidly diminishing work hardening potential as shown by the convergence of the HSLA and DP curves in Figure 60.

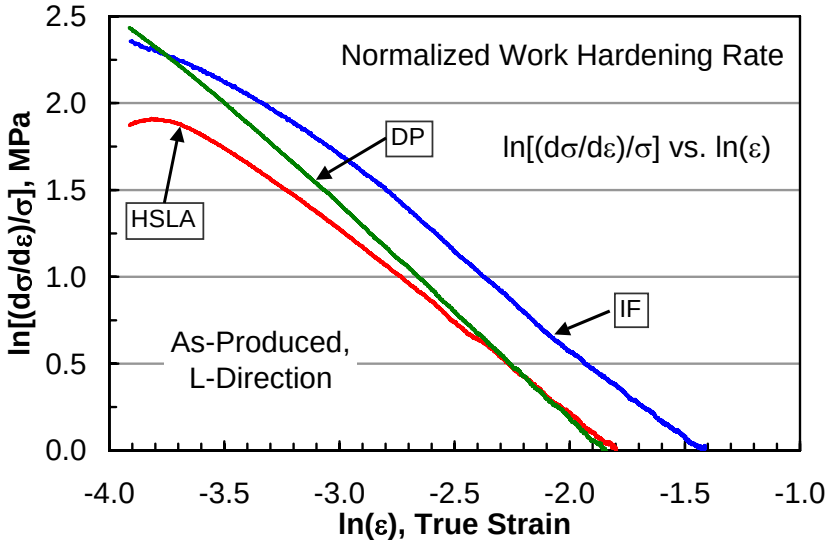

Figure 60: Normalized work hardening rate [$(d\sigma/d\varepsilon)/\sigma$] as a function of tensile strain.

Stout and Rollett (78) explained that, for two-phase alloys (*e.g.*, DP steels), the work hardening rate at low strains is much higher than that which can be attributed to conventional work hardening mechanisms associated with dislocation multiplication mechanics and

dislocation/particle interactions. It was suggested that the extreme apparent work hardening rates are a direct reflection of the development of long-range internal stresses caused by plastic incompatibility and strain partitioning between relatively hard and soft phases. Furthermore, as deformation continues, the rate of internal stress development diminishes, and work hardening behavior is dominated by more conventional mechanisms. This interpretation is certainly consistent with the WHR-vs-ε curves in Figure 59. Figure 61 illustrates the work hardening behavior near necking in reference to the true stress/strain (σ/ε) curves (L-direction). Although the work hardening rate of the DP steel has severely diminished at larger strains (ε > 0.1), it is sufficiently high to sustain uniform deformation similar to that of the HSLA steel, yet at a significantly higher strength level.

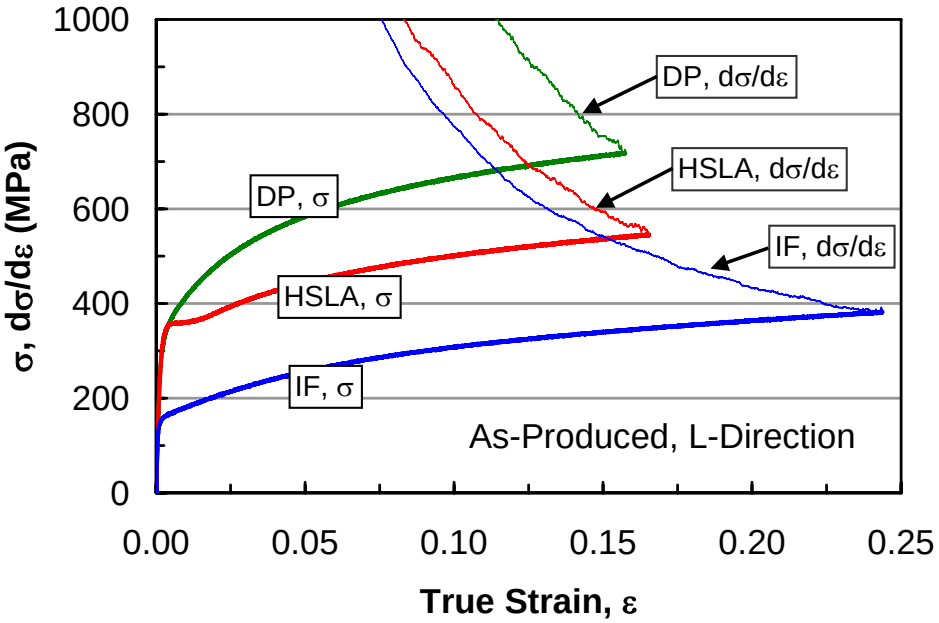

Figure 61: Example true stress/strain curves plotted to the end of uniform deformation. For each material, intersection of the true stress/strain curve with the work hardening rate (dσ/dε) curve marks the necking criterion (dσ/dε = σ).

5.2 NOTE ON EFFECTIVE STRESS AND EFFECTIVE STRAIN

Mechanical properties are often obtained by uniaxial tensile tests, as a large amount of useful information can be obtained regarding strength, ductility and work hardening behavior. However, sheet metal forming rarely involves uniaxial tension, and the effective strain concept has been developed to extrapolate uniaxial tension test data to more general stress states and strain paths (83). Conventionally, effective strain (ε_{eff}) is defined in terms of an effective stress (σ_{eff}) that is based upon a uniquely defined yielding criterion. In terms of principal components, effective strain may be defined such that the increment of plastic work per unit volume is

$$dw = \sigma_{eff}\, d\varepsilon_{eff} = \sigma_1 d\varepsilon_1 + \sigma_2 d\varepsilon_2 + \sigma_3 d\varepsilon_3 . \qquad [23]$$

An expression for effective strain is obtained by substituting an effective stress term into Equation 23 and solving for ε_{eff} with consideration of the flow rules for plastic deformation (84).

The maximum shear stress or Tresca yield criterion results in perhaps the simplest practical effective stress and effective strain relationships. The Tresca yield criterion states that yielding occurs when the maximum shear stress reaches a critical value, τ_c. The maximum shear stress in a unique stress state is equal to one half of the difference between the maximum and minimum principal stress (77) components. Thus, the yield criterion may be written as

$$2\tau_c = \sigma_{max} - \sigma_{min} , \qquad [24]$$

and the corresponding effective stress is

$$\sigma_{eff} = \sigma_{max} - \sigma_{min} . \qquad [25]$$

For uniaxial tension, the effective stress is the applied yield stress, σ_Y, where

$$\sigma_{max} - \sigma_{min} = \sigma_Y , \qquad [26]$$

since σ_{min} is zero. Thus, yielding is predicted for any arbitrary stress state when the difference between the largest and smallest principal stress components is equivalent to the yield strength in uniaxial tension. From this yield criterion, the following equations for effective stress and strain may be deduced by substituting Equation 25 into Equation 23 (84),

$$\varepsilon_{eff} = \left|\varepsilon_i\right|_{max}, \qquad [27]$$

where ε_i represents the set of three principal strains. The effective strain is equivalent to the absolute value of the principal strain of largest magnitude. For the three primary plane stress deformation modes (recall Figure 41 and Table II), Equation 27 gives (assuming isotropic material):

For uniaxial tension (UT): $\varepsilon_{eff} = \varepsilon_1$

For plane strain (PS): $\varepsilon_{eff} = \varepsilon_1 = -\varepsilon_3$

For balanced biaxial stretching (BB): $\varepsilon_{eff} = -\varepsilon_3 = 2\varepsilon_1 = 2\varepsilon_2$.

With effective stress and strain defined as in Equations 25 and 27, the uniaxial tension flow stress after non-uniaxial-tension deformation may be estimated with knowledge of the uniaxial tension flow curve (in the as-produced or reference state) and the strain history. The prestrain conditions given in Table VI were converted to effective strain for the following analysis.

5.3 RESIDUAL TENSILE DUCTILITY

For all of the prestrain conditions listed in Table VI, tensile tests were run in either the longitudinal, L-direction (rolling direction, RD) or the transverse, T-direction (90° to RD) as indicated in the table. For each condition, the major prestrain (ε_{maj}) axis is in the L-direction, by convention. The following results pertain to the residual tensile ductility after various degrees of

pre-deformation along various strain paths. The measures of residual tensile ductility are the uniform elongation (UEL), total elongation (TEL) and post-uniform elongation (PUEL) measured during the tensile tests—all expressed in percent engineering strain. Note that PUEL is simply the difference between TEL and UEL (PUEL = TEL – UEL) and represents the amount of deformation sustained after the peak stress in the stress/strain (s/e) curve.

5.3.1 **Residual Tensile Ductility after UT Prestrain**

The sequential complex strain path of uniaxial tension (UT) prestrain followed by UT deformation in the same direction may seem redundant or unnecessary; however, this progression serves as a useful conceptual reference when considering other modes of deformation. Figure 62 shows the influence of UT prestrain ($\varepsilon_{maj} = \varepsilon_L$) on the residual ductility of the IF, HSLA and DP steels, in both the L-direction (left column) and the T-direction (right column). For the L-direction tests (Figure 62A, C and E), the residual ductility parameters vary as expected for all three materials, where UEL and TEL decrease proportionally with increasing prestrain, and the PUEL remains essentially unchanged. The PUEL would begin to decrease once the prestrain exceeded the UEL value of the as-produced material (0% prestrain condition in Figure 62).

For the T-direction tests, strikingly different behavior is observed. For the IF steel and the HSLA steel (Figure 62B and D), a gradual decrease in UEL and TEL occurs up to an effective prestrain of about 0.05 (note the difference in scale), while, beyond this prestrain level, the UEL decreases precipitously effectively to zero, and the PUEL "suddenly" increases to approximately the TEL value and then decreases with the TEL value with increasing prestrain. Thus, there are two types of stress/strain behavior observed for uniaxial tension prestrain followed by transverse tension, with a transition occurring at an effective prestrain level

somewhere between 0.06 and 0.07. Type 1 behavior (small prestrains) is the "normal" response where the TEL is more or less comprised of similar UEL and PUEL contributions (as for the case of the L-direction tests for the entire UT prestrain range). Type 2 behavior is characterized by grossly unbalanced contributions of uniform and post-uniform elongation to the total elongation, where the UEL is severely diminished, and PUEL is nearly equivalent to TEL. This behavior is a reflection of the cross-hardening effect described in Section 2.7.4. The implications of cross-hardening are discussed further in Section 6.1.

For the DP steel, Type 2 behavior is not observed for the T-direction tensile tests (Figure 62F) for any of the UT prestrain conditions. In fact, for all prestrain levels, the UEL, TEL and PUEL values for the T-direction tensile tests are equal to or slightly higher than the corresponding values for the L-direction tensile tests (Figure 62E). This unique response represents an advantage of DP steels over conventional steels in terms of residual ductility in this particular two step forming mode—uniaxial tension prestrain followed by transverse (orthogonal) uniaxial tension.

5.3.2 **Residual Tensile Ductility after PS Prestrain**

For the complex strain path of plane strain (PS) prestrain ($\varepsilon_{maj} = \varepsilon_L$) followed by subsequent uniaxial tension (UT) deformation, the residual ductility parameters are shown in Figure 63 for all materials as a function of effective prestrain for both L-direction and T-direction tensile tests. Considering first the IF steel (Figure 63A: L-direction tension tests, and Figure 63B: T-direction tension tests), a transition from Type 1 to Type 2 behavior (see Section 5.3.1) is observed in both directions (L and T) with that in the L-direction being more gradual. The HSLA steel shows similar behavior as the IF steel in the T-direction (Figure 63D), but appears to have no detrimental transition in the L-direction (Figure 63C), within the prestrain

interval examined. This may be, in part, a symptomatic reflection of the relative anisotropy of the IF steel in contrast to the HSLA steel.

By considering the influence of R-value on the strain path associated with uniaxial tension (see Figure 41), the effective difference between the plane strain prestrain path and the subsequent uniaxial tension (L-direction) strain path can be assessed. Assuming that the tensile R-value in the L-direction (R_0 in Table VIII) does not change significantly with plane strain prestrain, the angle (θ) between the uniaxial tension (UT) secondary strain path and the plane strain (PS) prestrain path (β=0) in surface strain space (Figure 41) is

$$\theta_{PS/UT} = \tan^{-1}(\beta_{UT}) = \tan^{-1}\left(-\frac{R_0}{R_0+1}\right). \quad [28]$$

For the IF steel, θ = 32°, and for the HSLA steel, θ = 22°. In perspective, the strain paths associated with plane strain ($\varepsilon_{maj} = \varepsilon_L$) and uniaxial tension ($\varepsilon_{maj} = \varepsilon_L$) differ by about 50% more (in terms of θ) for the IF steel than for the HSLA steel. Recall that Ronde-Oustau and Baudelet (60) explained that, when the strain path is changed, formability (or in this case residual ductility) decreases more in the secondary strain path if the secondary strain path is further from the primary path on the tension side of the surface strain diagram (Figure 41). For the T-direction tensile tests, the prestrain path and the secondary deformation strain path are extremely different (more than 90° apart in surface strain space) such that the residual ductility is reduced for both the IF steel and the HSLA steel in this complex strain path.

For the DP steel, the residual tensile ductility after plane strain (PS) prestrain is shown in Figure 63E and Figure 63F for the L-direction and T-direction tension tests, respectively. For reference, θ (Equation 28) for the DP steel is about 26° (R_0 = 0.97)—an intermediate value between that of the IF steel and that of the HSLA steel. In the L-direction tests, the DP steel

shows behavior similar to that of the HSLA steel. In the T-direction tensile tests, however, the DP steel exhibits much greater retention of residual ductility within the tested prestrain range. For example, at the largest PS prestrain level attained ($\varepsilon_{eff} \sim 0.09$), the DP steel retained more than 3% tensile uniform elongation (UEL) in the T-direction, while the residual UEL of the IF steel and the HSLA steel are less than 1%. Additionally, the residual total elongation (TEL) of the DP steel is higher than that of the HSLA steel and approaches that of the highly formable IF steel. Again, the DP steel shows a distinct advantage over conventional steels in terms of residual ductility in this particular two step forming mode—plane strain prestrain followed by transverse (orthogonal) uniaxial tension.

5.3.3 **Residual Tensile Ductility after BB Prestrain**

For the complex strain path of balanced biaxial (BB) stretching ($\varepsilon_{maj} = \varepsilon_{min}$) followed by subsequent uniaxial tension (UT) deformation, the residual ductility parameters are shown in Figure 64 for all materials as a function of effective prestrain for both L-direction and T-direction tensile tests. For the IF steel (Figure 64A and B) and the HSLA steel (Figure 64C and D), similar behavior is observed for both directions, L and T, where a transition from Type 1 behavior to Type 2 behavior occurs at an effective prestrain level between 0.05 and 0.10. This type of "symmetric" response is expected from the in-plane symmetry of balanced biaxial stretching deformation. The DP steel also shows a symmetric response in the L-direction and T-direction tensile tests; however, the response is different than that of the IF steel and HSLA steel, where the deterioration in residual ductility at higher BB prestrain levels is less severe. In fact, at the same effective prestrain level (*e.g.*, $\varepsilon_{eff} = 0.1$), the measured residual ductility is similar to that observed for uniaxial tension (UT) prestrain (Figure 62E and F).

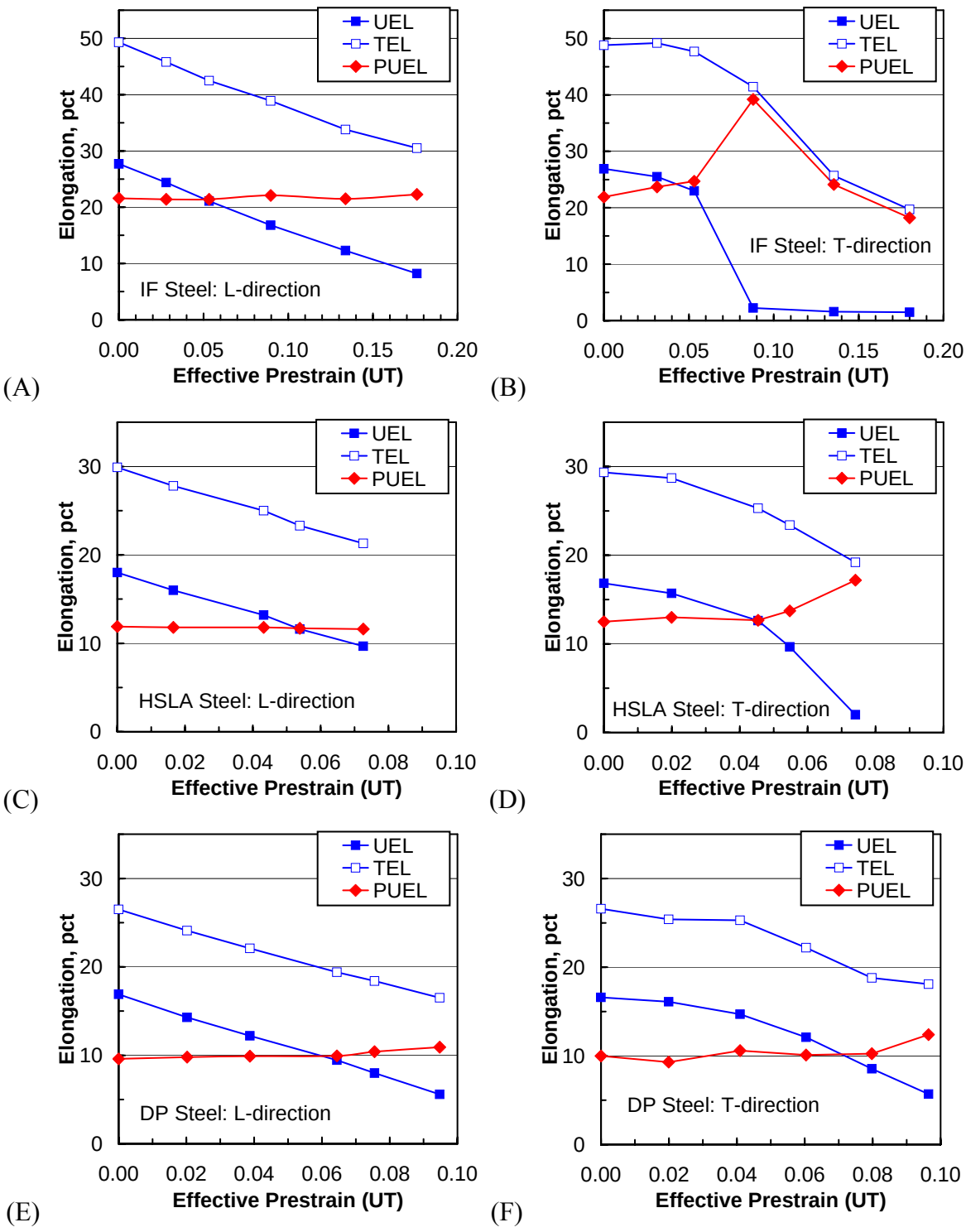

Figure 62: Residual tensile ductility after uniaxial tension (UT) prestrain ($\varepsilon_{maj} = \varepsilon_L$)—(A and B) IF steel, (C and D) HSLA steel, and (E and F) DP steel. Left column: tensile test in L (rolling) direction; Right column: tensile test in T direction (90° to rolling direction).

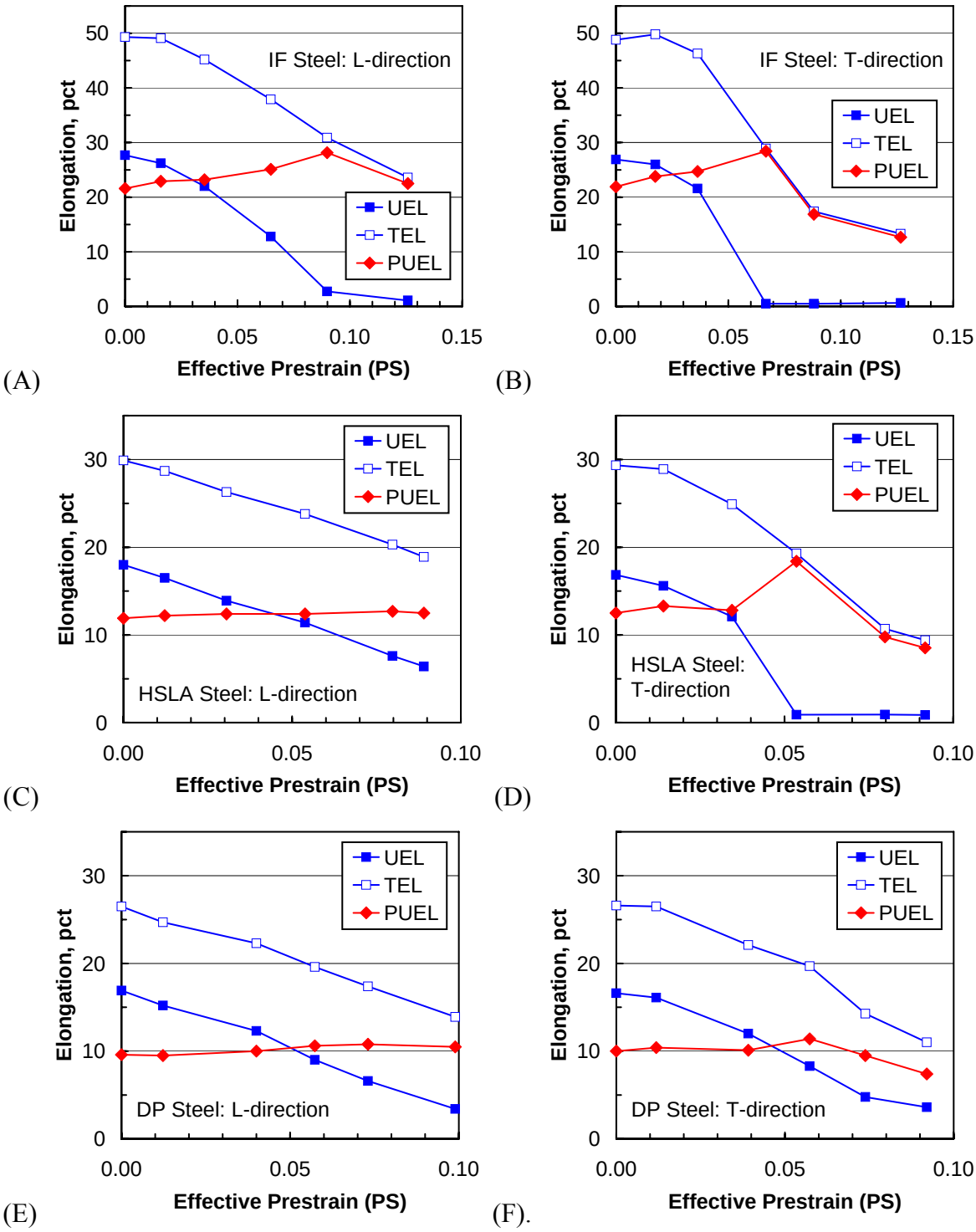

Figure 63: Residual tensile ductility after plane strain (PS) prestrain ($\varepsilon_{maj} = \varepsilon_L$)—(A and B) IF steel, (C and D) HSLA steel, and (E and F) DP steel. Left column: tensile test in L (rolling) direction; Right column: tensile test in T direction (90° to rolling direction).

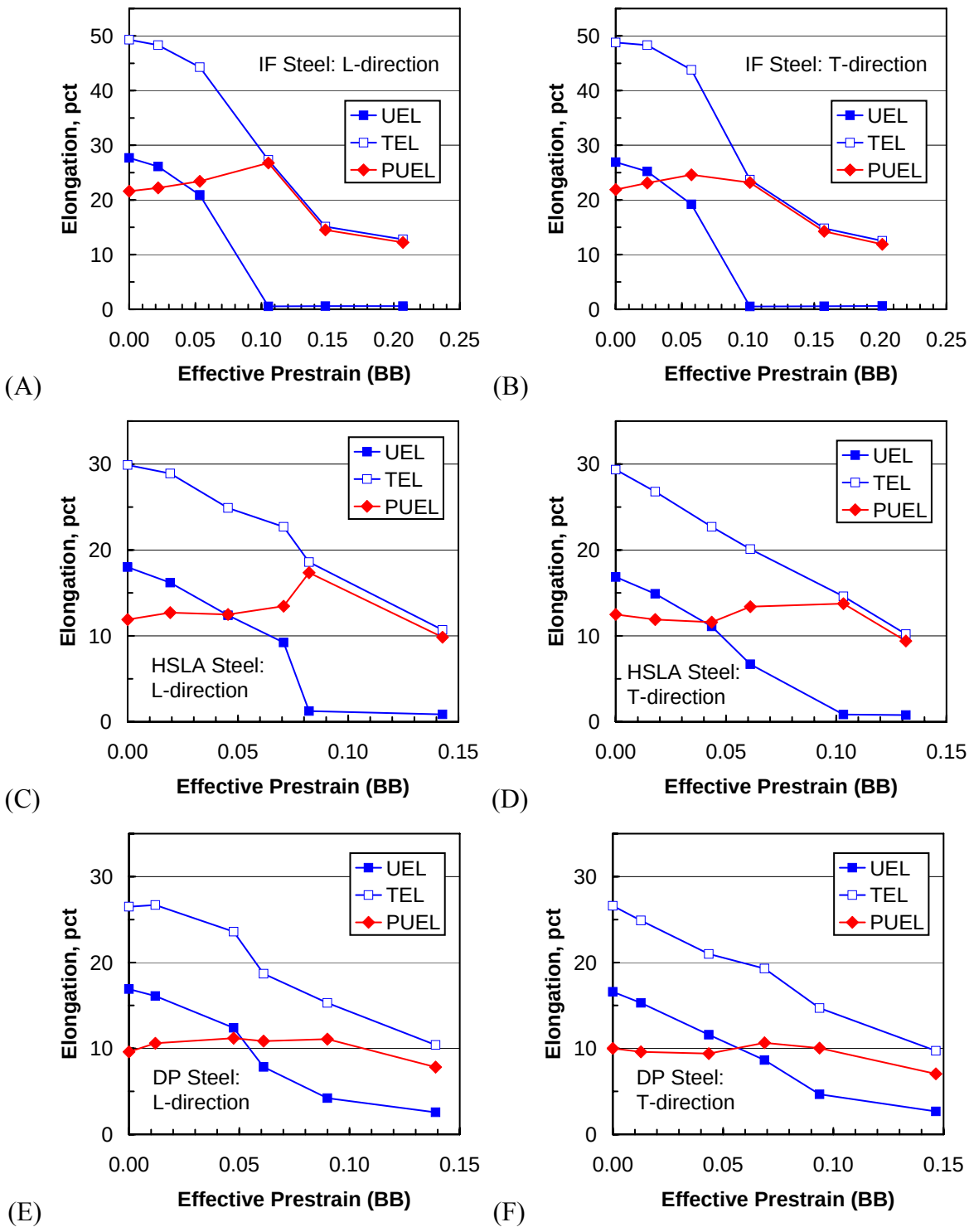

Figure 64: Residual tensile ductility after balanced biaxial stretching (BB) prestrain—(A and B) IF steel, (C and D) HSLA steel, and (E and F) DP steel. Left column: tensile test in L (rolling) direction; Right column: tensile test in T direction (90° to rolling direction).

5.4 STRENGTH EVOLUTION

In addition to the residual ductility parameters discussed above, the subsequent tensile flow stress (yield strength) was measured for each of the prestrain conditions listed in Table VI, in either the longitudinal, L-direction (rolling direction, RD) or the transverse, T-direction (90° to RD) as indicated in the table. Recall that, for each condition, the major prestrain (ε_{maj}) axis is in the L-direction, by convention. The following results pertain to the strength evolution after various degrees of pre-deformation along various strain paths. The measures of yield strength used in this analysis are the conventional 0.2% offset tensile flow stress ($\sigma_{0.2\%OFS}$) and the flow stress at 1% tensile strain ($\sigma_{1\%FS}$), as suggested by Toyoda *et al*. (63) in their analyses of the differential hardening behavior of conventional steels (see Figure 47A, where $\sigma_1 = \sigma_{1\%FS}$). For the following analysis, recall that "cross-hardening" means that the post-forming tensile yield strength is larger along the minor prestrain axis (T-direction) than along the major prestrain axis (L-direction); "cross-softening" means that the post-forming tensile yield strength is higher along the major prestrain axis than along the minor prestrain axis. "Isotropic hardening" refers to the condition where the post-forming tensile yield strength is the same along the minor and minor prestrain axes.

5.4.1 **Tensile Yield Strength after UT Prestrain**

The tensile flow stress, measured by $\sigma_{0.2\%OFS}$ and by $\sigma_{1\%FS}$, as a function of uniaxial tension (UT) prestrain ($\varepsilon_{maj} = \varepsilon_L$), is shown for both the L-direction and the T-direction tensile tests in Figure 65A ($\sigma_{0.2\%OFS}$) and in Figure 65B ($\sigma_{1\%FS}$). The IF steel, HSLA steel and DP steel data are shown together, as the intrinsic strength differences between materials allows such simultaneous uncluttered representation (for all prestrain modes). Note that, to avoid confusion, it was

necessary to plot the residual tensile ductility data (Section 5.3) on separate axes for each material in each tensile test direction.

(A)

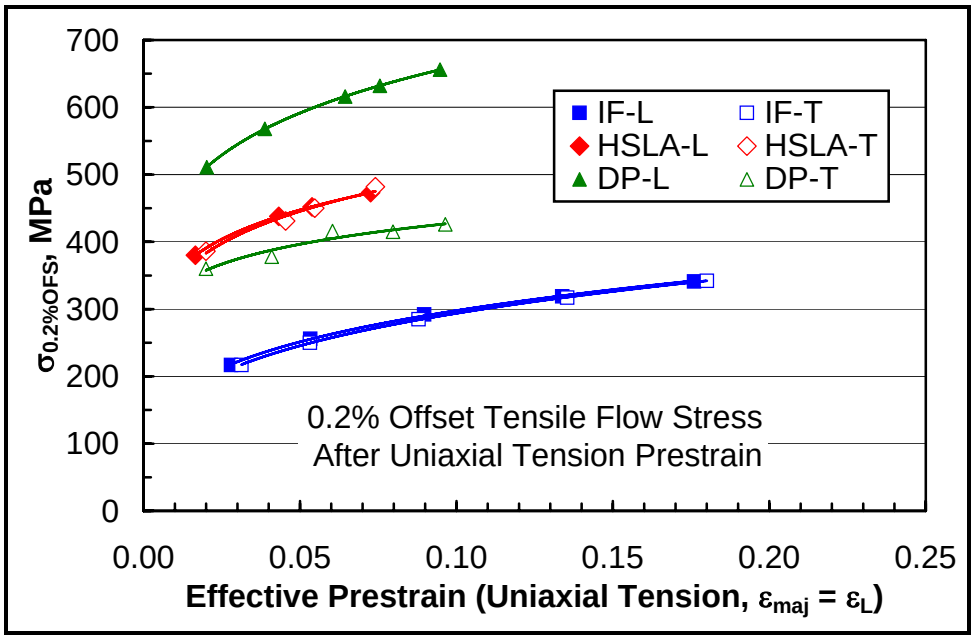

(B)

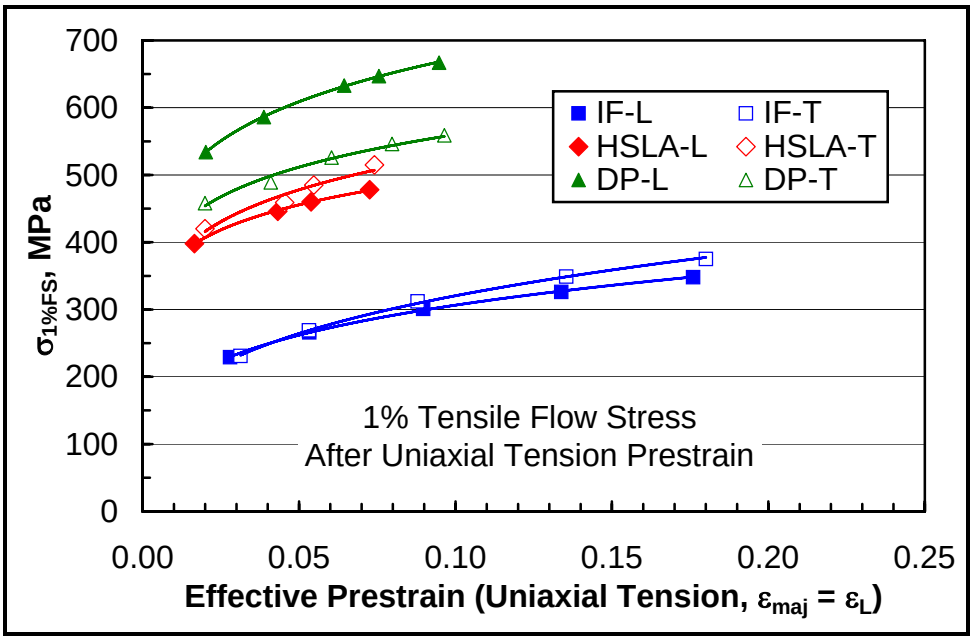

Figure 65: Tensile flow stress (yield strength) as a function of uniaxial tension (UT) prestrain for the IF steel, the HSLA steel and the DP steel—(A) based on the 0.2% offset flow stress ($\sigma_{0.2\%OFS}$), and (B) based on the flow stress at 1% tensile strain ($\sigma_{1\%FS}$).

In Figure 65A, it appears that both the IF steel and the HSLA steel exhibit isotropic tensile yield strength evolution or isotropic hardening (that is, for each UT prestrain level, the subsequent L and T direction tensile yield strengths are the same in terms of $\sigma_{0.2\%OFS}$). The DP steel shows a unique response, where the T-direction yield strength ($\sigma_{0.2\%OFS}$) is significantly *lower* than that measured in the L-direction. For the case where the subsequent yield strength in tension is lower in the T-direction than in the L-direction after prestraining (*e.g.*, DP steel prestrained in the UT deformation mode), the response will be called "cross-softening", to distinguish from the "cross-hardening" effect discussed in Section 2.7.4. The cross-softening effect increases for the DP steel as the amount of UT prestrain increases and is nearly 250 MPa at an effective prestrain of 0.1. These results agree with the data reported by Sugimoto *et al*. (65) and reproduced in Figure 48.

In Figure 65B, where $\sigma_{1\%FS}$ is the measure of yield strength, a different conclusion is drawn when assessing the anisotropy of tensile yield strength evolution for the IF and HSLA steels. It is now clear that these conventional "single phase" materials indeed exhibit cross-hardening ($\sigma_{1\%FS,T} > \sigma_{1\%FS,L}$) caused by UT prestrain, as shown for plane strain (PS) prestrain by Yan *et al*. (62) in Figure 46 and by Toyoda *et al*. (63) in Figure 47. The extent of differential hardening increases with increasing UT prestrain for the IF steel and the HSLA steel. The unique behavior of the DP steel persists with the alternate measure of yield strength, $\sigma_{1\%FS}$; however, the cross-softening is much less than that suggested by the conventional measure of tensile yield strength, $\sigma_{0.2\%OFS}$.

5.4.2 **Tensile Yield Strength after PS Prestrain**

For plane strain (PS) prestrain, the IF steel, HSLA steel and DP steel show tensile yield strength evolution that is respectively similar to that shown for the UT prestrain mode, with a few minor differences. These results are shown in Figure 66A for $\sigma_{0.2\%OFS}$ and in Figure 66B for $\sigma_{1\%FS}$. The first difference between the UT and PS prestrain modes is that cross-hardening is revealed in terms of $\sigma_{0.2\%OFS}$ for the IF steel and HSLA steel. Secondly, the cross-hardening response is greater for PS prestrain than for UT prestrain at any given ε_{eff} value. The cross-softening behavior of the DP steel persists in the PS prestrain mode, but the extent of which is far less than that observed for the UT prestrain mode.

5.4.3 **Tensile Yield Strength after BB Prestrain**

Tensile yield strength evolution for the balanced biaxial (BB) prestrain mode is shown for the IF, HSLA and DP steels in (Figure 67). The IF steel and DP steel show isotropic hardening in terms of both $\sigma_{0.2\%OFS}$ and $\sigma_{1\%FS}$ (that is, the yield strength, measured by either index, is the same in the L-direction and T-direction). This occurrence is an extension of the argument presented in Section 5.3.3 in the context of residual ductility, where the symmetry of the prestrain path leads to a symmetric response in subsequent uniaxial tension. For the HSLA steel, however, the T-direction yield strength is consistently higher than that in the L-direction. Additionally, the difference neither increases nor decreases as prestrain increases. It appears that the intrinsic anisotropy of mechanical properties is propagated through the prestrain deformation. In the as-produced condition (see Table VII), the HSLA steel shows the greatest difference in yield strength ($YS_T - YS_L$ = 37 MPa) and in ultimate tensile strength ($UTS_T - UTS_L$ = 16 MPa) among the three steels. The important observation for the HSLA steel is that the L-direction

yield strength and the T-direction yield strength evolve similarly (although offset by intrinsic anisotropy) when the prestrain mode is balanced biaxial stretching (BB).

(A)

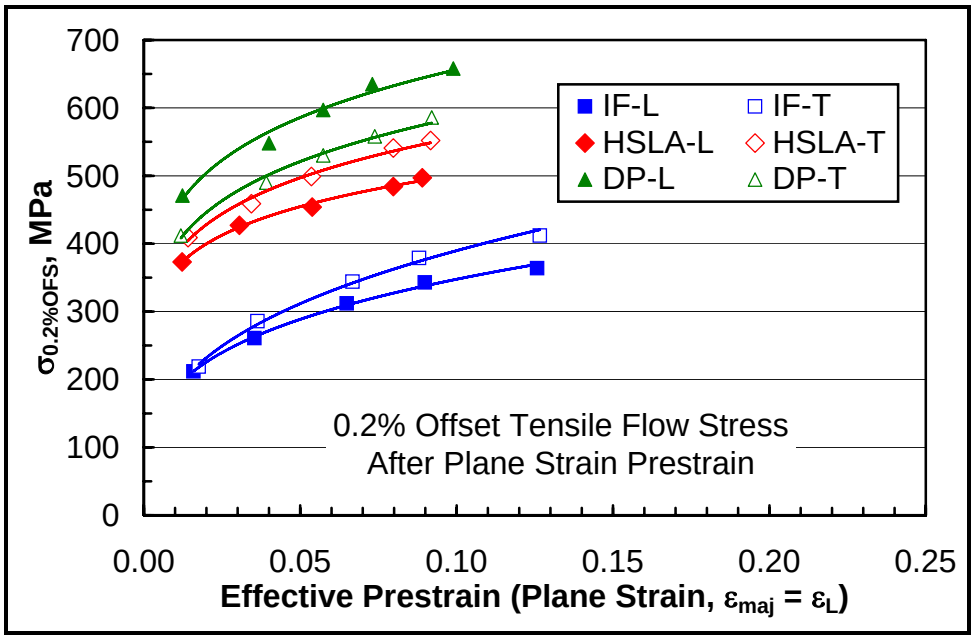

(B)

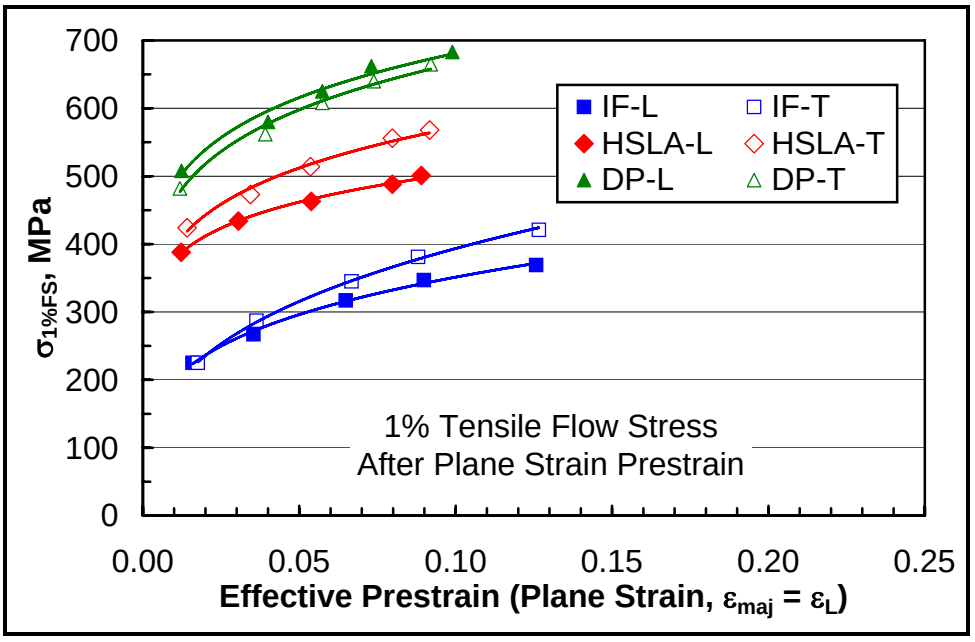

Figure 66: Tensile flow stress (yield strength) as a function of plane strain (PS) prestrain for the IF steel, the HSLA steel and the DP steel—(A) based on the 0.2% offset flow stress ($\sigma_{0.2\%OFS}$), and (B) based on the flow stress at 1% tensile strain ($\sigma_{1\%FS}$).

(A)

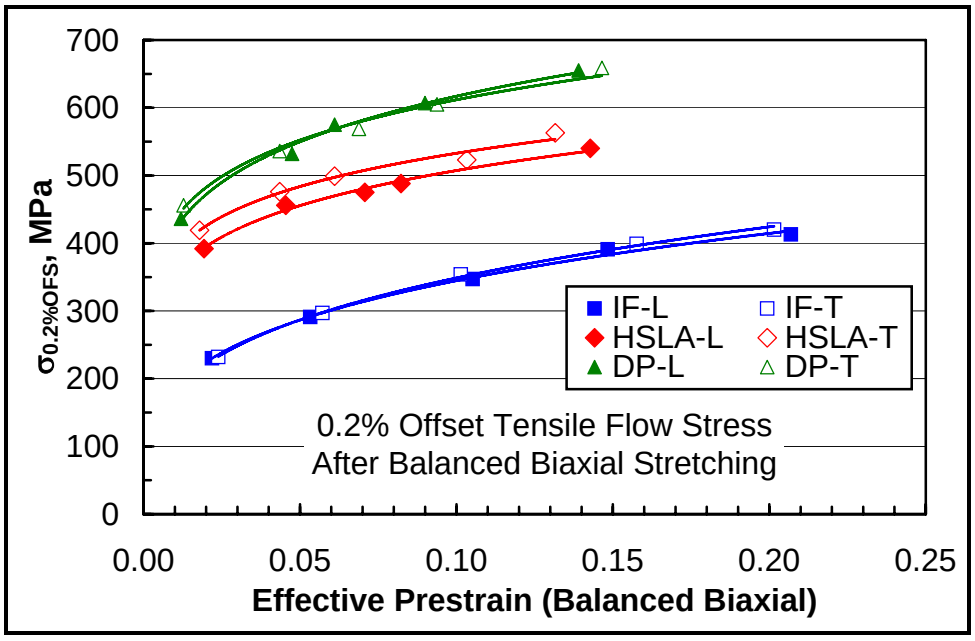

(B)

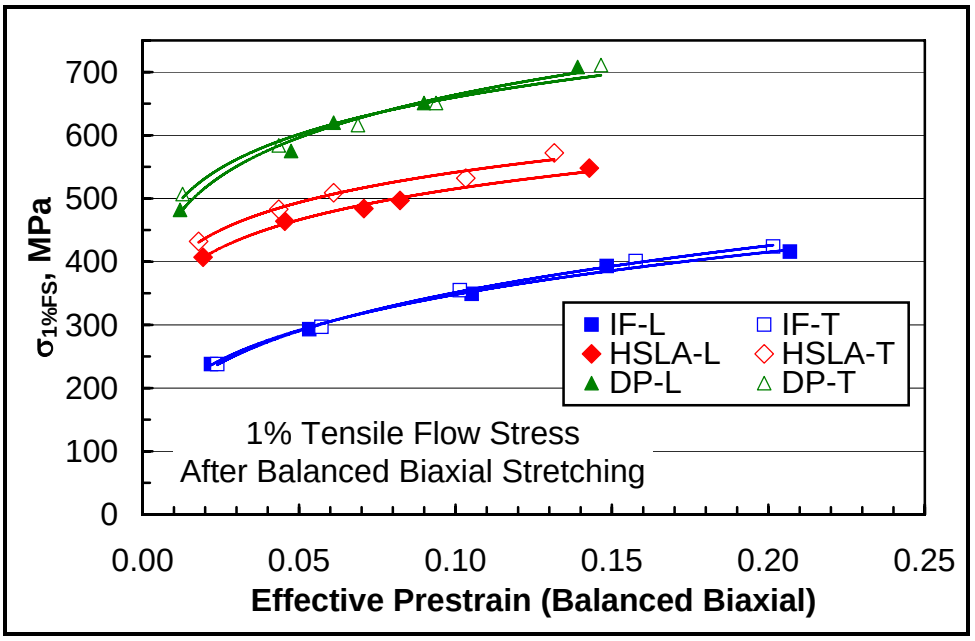

Figure 67: Tensile flow stress (yield strength) as a function of balanced biaxial stretching (BB) prestrain for the IF steel, the HSLA steel and the DP steel—(A) based on the 0.2% offset flow stress ($\sigma_{0.2\%OFS}$), and (B) based on the flow stress at 1% tensile strain ($\sigma_{1\%FS}$).

5.4.4 **Differential Hardening Behavior**

For the L-direction tensile tests and the T-direction tensile tests after prestraining, separate series of prestrained panels were created. As the tensile specimens were extracted from the center portion of each panel, it was not possible to obtain L-direction and T-direction tensile specimens from a single test panel. As such, for each nominal prestrain condition, the L-direction tests and the T-direction tests were associated with slightly different prestrain conditions, as shown in the compilation of prestrained specimens in Table VI (note the separate columns for subsequent tension in the L-direction and subsequent tension in the T-direction). With the inherent variability of the experimental prestraining method, it is not directly possible to compare the L and T tensile response for each specified prestrain condition. For this reason, the regression equations of the curve fits ($Y = AX^B$, where A and B are coefficients) of the data shown in Figure 65 through Figure 67 were used to calculate the differential hardening response (*i.e.*, $\Delta YS = YS_T - YS_L$) as a function of prestrain, for each prestrain mode. The calculated differential hardening behavior for the three materials is summarized in Figure 68 (uniaxial tension prestrain, UT), Figure 69 (plane strain prestrain, PS), and Figure 70 (balanced biaxial stretching prestrain, BB), for both measures of tensile yield strength, $\sigma_{0.2\%OFS}$ and $\sigma_{1\%FS}$, up to an effective strain of 0.1.

Figure 68 shows the intense "cross-softening" behavior of the DP steel and the mild "cross-hardening" behavior of the IF and HSLA steels, for UT prestrain. Considering the DP steel behavior in Figure 68 (UT prestrain), for example, it appears that the mechanism responsible for the cross-softening behavior affects the initial yield behavior (at 0.2% offset) more than the gross plastic deformation behavior shortly after yielding (at 1% strain). Conversely, the cross-hardening mechanism in the IF steel and the HSLA steel affects the post-yielding behavior (at

1% strain) more than the initial yielding behavior (0.2% offset). This basic difference implies different responsible mechanisms for cross-hardening and cross-softening. The impact on the initial yielding behavior implies that the cross-softening effect in the DP steel is influenced by an existing, static (elastic) phenomenon such as residual stresses induced by prestraining. The post-yielding influence of the cross-hardening mechanism in the IF and HSLA steels implies a dynamic phenomenon that is manifested by dislocation interactions during plastic deformation.

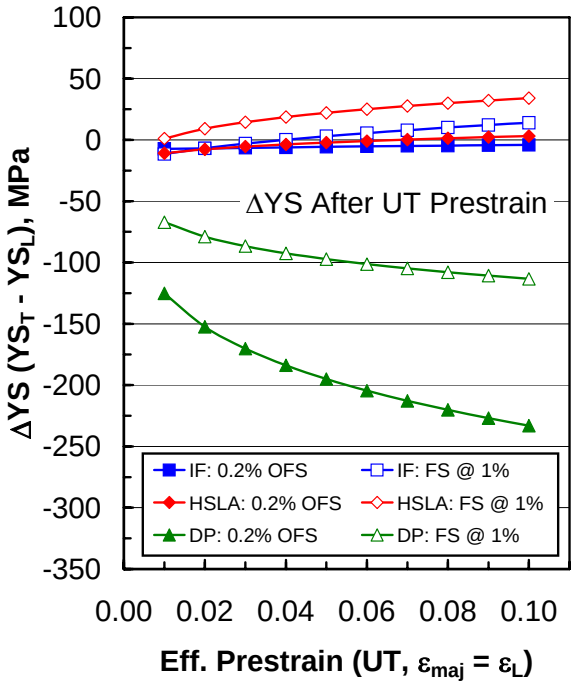

Figure 68: Differential hardening for the uniaxial tension (UT) prestrain mode. See text for details.

It is certainly possible that both mechanisms are operating in all three materials, but at different intensities. It may be that the cross-softening mechanism in the DP steel serves to alleviate or mask the underlying cross-hardening mechanism displayed by the IF steel and the HSLA steel. It is also likely that the cross-softening response diminishes as secondary tensile deformation continues—assuming an elastic distribution of prestrain-induced residual stresses

being the responsible mechanism. This notion is similar to the behavior commonly observed in Bauschinger Effect tests for DP steels. For example, Figure 31 (16) shows that the initial yielding behavior upon strain reversal (compression) occurs at a very low stress value (σ_r), but the "reverse curve" approaches the "forward curve" as compressive deformation progresses.

Figure 69 summarizes the differential hardening behavior for plane strain (PS) prestrain. For this prestrain mode, the cross-hardening effect of the IF steel and the HSLA steel is more pronounced than for the UT prestrain mode—apparent for both the $\Delta\sigma_{0.2\%OFS}$ and the $\Delta\sigma_{1\%FS}$ measures of differential hardening. Additionally, the cross-softening response of the DP steel is less prominent, yet still dominates the initial yielding and post yielding behavior. For the UT prestrain mode discussed above, the cross-softening effect increases monotonically at an ever-decreasing rate; however, it appears that the magnitude of the cross-softening effect saturates at a low level of PS prestrain. It could also be that that the underlying (masked) cross-hardening mechanism in the DP steel increases with increasing PS prestrain and serves to lessen the effect of the cross-softening mechanism.

For the BB prestrain mode (Figure 70), only a minor differential hardening effect is observed for the IF steel, the HSLA steel and the DP steel. Again, the consistent, steady cross-hardening effect of the HSLA steel is conceivably related to the intrinsic anisotropy of the material. It should be mentioned, in the context of balanced biaxial stretching (BB) prestrain, that a minimal differential hardening response does not necessarily mean that the *mechanisms* associated with cross-softening and cross-hardening are inoperative for this prestrain mode. It means rather that the effects of these mechanisms are acting similarly to affect the L-direction and the T-direction tensile response, owing to the symmetry of the prestrain deformation mode.

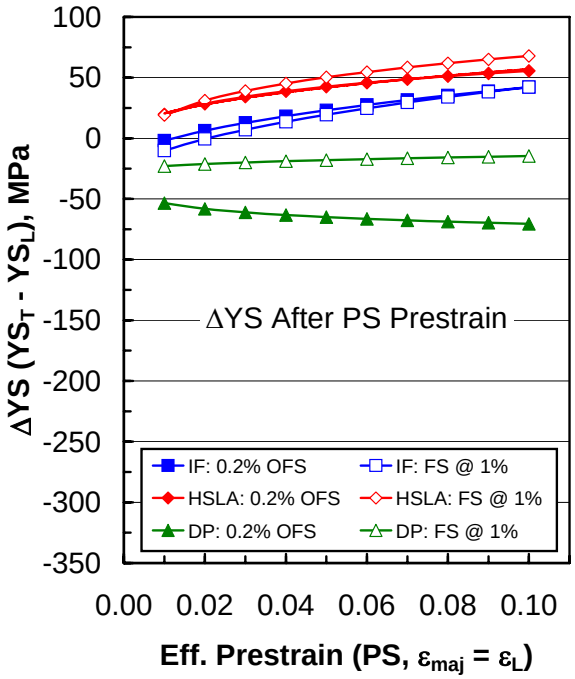

Figure 69: Differential hardening for the plane strain (PS) prestrain mode. See text for details.

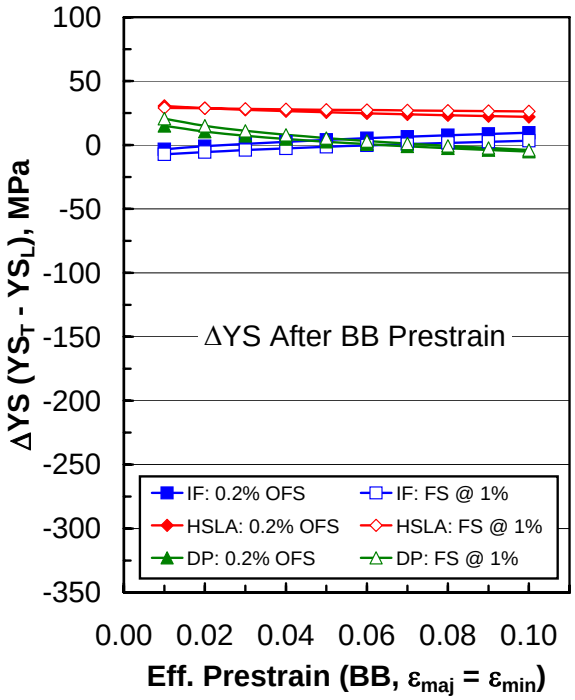

Figure 70: Differential hardening for the balanced biaxial stretching (BB) prestrain mode. See text for details.

5.4.5 **Effective Strain Analysis**

As discussed in Section 5.2, effective stress and strain were developed, in part, so that uniaxial tension stress/strain relationships can be extrapolated to more general modes of deformation, and it follows that post-forming tensile test behavior (*e.g.*, strength) may be predicted for any prestrain mode, as long as the primary strain history is defined by an effective strain function and the reference uniaxial tension behavior of the as-produced material (before prestraining) is known. The Tresca yield criterion, and its corresponding effective stress and effective strain relationships (Equations 25 and 27) are by no means the most advanced or accurate descriptors of material behavior. There are many other available material models that address such material characteristics as normal and planar anisotropy, the Bauschinger Effect, and differential hardening in general—all of which are assumed negligible in the Tresca material model. A number of these classic and recently developed material models have been reviewed by Stoughton (85) and by Banabic *et al*. (86). For the following exercise, the purpose is not to illustrate or define the most appropriate material model for each material (beyond the scope of this work), but rather: 1) to emphasize the need to address such factors as differential hardening and plastic anisotropy, and 2) to illustrate the basic behavioral differences of the DP steel in contrast to more conventional materials such as the IF steel and the HSLA steel.

In Figure 71 through Figure 73, the tensile yield strength evolution data ($\sigma_{0.2\%OFS}$) discussed in Section 5.4 are shown for all three experimental prestrain paths (UT, PS and BB prestrain) combined on single plots (*i.e.*, one plot for each material). In this way, the effects of strain path on strength evolution and differential hardening (cross-hardening and cross-softening) can be seen more clearly for each material. For illustrative purposes, the complex strain path sequence of uniaxial tension ($\varepsilon_{maj} = \varepsilon_L$) followed by additional tension in the L-direction is

shown as the reference curve (symbols connected by a fitted curve). The strength evolution data for the other complex strain paths are shown as symbols only (no connecting fitted curve). For added clarity of presentation, the L-direction tensile yield strength data are shown as filled symbols, while those for the T-direction are displayed as open (unfilled) symbols. The Tresca effective strain function (Equation 27)—hereafter, "effective strain function"—predicts that all of the tensile yield strength data (for both L-direction and T-direction tensile tests) will lie along the reference curve, for all prestrain modes.

For the IF steel and the HSLA steel (Figure 71 and Figure 72, respectively), the effective strain function sufficiently predicts the tensile yield strength in both the L and T directions after uniaxial tension (UT), as the L-direction data define the reference curve, and these materials show nearly-isotropic hardening for this prestrain mode (Figure 65). For the IF steel, the tensile yield strength evolution is greatly under-predicted by the effective strain function for plane strain (PS) and balanced biaxial stretching (BB) prestrain modes, with the worst prediction pertaining to the sequence of PS prestrain ($\varepsilon_{maj} = \varepsilon_L$) followed by uniaxial tension in the T-direction. Recall that the cross-hardening effect is greatest for this complex strain path sequence. For the HSLA steel, the effective strain function gives a reasonable prediction of the subsequent L-direction tensile yield strength for both PS and BB prestrain modes (only slightly under-predicted by the effective strain function). For the T-direction tensile tests, however, the tensile yield strength is again significantly under-predicted. It is likely that these minor differences between the IF steel and HSLA steel are dictated by statistically preferred crystal orientation (both the annealing textures and deformation textures, see Section 2.7.1) and by other microstructural differences such as grain size and precipitate/carbide dispersions.

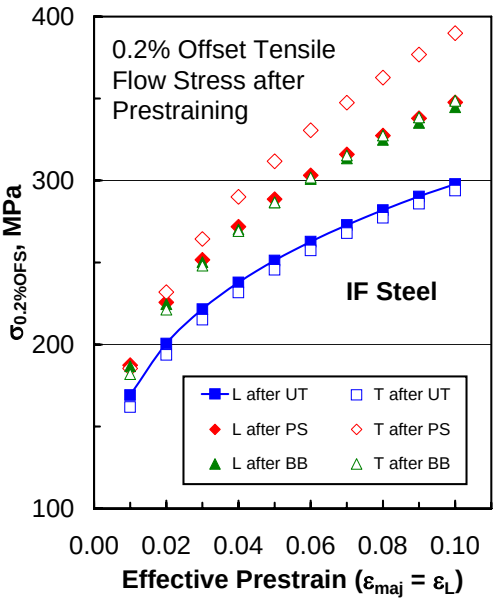

Figure 71: Tensile yield strength evolution of the IF steel along various prestrain paths ($\varepsilon_{maj} = \varepsilon_L$)—UT = uniaxial tension; PS = plane strain; and BB = balanced biaxial tension. The filled symbols represent tensile tests in the L direction (parallel to major prestrain axis), while the open symbols represent tensile tests in the T-direction (parallel to minor prestrain axis).

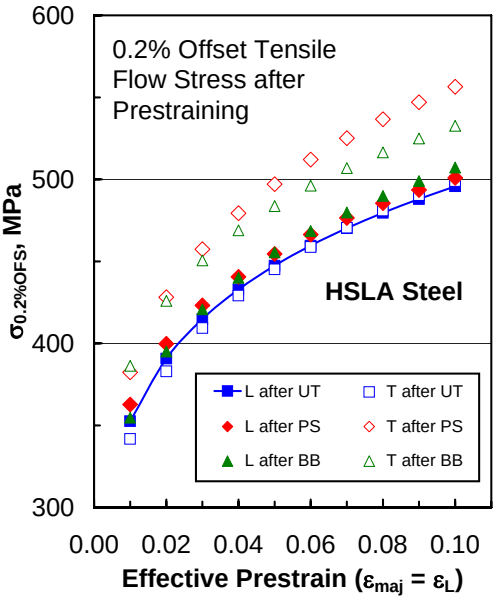

Figure 72: Tensile yield strength evolution of the HSLA steel along various prestrain paths ($\varepsilon_{maj} = \varepsilon_L$)—UT = uniaxial tension; PS = plane strain; and BB = balanced biaxial tension. The filled symbols represent tensile tests in the L direction (parallel to major prestrain axis), while the open symbols represent tensile tests in the T-direction (parallel to minor prestrain axis).

The DP steel (Figure 73) presents an entirely unique effective strain relationship for the various prestrain paths, in terms of strength evolution. First, the effective strain function tends to *over*-predict the subsequent tensile yield strength for all prestrain modes, except of course, the reference strain path of UT prestrain ($\varepsilon_{maj} = \varepsilon_L$) followed by tension in the L-direction (*i.e.*, the defined reference curve). Secondly, for UT prestrain ($\varepsilon_{maj} = \varepsilon_L$) followed by tension in the T-direction, the worst prediction is made, where, for the IF steel and HSLA steel, the best prediction corresponds to this sequence. Interestingly, for the T-direction tensile tests, the effective strain prediction improves as the prestrain path deviates further from uniaxial tension (untrue for the IF steel and HSLA steel). As the strength evolution is over-predicted for the balanced biaxial stretching (BB) prestrain mode, it is further apparent that the mechanism(s) responsible for the cross-softening effect (UT and PS prestrain) indeed affect the tensile response after BB prestrain, albeit symmetrically, as mentioned at the end of Section 5.4.4.

5.5 NEUTRON DIFFRACTION AND RESIDUAL STRESS ANALYSIS

5.5.1 **Neutron Diffraction Results**

Recall (Section 4.4.2) that twelve samples were sent to NIST for neutron diffraction analysis. One sample of each of the three steels was examined in the following conditions:

- As-produced (no prestrain)
- Prestrained to 5% major strain in uniaxial tension
- Prestrained to 5% major strain in plane strain
- Prestrained to 5% major strain in balanced biaxial stretching

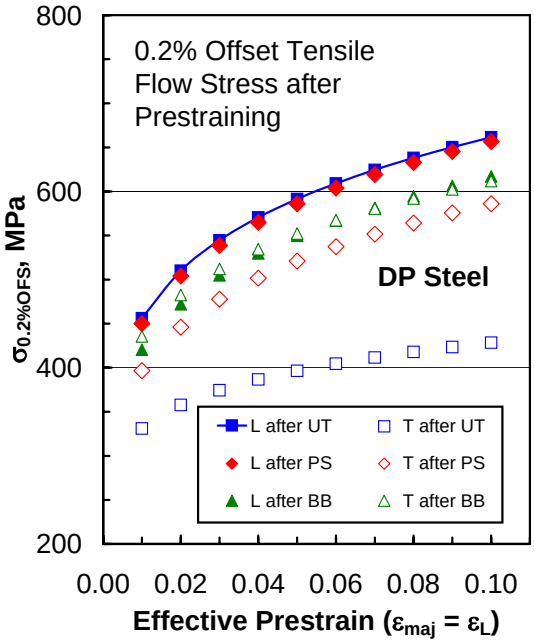

Figure 73: Tensile yield strength evolution of the DP steel along various prestrain paths ($\varepsilon_{maj} = \varepsilon_L$)—UT = uniaxial tension; PS = plane strain; and BB = balanced biaxial tension. The filled symbols represent tensile tests in the L direction (parallel to major prestrain axis), while the open symbols represent tensile tests in the T-direction (parallel to minor prestrain axis).

The ferrite interplanar spacings (d-spacings) were reported (for both {200} and {211} reflections) in the three principal directions (1, 2 and 3) for each sample with the following convention:

- 1 – the longitudinal (L) direction or sheet rolling direction (RD), also corresponding to the major strain direction for each prestrain condition
- 2 – the transverse (T) direction (90° to the RD)
- 3 – the sheet normal or thickness direction

All seventy-two ferrite d-spacing measurements are shown in Figure 74. For the {200} d-spacings (left column of Figure 74), relatively minor disturbances (dilation and contraction) in the reflecting plane spacings are observed for the IF steel and the HSLA steel when comparing the various prestrained samples to the reference ("Ref") samples in each principal direction.

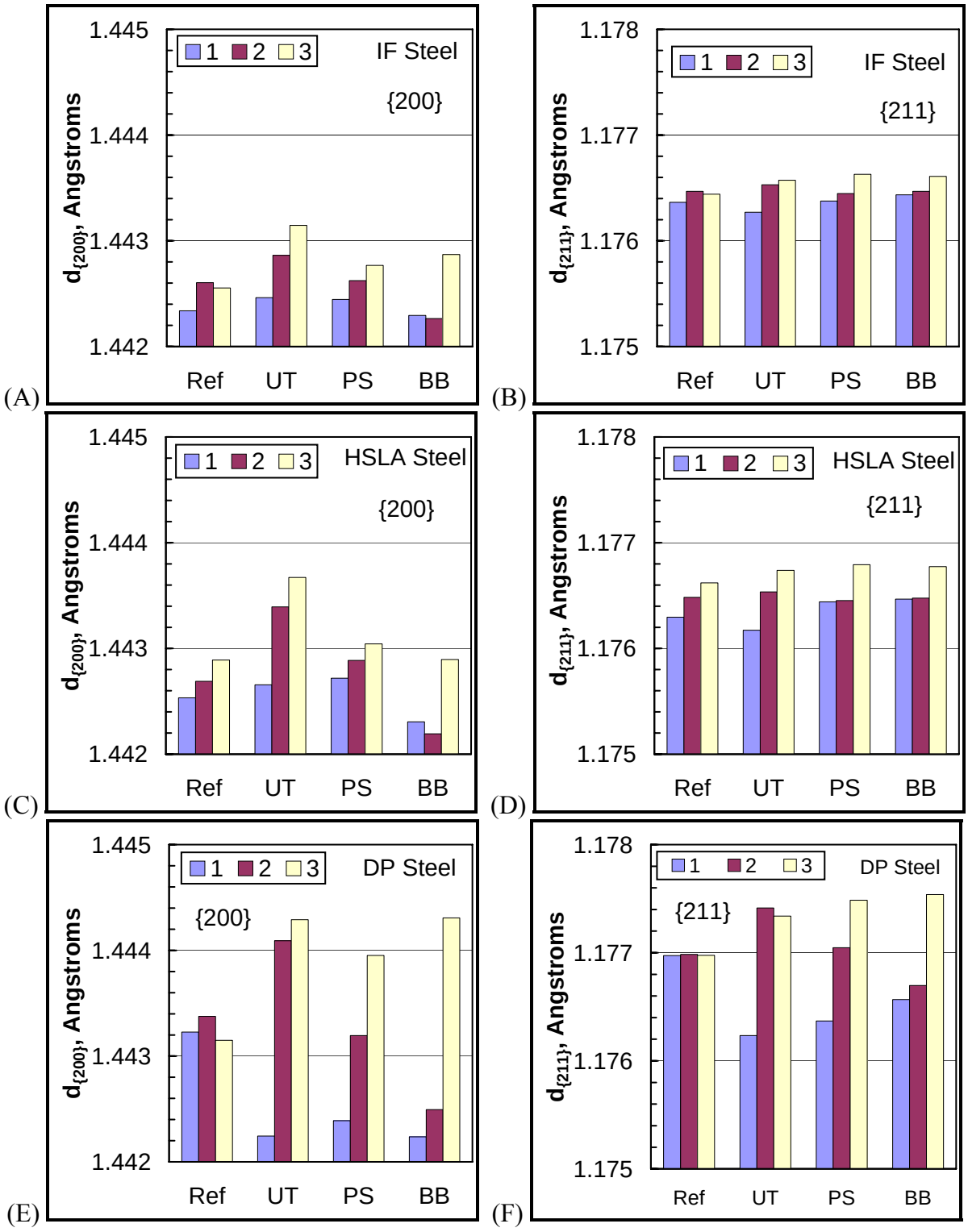

Figure 74: Interplanar spacings ({200} and {211}) for various prestrain conditions ($\varepsilon_{maj} = \varepsilon_L = 0.05$) measured by neutron diffraction—(A, B) IF steel, (C, D) HSLA steel and (E, F) DP steel. The designations 1, 2 and 3 refer to the principal directions and correspond to the longitudinal (L), transverse (T) and thickness dimensions of the samples.

For the DP steel, the d-spacing changes are more systematic and generally of larger magnitude. For the major strain direction (principal direction 1), consistent contraction of the {200} d-spacings (compressive strain) is shown for all prestrain modes, while, in the thickness direction (principal direction 3), consistent expansion of the {200} d-spacings (tensile strain) is shown for all prestrain modes. For the minor strain direction (principal direction 2), the sign of the {200} d-spacing change depends on the prestrain path and ranges from significant expansion for the UT prestrain mode to significant contraction for the BB prestrain mode, where only a minor contraction is shown for the PS prestrain mode. For the {211} d-spacings, (right column in Figure 74), similar trends in d-spacing changes are apparent for each material.

5.5.2 **Residual Stress Calculations based on Neutron Diffraction Data**

The d-spacing measurements were converted to elastic strains with Equation 21, and the deformation-induced residual stress components in each principal direction (1, 2 and 3) were calculated with Equations 22a through 22c with the diffraction elastic constants supplied by NIST (80) (see Section 4.4.3 for more background). The calculated deformation-induced residual stress components ($\sigma_{dr,ij}$) are summarized in Table IX for the {200} reflection data and in Table X for the {211} reflection data. As the principal axes are assumed from sample symmetry, all shear stress components of $\sigma_{dr,ij}$ are assumed zero, and as such, only the principal components of $\sigma_{dr,ij}$ (*i.e.*, $\sigma_{dr,1}$, $\sigma_{dr,2}$ and $\sigma_{dr,3}$) are shown in the summary tables. In reviewing Table IX and Table X (columns under the heading "$\sigma_{dr,ij}$"), it appears that the deformation-induced residual stress components are highly variable. Recall, however, that the magnitude (and in some cases the sign) of the residual stress depends almost entirely upon the choice of the reference d_0-value (Equation 19), and that the d-spacings of the "as-produced" samples (non-

prestrained) were used for lack of specific information pertaining to the true "unstressed" d_0-value. Also, the residual stress calculations depend, to a lesser extent perhaps, upon the choice of diffraction elastic constants. With these uncertainties in mind, and considering the end-use of the information generated by the neutron diffraction analysis, it is more appropriate to consider the deviatoric components of $\sigma_{dr,ij}$, as the hydrostatic or mean stress value for each deformation-induced residual stress state is not needed for this particular analysis. The hydrostatic stress components for each deformation-induced residual stress state that was calculated for each of the prestrained samples is listed under the heading "$\sigma_{dr,m}$" where

$$\sigma_{dr,m} = \frac{\sigma_{dr,kk}}{3} = \frac{\sigma_{dr,1} + \sigma_{dr,2} + \sigma_{dr,3}}{3}, \text{ and} \quad [28]$$

$$\sigma'_{dr,ij} = \sigma_{dr,ij} - \sigma_{dr,m}\delta_{dr,ij} \quad [29]$$

where $\sigma'_{dr,ij}$ refers to the deviatoric stress tensor of the deformation-induced residual stress state, shown under the corresponding heading in Table IX and Table X. Again, as the shear stress components are assumed zero, only the principal stress components are shown in the summary tables.

With this transformation, a meaningful pattern develops in the deviatoric components of the deformation-induced residual stresses. It also is clear that, for the different reflections ({200} and {211}), the calculated residual stress states in each sample differ effectively by only a hydrostatic stress component. As such, it is reasoned that, for each deviatoric component of deformation-induced residual stress, the average of the results given by the {200} reflections and the {211} reflections can be used for subsequent analyses. For example, from Table IX and Table X, $\sigma'_{dr,1}$ for the IF steel in the UT prestrain condition is –18.3 MPa based on {200} data,

and –18.8 MPa based on {211} data, where the average value, -18.6 MPa, will be used in further discussions about deformation induced residual stress components.

Table IX: Deformation Induced* Residual Stresses Based on {200} Reflections

Steel	Prestrain Mode	$\sigma_{dr,ij}$			$\sigma_{dr,m}$	$\sigma'_{dr,ij}$		
		$\sigma_{dr,1}$	$\sigma_{dr,2}$	$\sigma_{dr,3}$		$\sigma'_{dr,1}$	$\sigma'_{dr,2}$	$\sigma'_{dr,3}$
IF	UT	98.6	110.7	141.3	116.9	-18.3	-6.1	24.4
	PS	40.2	32.1	49.8	40.7	-0.5	-8.6	9.1
	BB	-9.8	-36.8	22.9	-7.9	-1.9	-28.9	30.8
HSLA	UT	154.9	207.7	214.7	192.5	-37.6	15.3	22.3
	PS	64.8	65.8	61.7	64.1	0.7	1.7	-2.4
	BB	-84.8	-109.5	-63.8	-86.0	1.2	-23.5	22.3
DP	UT	-11.9	143.0	181.9	104.3	-116.2	38.6	77.6
	PS	-95.9	-36.2	53.8	-26.1	-69.8	-10.1	79.9
	BB	-154.4	-144.5	41.6	-85.7	-68.7	-58.7	127.4

*After 5 pct major strain in the longitudinal (1) direction – all values in MPa.

Table X: Deformation Induced* Residual Stresses Based on {211) Reflections

Steel	Prestrain Mode	$\sigma_{dr,ij}$			$\sigma_{dr,m}$	$\sigma'_{dr,ij}$		
		$\sigma_{dr,1}$	$\sigma_{dr,2}$	$\sigma_{dr,3}$		$\sigma'_{dr,1}$	$\sigma_{dr,2}$	$\sigma_{dr,3}$
IF	UT	-4.1	19.0	29.3	14.7	-18.8	4.3	14.6
	PS	19.0	14.1	45.2	26.1	-7.1	-12.0	19.1
	BB	33.7	23.1	48.3	35.1	-1.3	-11.9	13.3
HSLA	UT	-13.9	12.3	22.3	6.9	-20.8	5.4	15.4
	PS	49.7	23.7	53.8	42.4	7.3	-18.7	11.4
	BB	56.7	30.3	54.2	47.0	9.6	-16.8	7.1
DP	UT	-104.7	68.9	58.9	7.7	-112.4	61.2	51.2
	PS	-93.1	6.0	72.5	-4.9	-88.2	10.8	77.4
	BB	-73.4	-55.8	70.5	-19.6	-53.9	-36.2	90.1

*After 5 pct major strain in the longitudinal (1) direction – all values in MPa.

Figure 75 shows the calculated deviatoric residual stress components (σ'_{dr}) for each material in each prestrain condition [$\varepsilon_{maj} = \varepsilon_L = \varepsilon_1 = 0.05$; for uniaxial tension (UT), plane strain (PS) and balanced biaxial stretching (BB) prestrain].

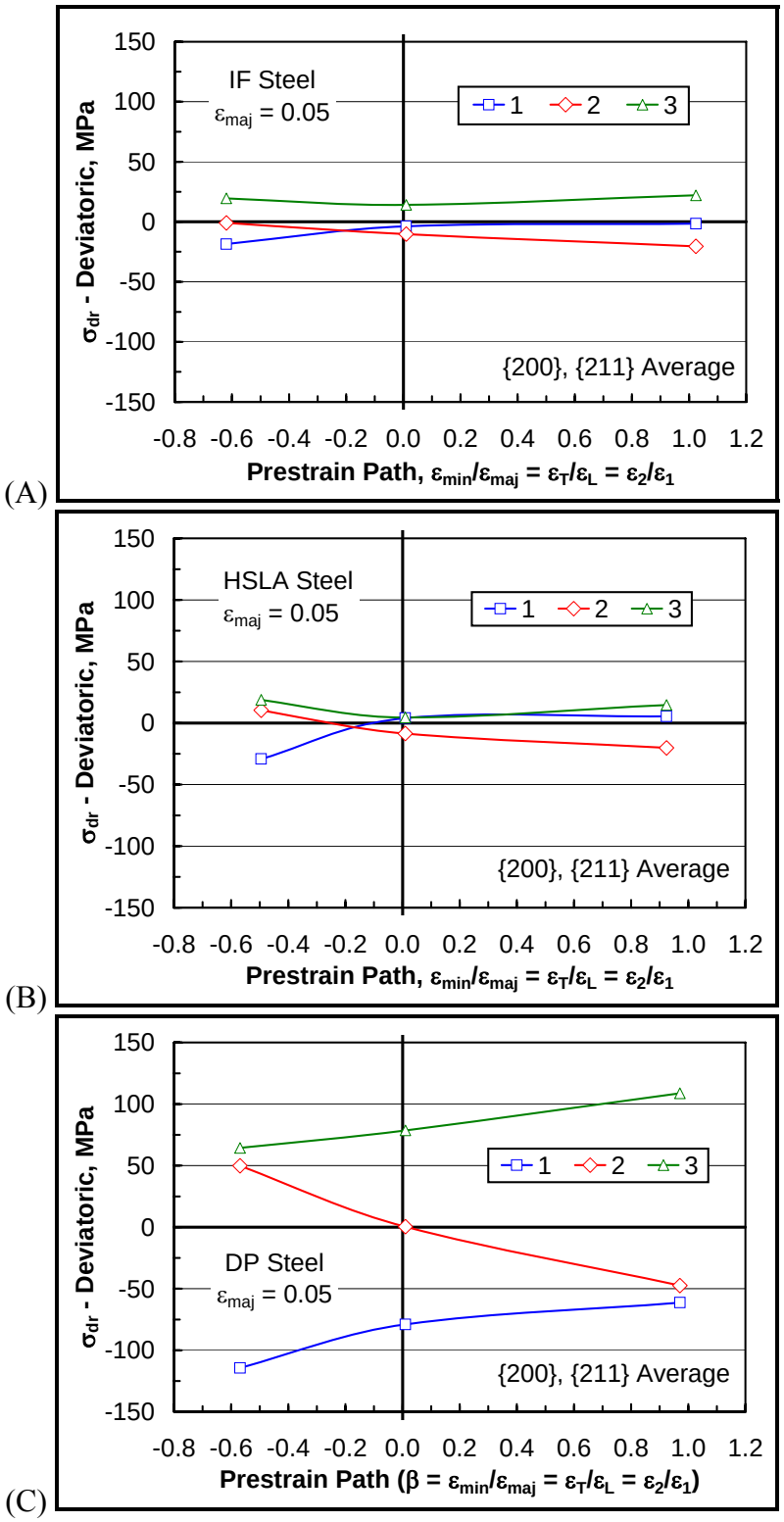

Figure 75: Deviatoric components of σ_{dr} (deformation-induced residual stress) for various prestrain paths —(A) IF steel, (B) HSLA steel and (C) DP steel. The designations 1, 2 and 3 refer to the principal directions and correspond to the longitudinal (L), transverse (T) and thickness dimensions of the samples. For each case, $\varepsilon_{maj} = \varepsilon_L = \varepsilon_1 = 0.05$.

The IF steel and the HSLA steel (Figure 75A and B, respectively) show very similar residual stress distributions, where the principal stress components of $\sigma'_{dr,ij}$ ($\sigma'_{dr,1}$, $\sigma'_{dr,2}$ and $\sigma'_{dr,3}$) fall within a ~ 50 MPa band for all prestrain modes (UT prestrain: $\beta \sim -0.5$; PS prestrain: $\beta \sim 0$; and BB prestrain: $\beta \sim 1$). The $\sigma'_{dr,1}$ component [longitudinal (L) direction or sheet rolling direction—parallel to ε_{maj}] increases slightly as β increases, while the $\sigma'_{dr,2}$ component [transverse (T) direction—parallel to ε_{min}] decreases proportionately. The $\sigma'_{dr,3}$ component (thickness direction) shows a minimum for the plane strain deformation mode ($\beta \sim 0$). Note that the deviatoric components of the deformation induced residual stresses reflect the {200} and {211} interplanar spacing changes shown in Figure 74A through D.

The DP steel (Figure 75C) shows a tremendously different residual stress distribution in contrast to the IF and HSLA steels (*i.e.*, in terms of the *magnitude* of the deformation induced residual stress components for each prestrain mode). As for the IF and HSLA steels, the $\sigma'_{dr,1}$ component increases (becomes less negative) as β increases, while $\sigma'_{dr,2}$ decreases. The thickness direction component, $\sigma'_{dr,3}$, increases as β increases. It has become clear that, for the DP steel, the deviatoric components of the deformation-induced residual stress state are proportional to and opposite in sign to the principal strain components associated with each prestrain mode. For example, for each prestrain mode, the major strain ($\varepsilon_{maj} = \varepsilon_L = \varepsilon_1$) is always positive, and $\sigma'_{dr,1}$ is always negative. Similarly, the thickness direction strain (ε_3) is always negative, while $\sigma'_{dr,3}$ is always positive. Furthermore, regarding the minor strain ($\varepsilon_{min} = \varepsilon_T = \varepsilon_2$), $\sigma'_{dr,2}$ changes from positive to negative as β (and ε_{min}) increases from negative to positive. Further evidence of the interdependence of $\sigma'_{dr,ij}$ and ε_{ij} is given by the following observations:

- $\sigma'_{dr,2} \sim \sigma'_{dr,3}$ when $\varepsilon_2 \sim \varepsilon_3$ (UT prestrain: $\beta \sim -0.6$),

- $\sigma'_{dr,2} \sim 0$ when $\varepsilon_2 \sim 0$ (PS prestrain: $\beta \sim 0.0$) and
- $\sigma'_{dr,2} \sim \sigma'_{dr,1}$ when $\varepsilon_2 \sim \varepsilon_1$ (BB prestrain: $\beta \sim 1.0$).

The results shown in Table IX and Table X and in Figure 75 are a testament to the importance of neutron diffraction methods in the characterization of residual stresses. Specifically, had another near-surface method been used (*e.g.*, X-ray diffraction), the large thickness direction components of the deformation-induced residual stresses (in principal direction 3) would not have been detected for the DP steel. It would not have been possible to factor out the hydrostatic stress component, $\sigma_{dr,m}$, from the total stress tensor, $\sigma_{dr,ij}$, to arrive at the deviatoric stress components, $\sigma'_{dr,ij}$. The implications of the calculated deformation-induced residual stresses shown in Figure 75, in the context of post-forming tensile properties, are discussed in Section 6.3.

6.0 DISCUSSION

In this chapter, the post-forming tensile properties and work hardening behavior will be directly related to the calculated prestrain-induced residual stresses (based on neutron diffraction experiments). Specifically, the 5% major strain ($\varepsilon_{maj} = \varepsilon_L = 0.05$) condition will be considered for each material for each of the experimental plane stress prestrain modes (uniaxial tension, plane strain and balanced biaxial stretching). First, in Section 6.1, the post-forming L-direction and T-direction tensile stress/strain behavior will be discussed. Then the anticipated relationships between deformation-induced residual stresses and post-forming tensile yield strength and differential hardening will be explored in Section 6.2. Then, in Section 6.3, a comparison between the predicted material behavior and the experimental results is made. Finally, various practical implications of this work are illustrated in Section 6.4.

6.1 TENSILE STRESS/STRAIN BEHAVIOR OF PRESTRAINED SAMPLES

In Sections 5.3 and 5.4, the residual tensile ductility and yield strength evolution, as a function of prestrain, were shown for the IF steel, the HSLA steel and the DP steel. In this section, the subsequent tensile stress/strain behavior, after prestraining, is examined more closely. For this analysis, the 5% major strain condition ($\varepsilon_{maj} = \varepsilon_L = 0.05$), for each prestrain mode, was chosen to correlate with the neutron diffraction residual stress analysis (see Section 5.5). L-direction

tensile specimens were machined from the same prestrained panels from which the neutron diffraction specimens were extracted. As mentioned in Section 5.4.4, it was necessary to prepare separate prestrained panels for subsequent L-direction and T-direction tensile tests. Table XI summarizes the 5% major strain samples used for the neutron diffraction experiments and the duplicate samples used for T-direction tensile tests. Although all of the samples listed in Table XI were nominally prestrained to a major strain of 5%, there are unavoidable minor variations between "duplicate" samples. It is not expected that these minor variations play a significant role in dictating the directional tensile stress/strain behavior discussed in the following.

Table XI: 5 % Major Strain Samples used in Neutron Diffraction Analysis

Steel	Neutron Diffraction Samples: L-direction Tensile Tests						Duplicate Samples: T-direction Tensile Tests					
	UT Prestrain		PS Prestrain		BB Prestrain		UT Prestrain		PS Prestrain		BB Prestrain	
	ε_{maj}	ε_{min}	ε_{maj}	ε_{min}	ε_{maj}	ε_{min}	ε_{maj}	ε_{min}	ε_{maj}	ε_{min}	ε_{maj}	ε_{min}
IF	0.051	-0.032	0.050	0.001	0.052	0.052	0.050	-0.031	0.050	0.000	0.049	0.051
HSLA	0.050	-0.024	0.052	0.001	0.050	0.044	0.049	-0.026	0.051	0.000	0.051	0.049
DP	0.048	-0.026	0.050	0.000	0.049	0.048	0.049	-0.029	0.051	0.001	0.048	0.047

6.1.1 **UT Prestrain Mode: Post-Forming Tensile s/e Curves**

Figure 76 summarizes the post-forming tensile stress/strain (s/e) behavior after uniaxial tension (UT) prestrain ($\varepsilon_{maj} = \varepsilon_L = 0.05$). In this figure, the post-forming tensile s/e curves of the IF, HSLA and DP steels are shown together for both L-direction and T-direction tensile tests. For this prestrain condition, all materials exhibit Type 1 tensile s/e behavior in the L-direction and T-direction tensile tests (see Section 5.3.1 for review of Type 1 and Type 2 tensile s/e behavior).

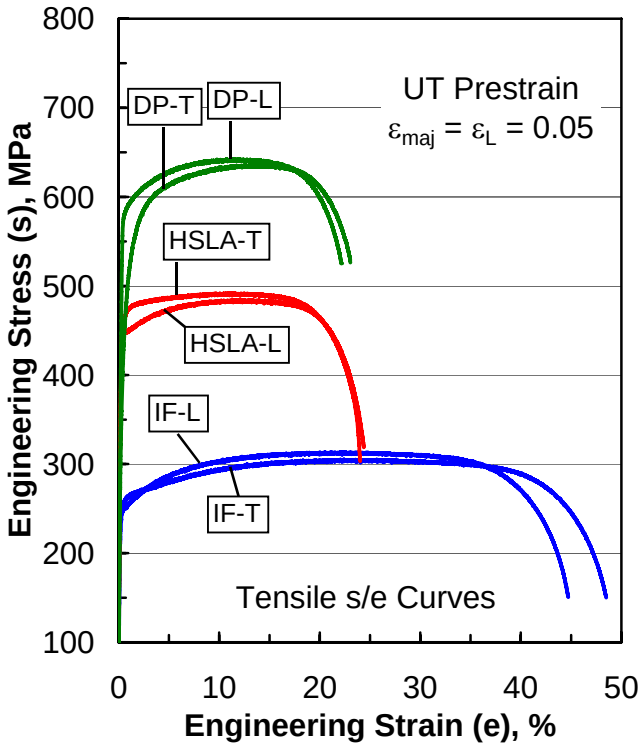

Figure 76: Post-forming tensile stress/strain curves (L and T directions) after uniaxial tension (UT) prestrain ($\varepsilon_{maj} = \varepsilon_L = 0.05$).

The IF steel and the HSLA steel exhibit a mild cross-hardening response, where the T-direction flow stress is initially higher than the L-direction flow stress. Recall that (Figure 62B and D), for the UT prestrain mode, the transition from a Type 1 to a Type 2 tensile response, in the T-direction, occurs at an effective prestrain between 0.05 and 0.1 for the IF steel and the HSLA steel ($\varepsilon_{maj} = \varepsilon_L$). Before the transition, the T-direction total elongation (TEL), uniform elongation (UEL) and post-uniform elongation (PUEL) values are similar to the corresponding L-direction values. After the transition, the T-direction UEL and TEL values are below the corresponding L-direction values for a given prestrain condition. At about 3% tensile elongation (Figure 76), the L-direction and T-direction tensile s/e curves intersect for the IF steel, and the L-direction flow stress exceeds the T-direction flow stress as tensile deformation continues. As discussed in Section 5.4.3, the HSLA steel has intrinsically greater anisotropy in mechanical

properties (in the as-produced condition, the T-direction yield strength and ultimate tensile strength are significantly greater than the corresponding L-direction values). Because of the inherently greater anisotropy, the HSLA steel shows no crossover point (the tensile flow stress is higher in the T-direction throughout the tensile test). For this particular prestrain condition, the overall T-direction residual ductility is not significantly affected by the mild cross-hardening effect; however, the cross-hardening effect (latent work hardening) dominates the T-direction residual ductility for larger UT prestrains (see Figure 62B and D).

Similar to the IF steel and the HSLA steel, the overall residual tensile ductility after UT prestrain ($\varepsilon_{maj} = \varepsilon_L = 0.05$) is similar for the L-direction and T-direction tensile tests (Figure 76) for the DP steel. Recall that, for the DP steel (Figure 62F), there is no distinct transition from Type 1 to Type 2 T-direction tensile stress/strain behavior for the UT prestrain mode in the range examined. Also recall that the cross-softening effect is greatest in the DP steel for the UT prestrain mode. For the particular example shown in Figure 76, it is clear that the intense cross-softening effect diminishes quickly as tensile deformation continues (*i.e.*, the L-direction and T-direction s/e curves converge). It is possible that the cross-softening mechanism in the DP steel serves to alleviate or mask the underlying cross-hardening (latent work hardening) mechanism displayed more prominently by the IF steel and the HSLA steel. It is also likely that the mechanism responsible for the cross-softening response diminishes as secondary tensile deformation continues—assuming that an elastic distribution of prestrain-induced residual stresses is the responsible mechanism (also discussed in Section 5.4.4).

6.1.2 **PS Prestrain Mode: Post-Forming Tensile s/e Curves**

The post-forming tensile stress strain curves after plane strain (PS) prestrain ($\varepsilon_{maj} = \varepsilon_L = 0.05$) are shown in Figure 77. For the IF steel and the HSLA steel, the most significant

difference between L-direction and T-direction tensile behavior is observed after PS prestrain. Recall that the cross-hardening effect is most pronounced for the PS prestrain mode (see Figure 69). While the L-direction tensile test reveals "normal" stress/strain behavior (Type 1 behavior) for the IF and HSLA steels, the T-direction tensile tests reveal the characteristic effects of latent work hardening discussed in Section 2.7.4 (Type 2 behavior), and the overall tensile ductility is decreased in contrast to the L-direction. Recall that, for the IF steel and the HSLA steel, the transition from Type 1 to Type 2 tensile stress/strain behavior occurs at an effective prestrain around 0.05 for PS prestrain followed by tension in the T-direction (Figure 63B and D). The net result of the intense cross-hardening response is that the TEL is almost entirely comprised of post-peak-stress deformation in the T-direction. That is, the ultimate tensile strength (UTS) occurs at a very low strain value, and thus the post-uniform elongation (PUEL) is very large. The difference in L-direction and T-direction tensile behavior, for the IF and HSLA steels in the PS prestrain condition, is very similar to that reported by Yan *et al*. [62] for a low-carbon steel (see Figure 46). For this particular complex strain path (PS prestrain followed by transverse tension), the tensile work hardening behavior of the IF steel and the HSLA steel are discussed in more detail in Section 6.1.7 (in contrast to the DP steel).

In contrast to the IF steel and the HSLA steel, the DP steel shows Type 1 tensile stress/strain behavior in both L-direction *and* T-direction tensile tests after PS prestrain. Recall that the cross-softening response in the DP steel is less intense for the PS prestrain mode than for the UT prestrain mode (Figure 68 and Figure 69), but still appears to be strong enough to counteract the underlying latent work hardening effect that dominates the low-strain T-direction tensile stress/strain behavior of the IF and HSLA steels after PS prestrain. The T-direction tensile flow stress of the DP steel exceeds that in the L-direction after approximately 2% tensile

deformation (*i.e.*, there is a crossover point at about 2% elongation). Again, as for the UT prestrain mode, the cross-softening effect is diminished as tensile deformation continues.

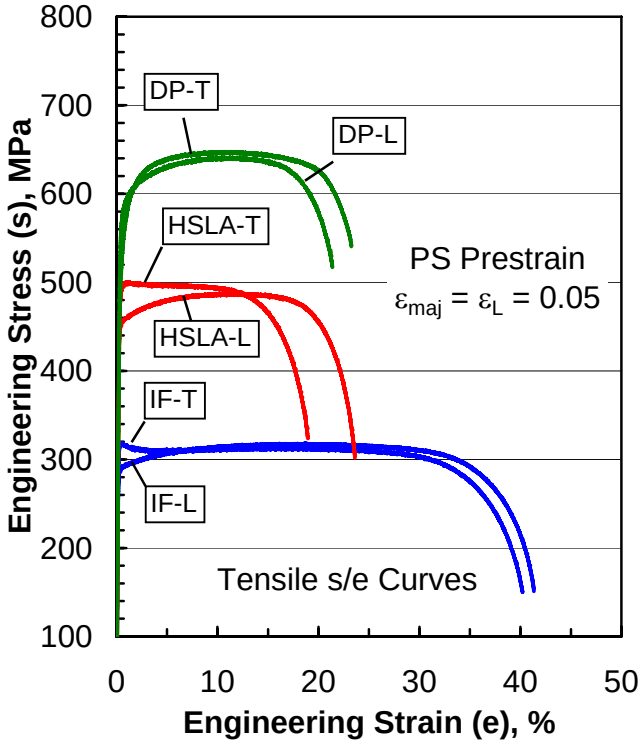

Figure 77: Post-forming tensile stress/strain curves (L and T directions) after plane strain (PS) prestrain ($\varepsilon_{maj} = \varepsilon_L = 0.05$).

6.1.3 **BB Prestrain Mode: Post-Forming Tensile s/e Curves**

The post-forming tensile stress strain curves after balanced biaxial stretching (BB) prestrain ($\varepsilon_{maj} = \varepsilon_{min} = 0.05$) are shown in Figure 78. The IF steel and the HSLA steel show similar tensile responses in the L and T directions (Type 2 behavior—see Section 5.3.1), as expected from the planar symmetry of the prestrain mode. However, it should be noted that the tensile response is similar to that shown in the T-direction for the PS prestrain condition. Therefore, it seems that, for the IF and HSLA steels, the cross-hardening mechanism (latent work hardening) is operative in both directions (L and T) for tensile deformation following BB prestrain.

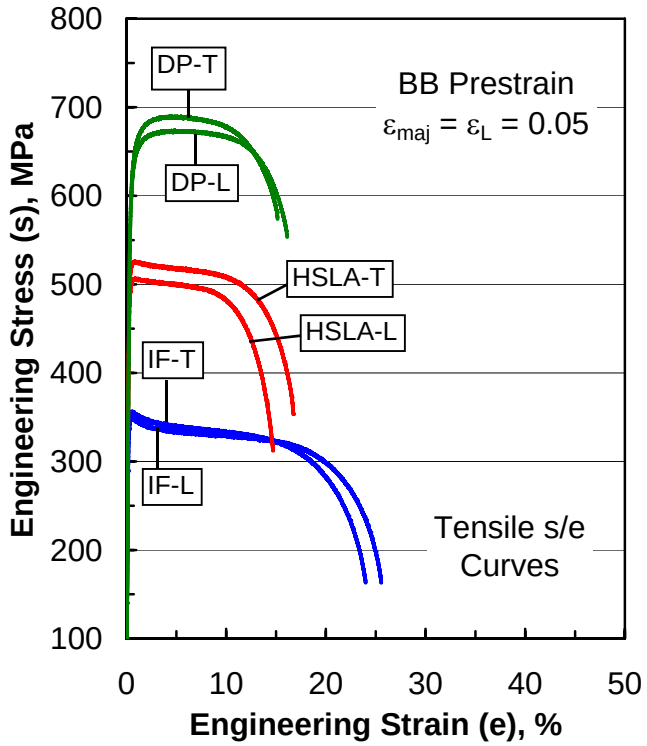

Figure 78: Post-forming tensile stress/strain curves (L and T directions) after balanced biaxial stretching (BB) prestrain ($\varepsilon_{maj} = \varepsilon_L = 0.05$).

Unlike the IF steel and the HSLA steel, the DP steel shows Type 1 tensile stress/strain behavior in *both* the L and T directions after BB prestrain. Additionally, there appears to be no latent work hardening effect, in either the L or T direction, for the BB prestrain mode (or possibly the effects of latent work hardening are masked). It is suspected that the large deformation-induced residual stresses (see Figure 75C), generated during prestraining, are responsible for the unique post-forming tensile stress/strain response of the DP steel (for all prestrain modes considered in this study). The persistence of Type 1 tensile stress/strain behavior after BB prestrain suggests that the mechanism responsible for cross-softening after UT and PS prestrain also affects the tensile response after BB prestrain, albeit symmetrically. The relationships between post-forming tensile properties and prestrain-induced residual stresses are discussed further in Sections 6.2 through 6.3.

The IF steel and the HSLA steel show remarkably similar subsequent tensile stress/strain behavior for all prestrain modes considered. This observation is especially remarkable considering the vast differences in mechanical properties (including anisotropy), microstructure, and composition between the two steels. More important, in the context of the objective stated in Section 3.0, is the strikingly unique behavior exhibited by the DP steel. The observations concerning the overall post-forming tensile stress/strain behavior of the IF steel, HSLA steel and DP steel are summarized in Table XII. The greatest differences in post-forming tensile stress/strain behavior between materials (and between tensile test directions in a given material) occur in low tensile strain intervals (at and immediately after yielding). As such, a closer look at post-forming tensile yielding behavior is taken in sections 6.1.4 through 6.1.6.

Table XII: Summary of Post-Forming Tensile s/e Behavior (Prestrain: $\varepsilon_{maj} = \varepsilon_L = 0.05$)

Steel	UT Prestrain Mode		PS Prestrain Mode		BB Prestrain Mode	
	L-Direction	T-Direction	L-Direction	T-Direction	L-Direction	T-Direction
IF	Type 1	Type 1	Type 1	Type 2	Type 2	Type 2
HSLA	Type 1	Type 1	Type 1	Type 2	Type 2	Type 2
DP	Type 1	Type 1	Type 1	Type 1	Type 1	Type 1

White: Cross-Softening; Grey: Nearly Isotropic Hardening; Black: Cross-Hardening

6.1.4 **Tensile Yielding Behavior after UT Prestrain**

To illustrate the post-forming tensile yielding behavior more clearly, the tensile stress/strain curves from Figure 76 through Figure 78 are re-plotted in Figure 79 over the strain interval from 0 to 2% engineering strain. The post-forming tensile stress/strain curves associated with each prestrain mode are grouped separately (Figure 79A – UT prestrain; Figure 79B – PS prestrain; and Figure 79C – BB prestrain), and the L-direction and T-direction curves are shown together for the IF, HSLA and DP steels in each case.

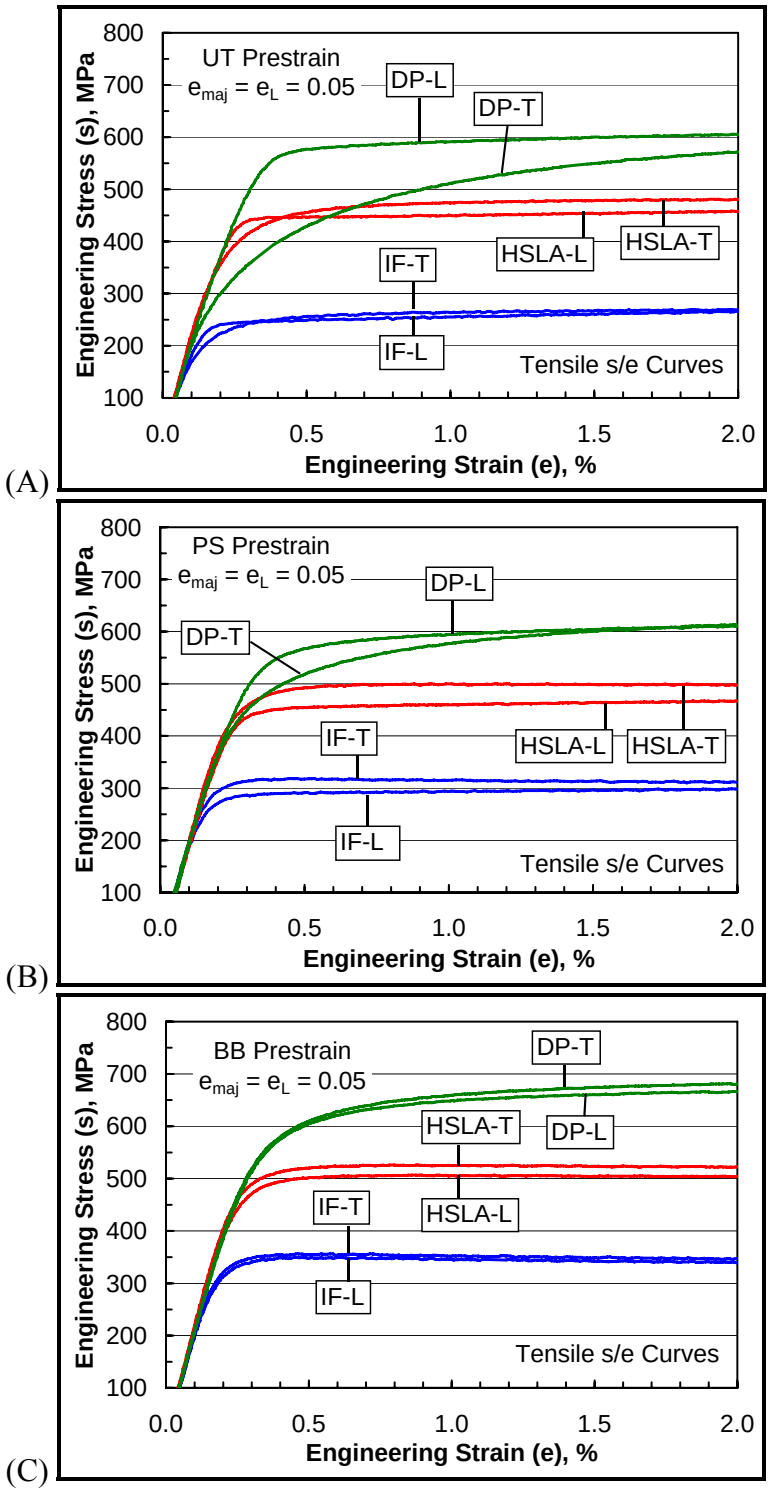

Figure 79: Post-forming tensile yielding behavior (L and T directions) for various prestrain modes—(A) uniaxial tension (UT) prestrain; (B) plane strain (PS) prestrain; and (C) balanced biaxial stretching (BB) prestrain. For each prestrain mode, the IF steel, HSLA steel and DP steel curves are shown together as indicated.

For the UT prestrain condition ($\varepsilon_{maj} = \varepsilon_L = 0.05$), the IF steel and the HSLA steel show nearly identical behavior, where the T-direction tensile flow stress is lower than that in the L-direction at very small strains ($e < 0.3\%$). A crossover occurs between 0.3% and 0.4% strain, where the T-direction flow stress exceeds the L-direction flow stress at larger strains. It appears that the observed cross-hardening effect is preceded by a very mild cross-softening effect—similar to the DP steel, but of much smaller intensity. It is believed that this behavior is an original observation that was previously unreported in the literature for conventional "single phase" steels. Interestingly, the 0.2% offset flow stress occurs approximately at the crossover point for both the IF steel and the HSLA steel. Recall the observed nearly isotropic hardening response for the UT prestrain mode for these two materials (see Figure 65A). It is clear that, depending on the method by which the "yield strength" is measured, one would conclude isotropic hardening, cross-softening, or cross-hardening, when assessing the subsequent tensile response of the IF and HSLA steels after UT prestrain. Figure 79A reveals the complex nature of low strain yielding and post-yielding tensile stress/strain behavior and further supports the idea that multiple mechanisms dictate the post-forming tensile response (that is, both cross-hardening and cross-softening mechanisms operate simultaneously at various intensities). It is believed that the initial yielding behavior (plastic strain below $e \sim 0.3\%$) is influenced by a transient elastic phenomenon such as the prestrain-induced residual stresses shown in Figure 75A and B (recall that the measured deformation-induced residual stresses in the IF steel and the HSLA steels are small in contrast to the DP steel, yet non-zero). The observed crossover implies that latent work hardening takes effect only after yielding in the T-direction and/or that the initial effects of deformation-induced residual stresses are diminished as tensile deformation proceeds. Note that, for the IF steel, two crossover points are observed—the first occurs at about 0.3%

elongation (Figure 79A), and the second occurs at about 3% elongation—after the latent work hardening effect is "pulled through" (Figure 76).

For the DP steel (Figure 79A), there is no crossover point, and the T-direction tensile flow stress is lower than that in the L-direction throughout the entire tensile test. Recall that, for the DP steel, the cross-softening effect is strongest for the UT prestrain mode (see Figure 65, Figure 68 and Figure 73). Also recall that there is no transition from Type 1 to Type 2 tensile behavior in the T-direction at higher UT prestrain levels, within the range examined—in contrast to the IF and HSLA steels (see Figure 62B, D and F). While the low-strain cross-softening effect is much more prominent for the DP steel (in contrast to the IF and HSLA steels), the difference between the L-direction and T-direction tensile flow stress diminishes rapidly as tensile deformation continues. Thus, there is some ambiguity regarding the relative contributions of latent work hardening and prestrain-induced residual stresses to the transient cross-softening effect.

It is reasonable to assume that, since the cross-hardening effect is relatively weak for the IF steel and the HSLA steel for the subject prestrain condition, the differential low-strain tensile behavior of the DP steel is a direct reflection of a decaying residual stress pattern (established during UT prestraining in the L-direction) that is disturbed by tensile deformation in the T-direction. Conversely, the prestrain-induced residual stress pattern is reinforced by further L-direction tensile deformation. It is likely that, if the T-direction tensile deformation were interrupted after a few percent elongation, a new deformation-induced residual stress pattern would be measured in the ferrite phase—similar to that developed during the prestrain step, but aligned with respect to the principal strain axes of T-direction tensile deformation (see Figure 75c). That is, a compressive residual stress would develop in the T-direction (principal direction

2), and positive residual stresses would be measured in the L-direction and the thickness direction (principal directions 1 and 3, respectively).

This supposition could be verified (or possibly invalidated) by additional neutron diffraction residual stress measurements of samples subjected to two-stage prestrains. Additional valuable insight would be gained not only by measuring deformation-induced residual stresses after deformation in simple strain modes (as done in this research program), but also by monitoring the *changes* in the residual stress distribution that occur once the strain path is changed, and as deformation progresses along the secondary strain path. For example, considering the post-forming tensile s/e curves of the DP steel after UT prestrain (Figure 79A), it would be interesting to examine the deformation-induced residual stresses at 0.5%, 1% and 2% tensile deformation in the L and T directions (for starters). It remains uncertain whether the apparent diminishing cross-softening effect of the DP steel (convergent L-direction and T-direction tensile s/e curves in Figure 79A) is caused by a decaying residual stress pattern, or by the evolution of a new residual stress pattern during secondary T-direction tensile deformation, or both.

6.1.5 **Tensile Yielding Behavior after PS Prestrain**

Figure 79B shows the post-forming tensile yielding behavior for the PS prestrain mode ($\varepsilon_{maj} = \varepsilon_L = 0.05$). The aforementioned cross-hardening behavior of the IF steel and the HSLA steel clearly prevails over other low-strain phenomena, such as the initial mild cross-softening observed after UT prestrain (Figure 79A).

As for the UT prestrain condition (Figure 79A), the DP steel initially shows a clear cross-softening response after PS prestrain (Figure 79B) that diminishes quickly with increasing tensile deformation. As shown in Figure 77, there is a crossover at about 2% tensile elongation, where

the T-direction flow stress exceeds that in the L-direction as tensile deformation continues. It appears that the cross-softening response in the DP steel is relatively insignificant for the PS prestrain condition (in contrast to the UT prestrain condition). However, it is important to realize that the *mechanism* responsible for the cross-softening effect likely affects the *L-direction* tensile behavior after PS prestrain ($\varepsilon_{maj} = \varepsilon_L$), as the strain path has been changed between the prestrain step and the secondary tensile deformation. For the UT prestrain condition (Figure 79A), the L-direction tensile test is merely a continuation of the prestrain mode of deformation—with no strain path change. As such, the *difference* between the L-direction and T-direction low-strain tensile response after PS prestrain may not reflect the magnitude of the influence of prestrain-induced residual stresses on post-forming tensile stress/strain behavior, for example. This is especially true for balanced biaxial stretching prestrain, as the prestrain deformation is symmetric (next section). The anticipated effects of prestrain-induced residual stresses on post-forming tensile yielding behavior are discussed in Section 6.2.

6.1.6 **Tensile Yielding Behavior after BB Prestrain**

The post-forming tensile yielding behavior for the BB prestrain mode ($\varepsilon_{maj} = \varepsilon_{min} = 0.05$) is shown in Figure 79C. Clearly, the symmetric post-forming tensile response is a reflection of symmetry of the prestrain mode. That is, as the materials were deformed equally in the L and T directions during the prestrain step, it follows that the deformation response is similar for tension applied in the L and T directions. The minor variations in L-direction and T-direction yielding behavior for each material reflect the intrinsic anisotropy in mechanical properties reported for the as-produced condition (Table VII).

Again, it is important to consider that the IF steel and the HSLA show Type 2 behavior in the L and T directions after BB prestrain, while the DP steel exhibits Type 1 behavior in both

directions. Latent work hardening appears to affect symmetrically the post-forming tensile response of the IF and HSLA steels after BB prestrain, while latent hardening is either absent or masked (by large prestrain-induced residual stresses, for example) in the case of the DP steel.

6.1.7 **A Closer Look at Post-Forming Tensile Work Hardening**

In reviewing Table XII, it is clear that the PS prestrain mode reveals the most interesting post-forming tensile response behavior—in terms of both material differences and directionality in tensile behavior (L-direction vs. T-direction). For the particular PS prestrain condition considered in this portion of the analysis ($\varepsilon_{maj} = \varepsilon_L = 0.05$), it was found that the IF steel and the HSLA exhibit the characteristics of latent work hardening during subsequent T-direction tensile deformation. The cross-hardening effect results in Type 2 tensile behavior (Section 5.3.1) that is characterized by grossly unbalanced contributions of uniform elongation (UEL) and post-uniform elongation (PUEL) to the total elongation (TEL), where the UEL is severely diminished (around 1% or less), and PUEL is nearly equivalent to TEL. The characteristics of cross-hardening and flow softening, along with their associated mechanisms, are discussed in Sections 2.7.4 and 2.7.5. Perhaps more importantly, the DP steel shows no such latent work hardening effect and, in fact, reveals a distinct cross-*softening* behavior, where the T-direction flow stress is lower than that in the L-direction—at and immediately following yielding. In the following, the T-direction post-forming tensile stress/strain behavior, after PS prestrain ($\varepsilon_{maj} = \varepsilon_L = 0.05$), will be examined more closely.

The T-direction post-forming tensile stress/strain curves for the PS prestrain mode (Figure 77) are re-plotted in Figure 80A. For each curve the ultimate tensile strength (UTS) is marked as “Max. Stress” on the diagram, where the UTS is defined as the maximum engineering stress recorded during a tensile test. The engineering strain corresponding to the UTS (the UEL

value) usually marks the beginning of diffuse necking, where the work hardening rate is matched by the geometrical thinning associated with tensile deformation (77). Note that, for the IF steel and the HSLA steel, the maximum stress (UTS) occurs at 0.5% and 1.1% tensile engineering strain, respectively. Correspondingly, the post-uniform elongation (PUEL) values are respectively 39.8% and 17.9% (significantly higher than the T-direction PUEL values reported for the as-produced condition, Table VII). In reviewing the as-produced tensile stress/strain curves of the IF steel, the HSLA steel and the DP steel (Figure 57A and Figure 58A), "normal" engineering tensile stress/strain behavior (Type 1 behavior) may be characterized by more or less balanced contributions of uniform and post-uniform elongation to the total elongation. Additionally, "normal" stress/strain behavior is characterized by downward curvature of the engineering stress/strain curve at all points after the UTS (during post-uniform elongation). In this context, the IF steel and the HSLA steel certainly do not show "normal" tensile stress/strain behavior after the maximum engineering stress (UTS).

For the IF steel, the s/e curve exhibits upward curvature immediately after the maximum stress and, upon further tensile deformation, shows a transition toward downward curvature, and a second local maximum occurs in the s/e curve at 16.1 %. At all points after the second local maximum, the curvature of the s/e curve is downward (characteristic of a true diffuse necking response and "normal" post-uniform elongation behavior). This behavior is similar to the "8x0(T)" curve in Figure 46 reported by Yan *et al*. (62) and the schematic illustration of latent work hardening behavior in Figure 47 given by Toyoda *et al*. (63). The HSLA steel exhibits behavior similar to that of the IF steel, where the s/e curve assumes upward curvature immediately after the maximum stress value. No second local maximum is observed for the HSLA steel however, and an inflection toward downward curvature occurs at about 5%

engineering strain. This behavior is similar to the "12x0(T)" curve in Figure 46 (62). For the DP steel, the maximum stress (UTS) occurs at approximately 10.8% and the s/e curve has downward curvature throughout the entire tensile test (typical Type 1 tensile stress/strain behavior).

(A)

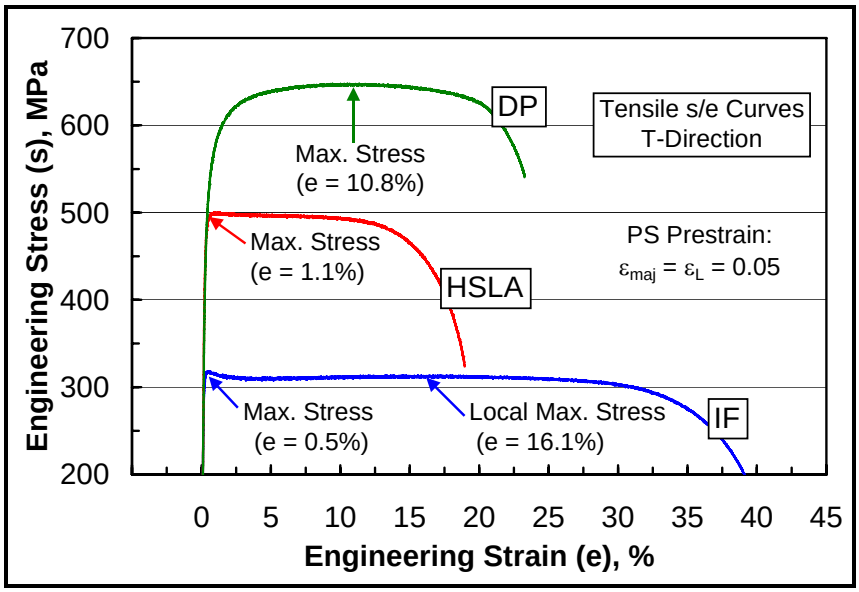

(B)

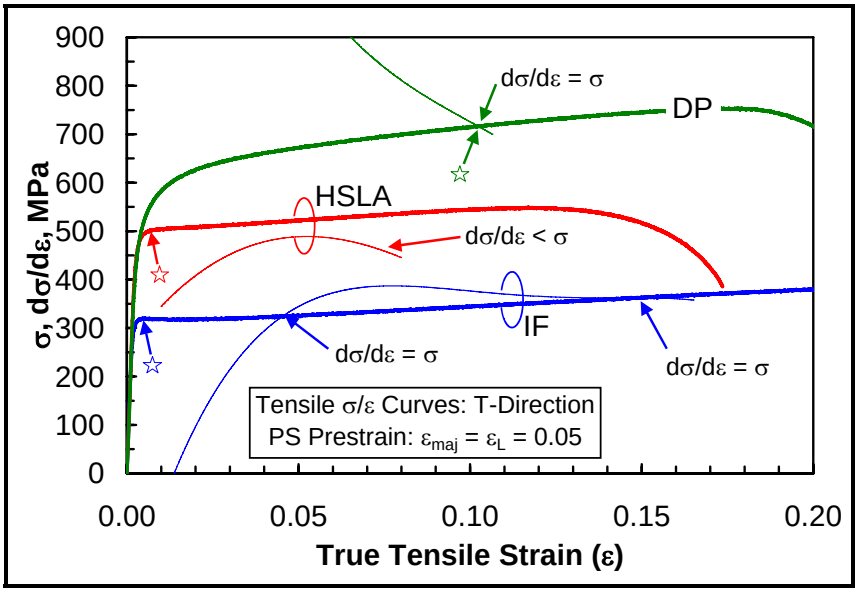

Figure 80: A closer look at the transverse (T-direction) tensile stress/strain behavior after plane strain (PS) prestrain ($\varepsilon_{maj} = \varepsilon_L = 0.05$) for the IF steel, HSLA steel and DP steel. In (A), the s/e curves are shown with maximum stress values as marked, and (B) shows the true stress/strain (σ/ε) behavior up to $\varepsilon = 0.2$ (maximum engineering stress values marked by stars). Also in (B) are the work hardening rate ($d\sigma/d\varepsilon$-vs-ε) curves. See text for details.

The engineering stress/strain (s/e) curves from Figure 80A were converted to true stress/strain (σ/ε) curves and are shown in Figure 80B (up to $\varepsilon = 0.2$), along with the respective work hardening rate curves ($d\sigma/d\varepsilon$-vs-ε) that correspond to each material. For each σ/ε curve, the maximum engineering stress (UTS) values from Figure 80A are marked by stars (first instance where $d\sigma/d\varepsilon = \sigma$). For the IF steel, the work hardening rate falls below zero ($d\sigma/d\varepsilon$ is negative) after the maximum stress value, but rises shortly thereafter (the initial portion of the work hardening rate curve has been omitted for clarity). As tensile deformation continues, $d\sigma/d\varepsilon$ rises above σ at $\varepsilon = 0.046$ (4.7% elongation); then reaches a local maximum value at $\varepsilon = 0.079$ (8.2% elongation); then decreases to intersect σ again at $\varepsilon \sim 0.15$ (16.1% elongation). In the context of "normal" stress/strain behavior, the end of uniform elongation (the start of diffuse necking) in a sheet tensile test is normally uniquely defined by $d\sigma/d\varepsilon = \sigma$. For the particular example shown in Figure 80B for the IF steel, the condition that $d\sigma/d\varepsilon = \sigma$ is apparently satisfied three times in a single tensile test as follows:

- $d\sigma/d\varepsilon = \sigma$ at 0.5% elongation ($d\sigma/d\varepsilon$ decreasing—maximum engineering stress),
- $d\sigma/d\varepsilon = \sigma$ at 4.7% elongation ($d\sigma/d\varepsilon$ increasing—inconsequential), and
- $d\sigma/d\varepsilon = \sigma$ at 16.1% elongation ($d\sigma/d\varepsilon$ decreasing—true necking begins?).

In essence, it can be said that, after the initial latent work hardening and flow softening effects, the IF steel "recovers" and displays a "normal" tensile response in the T-direction. For the IF steel, the transition from Type 1 to Type 2 post-forming tensile behavior (T-direction) occurs at an effective prestrain around 0.05 ($\varepsilon_{maj} = \varepsilon_L$) for the PS mode of prestrain (see Figure 63B). As such, it is rather fortuitous that the unique behavior illustrated by the IF steel in Figure 80 was captured and observed here. For lower amounts of PS prestrain, the T-direction tensile s/e curves of the IF steel resemble that for the UT prestrain condition (IF steel: T-direction tensile

test) shown in Figure 76, where the cross-hardening effect is merely a bump or inflection shortly after yielding. At higher amounts of PS prestrain, the T-direction tensile s/e curves show no second local maximum in the s/e curve after the UTS (true Type 2 behavior). Characteristics of both Type 1 and Type 2 behavior are clearly observed for the IF steel in Figure 80. For instance, if the second local maximum were considered the end of uniform elongation (UEL = 16.1%, rather than 0.5%), the post-uniform strain would be 24.2%, rather than 39.8%.

Regardless of one's preferred interpretation of "uniform elongation", it is certainly true that the IF steel exhibits a great deal of residual tensile ductility beyond the maximum stress value at 0.5% engineering strain. Furthermore, it is not unusual that $d\sigma/d\varepsilon = \sigma$ multiple times during a tensile test. Take, for instance, the case of the HSLA steel in the as-produced condition (T-direction tensile test shown in Figure 58). The post-yielding inflection is large enough such that a local maximum in engineering stress occurs at about e = 0.3% ($d\sigma/d\varepsilon = \sigma$), while the necking strain (UEL) reported in Table VII is 16.9% elongation (where again, $d\sigma/d\varepsilon = \sigma$). Another instance where $d\sigma/d\varepsilon = \sigma$ must occur between these two strain values. In this type of analysis, it may be more appropriate to qualify the definition of the necking strain (or uniform elongation, UEL) as the *last* local maximum on the engineering tensile stress/strain curve. The reason that the IF steel behavior in Figure 80 appears so unusual is that the last local maximum occurs *after* the maximum stress value.

For the HSLA steel (Figure 80B), the T-direction tensile work hardening behavior after PS prestrain ($\varepsilon_{maj} = \varepsilon_L = 0.05$) is relatively easier to describe in terms of the qualified definition of uniform elongation (above). For the HSLA steel in this particular prestrain condition, the last local maximum in the engineering tensile s/e curve corresponds to the maximum engineering stress (UTS). As such, after the UTS, $d\sigma/d\varepsilon < \sigma$ throughout the remainder of the tensile test, as

shown in the diagram ($d\sigma/d\varepsilon = \sigma$ only at 1.1% elongation). However, it is clear that the HSLA steel behaves very similarly to the IF steel after the maximum engineering stress (marked by the star). The work hardening rate ($d\sigma/d\varepsilon$) drops below the true flow stress (σ), but begins to rise shortly thereafter (again the initial portion of the work hardening curve has been omitted for clarity). Unlike the case of the IF steel, the work hardening rate never exceeds the true flow stress after the UTS and reaches a maximum at $\varepsilon = 0.053$ (5.4% elongation). Although the work hardening rate of the HSLA steel is higher than that of the IF steel in this strain interval, the higher inherent strength level of the HSLA steel precludes the incidence of further intersection between the $d\sigma/d\varepsilon$-vs-ε curve and the σ-vs-ε curve. Recall that, for the HSLA steel, the transition from Type 1 to Type 2 post-forming tensile behavior (T-direction) occurs at an effective prestrain of less than 0.05 ($\varepsilon_{maj} = \varepsilon_L$) for the PS mode of prestrain (see Figure 63D). At some lower undetermined PS prestrain level (greater than 0.035, but less than 0.05), the unique transitional behavior shown by the IF steel would likely be observed. In a future analysis, it would be interesting to explore these tensile deformation vagaries in greater detail, in the context of micromechanical deformation mechanisms, and the implications toward plastic instability, strain localization, and necking behavior in tension.

However, for this research program, the most interesting result is the rather uninteresting post-forming tensile response of the DP steel. For the PS prestrain condition ($\varepsilon_{maj} = \varepsilon_L = 0.05$), the DP steel exhibits true Type 1 tensile stress/strain behavior in the T-direction tensile test, where yielding is followed by significant uniform elongation—the limit of which being defined by the intersection of a monotonically decreasing work hardening rate and the true tensile flow stress ($d\sigma/d\varepsilon = \sigma$).

6.2 POST-FORMING RESIDUAL STRESS DISTRIBUTIONS IN DP STEELS

Throughout the discussion of the post-forming tensile stress/strain behavior (Section 6.1) various references were made to the possible influence of deformation-induced residual stresses, such as those listed in Table IX and Table X and shown graphically in Figure 75. In this section, the anticipated relationships between prestrain-induced residual stresses and post-forming tensile yield strength and differential hardening will be explored. The concept of stress state superposition will be drawn upon, and Mohr's circle of stress will be used as a conceptual visualization tool.

6.2.1 **Internal Stress Development in DP Steels**

Sugimoto *et al*. (65) proposed a model that describes internal stress development in DP steels during plastic deformation. The model is similar in form to that developed by Zhonghua and Haicheng (16)—discussed in Section 2.5.3 in the context of the Bauschinger Effect. Sugimoto *et al.* began by recognizing that, during plastic deformation of a DP steel, the magnitude of the plastic strain in the ductile ferrite phase, ε_{ij}^{F}, exceeds that of the much harder martensite phase, ε_{ij}^{M} (strain partitioning—see Section 2.4.2). As a result, internal stresses develop, and the total applied stress tensor, σ_{ij}^{A}, is partitioned between the ferrite phase (σ_{ij}^{F}) and the martensite phase (σ_{ij}^{M}) as follows:

$$\sigma_{ij}^{F} = \sigma_{ij}^{A} - fK\left(\varepsilon_{ij}^{F} - \varepsilon_{ij}^{M}\right) \text{ and} \qquad [30a]$$

$$\sigma_{ij}^{M} = \sigma_{ij}^{A} + (1-f)K\left(\varepsilon_{ij}^{F} - \varepsilon_{ij}^{M}\right), \qquad [30b]$$

where f is the volume fraction of martensite in the DP steel, and K is an elastic property factor defined as

$$K = \frac{E(7-5\nu)}{15(1-\nu^2)}, \qquad [31]$$

where E and ν are Young's modulus and Poisson's ratio, respectively. Then it was assumed that, after prestraining and full relaxation of externally applied stresses, the ferrite and martensite phases have respective plastic strains of $\varepsilon_{ij}^{F,p}$ and $\varepsilon_{ij}^{M,p}$ after elastic recovery (the superscript "p" means plastic or permanent deformation). The resultant deformation-induced residual stresses in the ferrite phase ($\sigma_{dr,ij}^{F}$) and the martensite phase ($\sigma_{dr,ij}^{M}$) are given as follows (in light of Equation 30):

$$\sigma_{dr,ij}^{F} = -fK\left(\varepsilon_{ij}^{F,p} - \varepsilon_{ij}^{M,p}\right) \text{ and} \qquad [32a]$$

$$\sigma_{dr,ij}^{M} = (1-f)K\left(\varepsilon_{ij}^{F,p} - \varepsilon_{ij}^{M,p}\right). \qquad [32b]$$

Now, if it is assumed that the martensite phase is unyielding ($\varepsilon_{ij}^{M,p} = 0$), Equation 32 becomes

$$\sigma_{dr,ij}^{F} = -fK\left(\varepsilon_{ij}^{p}\right) \text{ and} \qquad [33a]$$

$$\sigma_{dr,ij}^{M} = (1-f)K\left(\varepsilon_{ij}^{p}\right), \qquad [33b]$$

where ε_{ij}^{p} is the total plastic strain tensor of the DP steel ($\varepsilon_{ij}^{F,p} = \varepsilon_{ij}^{p}$). It should be noted that the components of $\sigma_{dr,ij}^{F}$ and $\sigma_{dr,ij}^{M}$ must balance over the entire volume of material with respect to the volume fractions of ferrite and martensite. From Equation 33, it is predicted that the components of the deformation-induced residual stress tensor in the ferrite phase ($\sigma_{dr,ij}^{F}$) are proportional to the components of the prestrain tensor (ε_{ij}^{p}), but opposite in sign. Conversely, the components of $\sigma_{dr,ij}^{M}$ are proportional to the components of ε_{ij}^{p}, and of the same sign (note that f and K are positive values).

Now, with Equation 33a, it is possible to estimate the types of post-forming, deformation-induced residual stress distributions that develop in DP steels for various prestrain modes. Recall that, in Table II, the principal strain relationships associated with uniaxial tension (UT), plane strain (PS) and balanced biaxial stretching (BB) modes of prestrain are given. From Table II and Equation 33a, the following ferrite phase residual stress distributions are anticipated (assuming an isotropic material):

$$\text{For UT prestrain: } \varepsilon_{ij}^{p} = \begin{vmatrix} \varepsilon_1 & 0 & 0 \\ 0 & -\frac{1}{2}\varepsilon_1 & 0 \\ 0 & 0 & -\frac{1}{2}\varepsilon_1 \end{vmatrix} \Rightarrow \sigma_{dr,ij}^{F} = \begin{vmatrix} -fK\varepsilon_1 & 0 & 0 \\ 0 & \frac{1}{2}fK\varepsilon_1 & 0 \\ 0 & 0 & \frac{1}{2}fK\varepsilon_1 \end{vmatrix}, \quad [34a]$$

$$\text{For PS prestrain: } \varepsilon_{ij}^{p} = \begin{vmatrix} \varepsilon_1 & 0 & 0 \\ 0 & 0 & 0 \\ 0 & 0 & -\varepsilon_1 \end{vmatrix} \Rightarrow \sigma_{dr,ij}^{F} = \begin{vmatrix} -fK\varepsilon_1 & 0 & 0 \\ 0 & 0 & 0 \\ 0 & 0 & fK\varepsilon_1 \end{vmatrix}, \text{ and} \quad [34b]$$

$$\text{For BB prestrain: } \varepsilon_{ij}^{p} = \begin{vmatrix} \varepsilon_1 & 0 & 0 \\ 0 & \varepsilon_1 & 0 \\ 0 & 0 & -2\varepsilon_1 \end{vmatrix} \Rightarrow \sigma_{dr,ij}^{F} = \begin{vmatrix} -fK\varepsilon_1 & 0 & 0 \\ 0 & -fK\varepsilon_1 & 0 \\ 0 & 0 & 2fK\varepsilon_1 \end{vmatrix}. \quad [34c]$$

A similar exercise would reveal the anticipated residual stress distributions of the martensite phase. The relationships given in Equation 34 are shown schematically by Mohr's circle representation in Figure 81. For this figure, DP steel samples have been hypothetically prestrained to the same major strain level ($\varepsilon_{maj} = \varepsilon_1$) in each of the UT, PS and BB prestrain modes. The Mohr's circle representation is a convenient way of visualizing a three-dimensional stress state in two dimensions (77). The principal components of $\sigma_{dr,ij}^{F}$ (hereafter called $\sigma_{dr,ij}$ as in Section 4.4.3) for each residual stress state are marked by the appropriate principal directions (1, 2 and 3) along the normal stress (σ) axis in Figure 81. Note that $\sigma_{dr,1}$ is the same for each prestrain mode (as $\varepsilon_{maj} = \varepsilon_1$ is the same for each prestrain mode). The dotted lines above and

below the normal stress axis mark the critical shear stress, τ_c, (defined in Section 5.2). For this analysis, it is assumed that τ_c is the same for each prestrain condition. The following elements of Mohr's circle representation are important for this analysis.

- For each stress state in Figure 81, three circles are drawn: one that passes through σ_{max} and σ_{min} ($\sigma_{dr,3}$ and $\sigma_{dr,1}$, respectively); one that passes through σ_{max} and the intermediate principal stress ($\sigma_{dr,2}$); and one that passes through σ_{min} and the intermediate principal stress.
- If the intermediate principal stress is equal to σ_{max} (or σ_{min}), the corresponding circle that connects the intermediate principal stress to σ_{max} (or σ_{min}) reduces to a point on the Mohr's circle diagram (Examples: Figure 81A and C).
- For any given stress state, the area bound by the largest circle, but outside the other two circles, defines all possible alternate representations of each stress state (after an appropriate stress axis rotation).
- If the largest circle on the diagram (that which passes through σ_{min} and σ_{max}) touches the lines marked τ_c, yielding is predicted (note that this another way of expressing the Tresca yield criterion).
- The intermediate principal stress component (less than σ_{max}, but greater than σ_{min}) has no anticipated effect on yielding (another reflection of the Tresca Yield Criterion).
- The principal directions 1, 2 and 3 refer to the original principal strain directions for each prestrain mode: 1 – major strain direction, 2 – minor strain direction, and 3 – thickness strain direction.

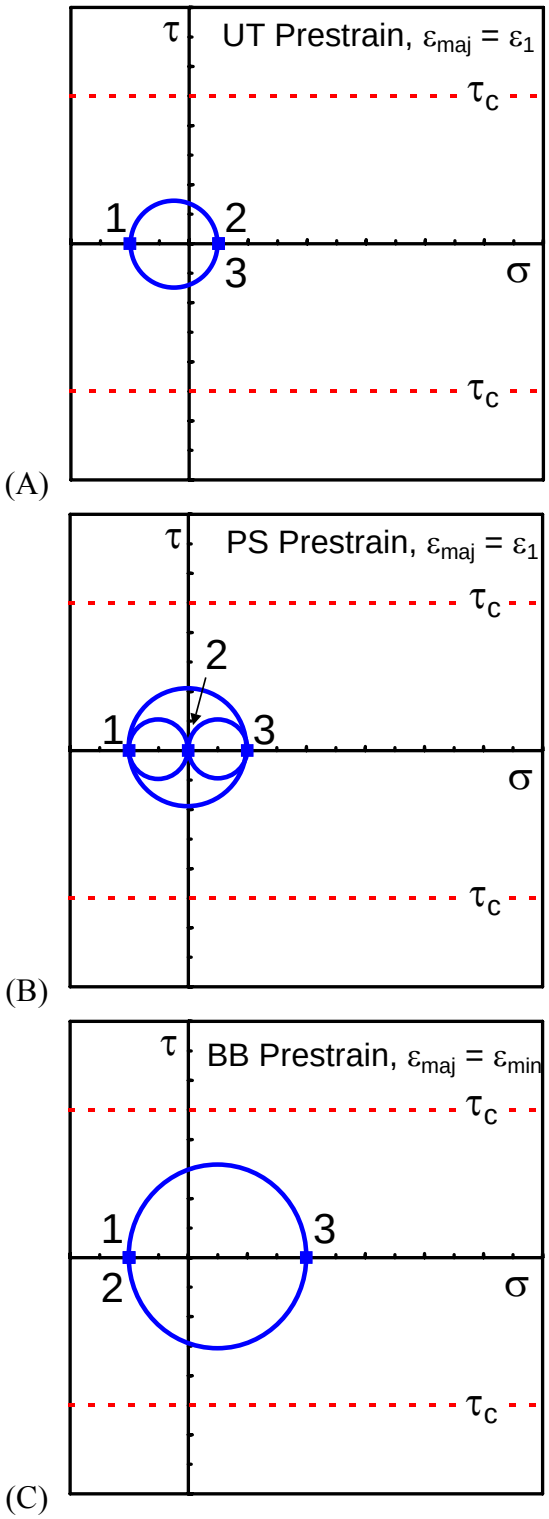

Figure 81: Schematic Mohr's circle representation of the anticipated effects of strain path on the deformation-induced ferrite residual stress state in a dual-phase steel—(A) uniaxial tension prestrain, (B) plane strain prestrain, and (C) balanced biaxial stretching prestrain. See text for details and assumptions made.

The Mohr's circle representation of $\sigma_{dr,ij}$ for the UT, PS and BB prestrain modes are shown schematically in Figure 81A, B and C, respectively. Note that, as the principal strain ratio, β, of the prestrain mode increases, the following are observed:

- The $\sigma_{dr,1}$ component is negative and does not change with β (because $\varepsilon_1 = \varepsilon_{maj}$ is positive, and also does not change with β, by convention).
- The size of the largest circle increases (the maximum residual shear stress approaches the critical shear stress).
- The $\sigma_{dr,2}$ component moves from right to left on the diagram (changes from positive to negative as β changes from negative to positive, and is zero when $\beta = 0$).
- The $\sigma_{dr,3}$ component moves from left to right on the diagram (becomes increasingly positive) as the magnitude of the thickness strain (negative) increases for a fixed major strain value.

As a hypothetical example, consider a DP steel that is prestrained to a specified major strain level in the UT, PS and BB prestrain modes ($\varepsilon_{maj} = \varepsilon_1$). Also assume that the resultant deformation-induced residual stress component in principal direction 1 ($-fK\varepsilon_1$) is –100 MPa (same for all prestrain modes). From Equation 34, the remaining prestrain-induced residual stress components can be calculated for each prestrain mode. The results of this hypothetical example are shown in Figure 82. Note the similarity between Figure 82 and Figure 75C.

From this analysis, it is clear that the distribution of deformation induced residual stresses in the ferrite phase is expected to depend greatly upon the mode of prestrain. Furthermore, it is expected that the post-forming tensile response depends not only upon the prestrain mode, but also upon the direction of applied subsequent tension (*e.g.*, parallel or perpendicular to the major prestrain axis). In the following section, the Mohr's circle representation is extended to illustrate

the expected ways in which deformation-induced residual stresses affect the post-forming tensile yield strength for DP steels.

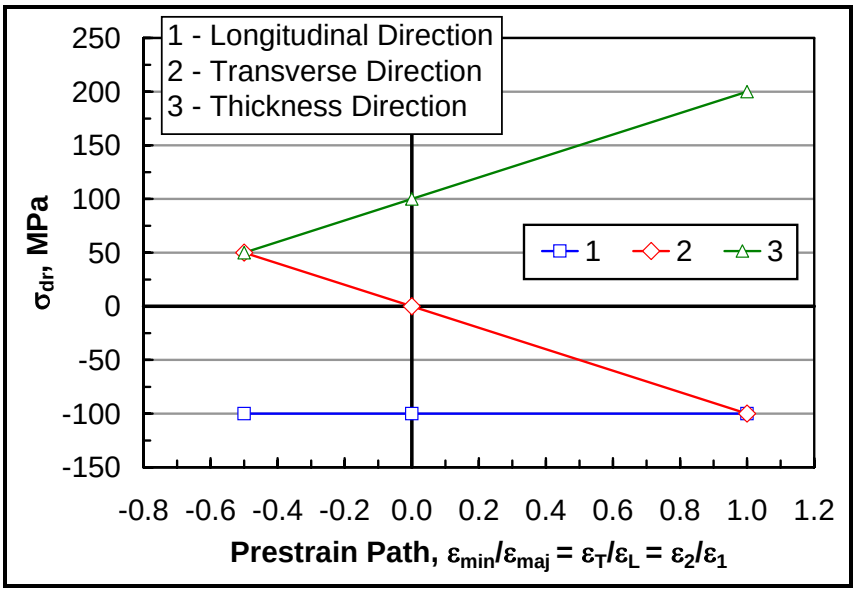

Figure 82: Schematic illustration of the influence of strain path on post-forming residual stress components in a dual-phase steel. The numbers 1, 2 and 3 refer to the principal directions and correspond to the longitudinal (L), transverse (T) and thickness dimensions. See text for details.

6.2.2 **Superposition of Residual and Applied Stresses**

Now that the anticipated influence of prestrain path on post-forming, deformation-induced residual stress distributions in DP steels has been established (Equations 33 and 34 and Figure 81), the principle of stress state superposition can be used to illustrate the expected influence of various prestrain-induced residual stress states on the directionality of post-forming tensile yield strength. The principle of superposition (77) is that two independent stress states (σ_{ij}^{1} and σ_{ij}^{2}) can be combined by direct superposition, where the individual components of which are added linearly to arrive at a third composite stress state, σ_{ij}^{3}. Or, in tensor notation:

$$\sigma_{ij}^{1}+\sigma_{ij}^{2}=\begin{vmatrix}\sigma_{11}^{1}+\sigma_{11}^{2} & \sigma_{12}^{1}+\sigma_{12}^{2} & \sigma_{13}^{1}+\sigma_{13}^{2}\\ \sigma_{12}^{1}+\sigma_{12}^{2} & \sigma_{22}^{1}+\sigma_{22}^{2} & \sigma_{23}^{1}+\sigma_{23}^{2}\\ \sigma_{13}^{1}+\sigma_{13}^{2} & \sigma_{23}^{1}+\sigma_{23}^{2} & \sigma_{33}^{1}+\sigma_{33}^{2}\end{vmatrix}=\sigma_{ij}^{3}. \qquad [35]$$

Specifically, σ_{ij}^{1} may be a prestrain-induced residual stress state, and σ_{ij}^{2} may be a post-forming applied elastic stress such as uniaxial tension in a tensile test. Now consider that, for each of the deformation-induced residual stress states shown in Figure 81, an elastic uniaxial tensile stress ($< 2\tau_c$) is applied in either the sheet longitudinal (L) direction (principal direction 1) or the sheet transverse (T) direction (principal direction 2). Using the principle of superposition, the composite stress states are shown schematically in Figure 83 through Figure 85 for the UT prestrain mode, the PS prestrain mode and the BB prestrain mode.

For the case of UT prestrain ($\varepsilon_{maj} = \varepsilon_1 = \varepsilon_L$), the superposition of an elastic uniaxial tension stress over the prestrain-induced residual stress state is shown schematically in Figure 83A for L-direction tension (tension axis in principal direction 1) and in Figure 83B for T-direction tension (tension axis in principal direction 2). Note that, although the L-direction and T-direction applied tensile stresses are of the same magnitude, very different composite stress states are realized by the respective superpositions. For tension applied in the L-direction, the maximum shear stress, after stress state superposition (top of the circle on the Mohr's circle diagram), is well below the critical shear stress, τ_c (*i.e.*, the material is far from yielding). However, for the same tensile stress applied in the T-direction, yielding is expected, where the largest circle on the Mohr's circle diagram (after stress state superposition) is tangent to the line marked by τ_c. Thus, the essence of the cross-softening effect in DP steels is predicted by this simplified treatment. The applied tensile stress in the L-direction would need to be increased significantly for the yielding criterion to be met (*i.e.*, such that $\tau_{max} = \tau_c$).

A similar analysis is shown for the case of PS prestrain in Figure 84A for L-direction tension (tension axis in principal direction 1) and in Figure 84B for T-direction tension (tension axis in principal direction 2). The same conclusion is reached, as for UT prestrain condition, where a cross-softening effect is predicted, albeit smaller than that predicted for the UT prestrain condition. In contrasting Figure 83A [L-direction tension after UT prestrain ($\varepsilon_{maj} = \varepsilon_1 = \varepsilon_L$)] and Figure 84A [L-direction tension after PS prestrain ($\varepsilon_{maj} = \varepsilon_1 = \varepsilon_L$)], the maximum shear stress (top of largest circle on the Mohr's circle diagram, after superposition) is greater for the latter case. Hence the L-direction tensile yield stress after PS prestrain would be lower than that after UT prestrain (assuming τ_c is the same for both prestrain conditions). Following a similar argument (contrasting Figure 83B and Figure 84B) it is expected that the T-direction yield stress after PS prestrain would be higher than that after UT prestrain. It appears that, as the minor strain ($\varepsilon_{min} = \varepsilon_2 = \varepsilon_T$) of the prestrain mode increases, the L-direction post-forming tensile yield stress decreases while that in the T-direction increases (again, it is assumed for this exercise, that τ_c is the same for all prestrain conditions).

For the BB prestrain condition (Figure 85), the superposition of deformation-induced residual stresses and applied tension predicts isotropic hardening in the context of the post-forming tensile yield strength. As the prestrain mode exhibits planar symmetry, it follows that the post-forming tensile response is symmetric.

The results of the preceding simplified analysis of the effects of prestrain mode on post-forming residual stress distributions and the stress state superposition exercise are consistent with the observations of differential hardening for the DP steel (see Figure 68 through Figure 70). In the next section, the expected relationship between deformation-induced residual stresses and post-forming tensile yield strength will be examined more closely.

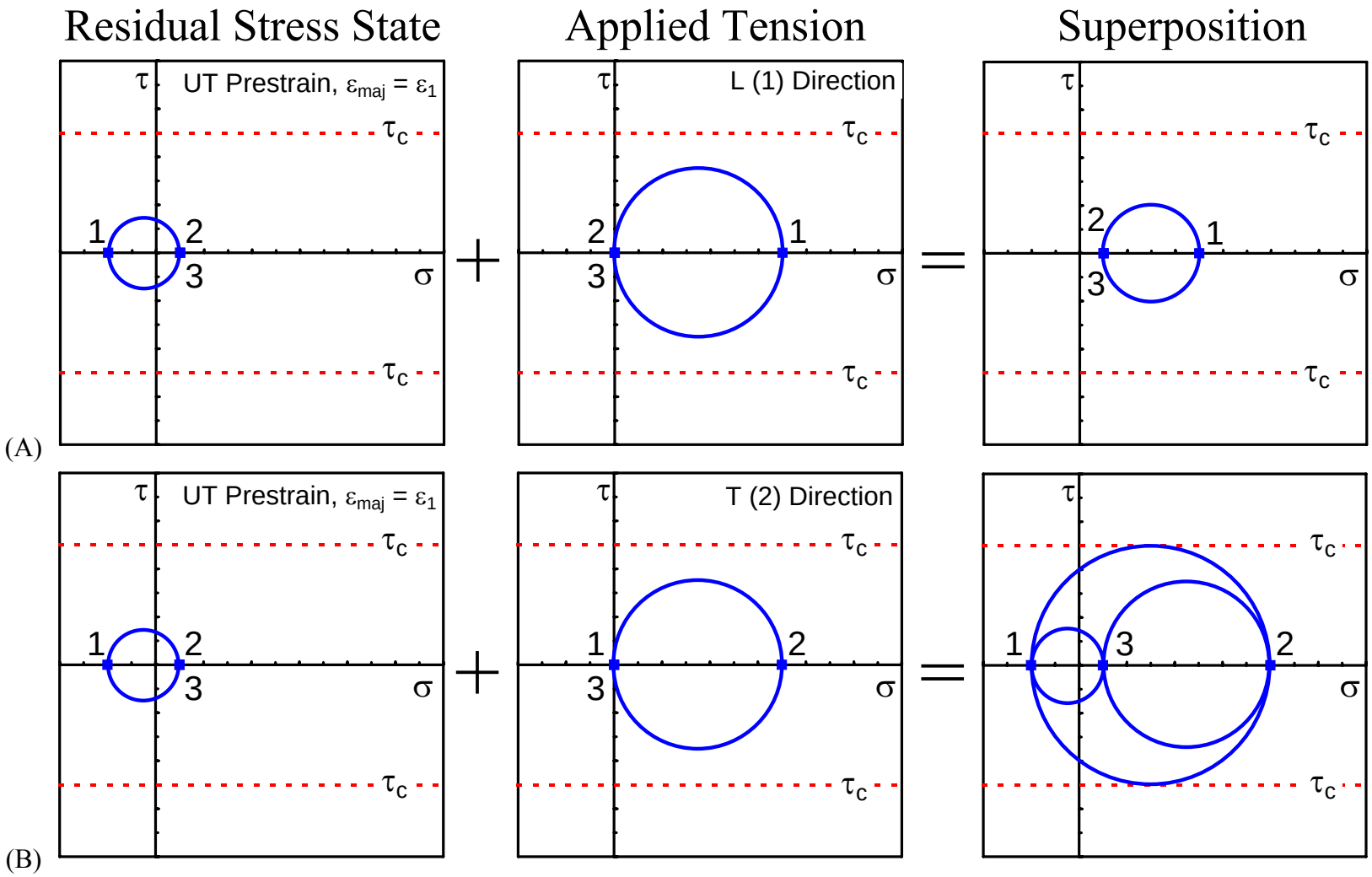

Figure 83: Superposition of applied tension and residual stress states for (A) uniaxial tension prestrain followed by uniaxial tension in the longitudinal direction ($< 2\tau_c$), and (B) uniaxial tension prestrain followed by uniaxial tension in the T direction ($< 2\tau_c$). [1 = longitudinal (L) direction; 2 = transverse (T) direction; and 3 = thickness direction.]

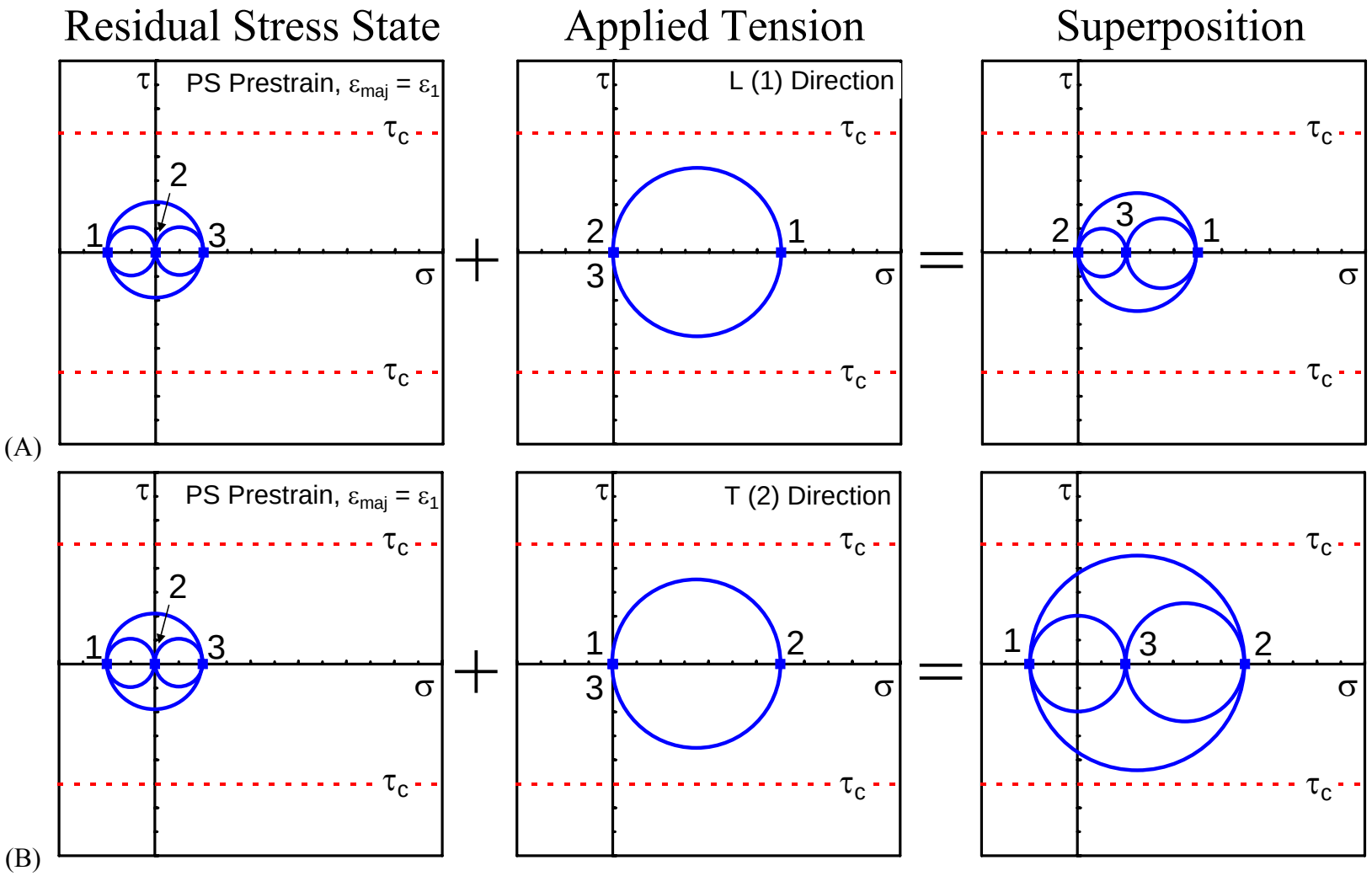

Figure 84: Superposition of applied tension and residual stress states for (A) plane strain prestrain followed by uniaxial tension in the longitudinal direction ($< 2\tau_c$), and (B) plane strain prestrain followed by uniaxial tension in the T direction ($< 2\tau_c$). [1 = longitudinal (L) direction; 2 = transverse (T) direction; and 3 = thickness direction.]

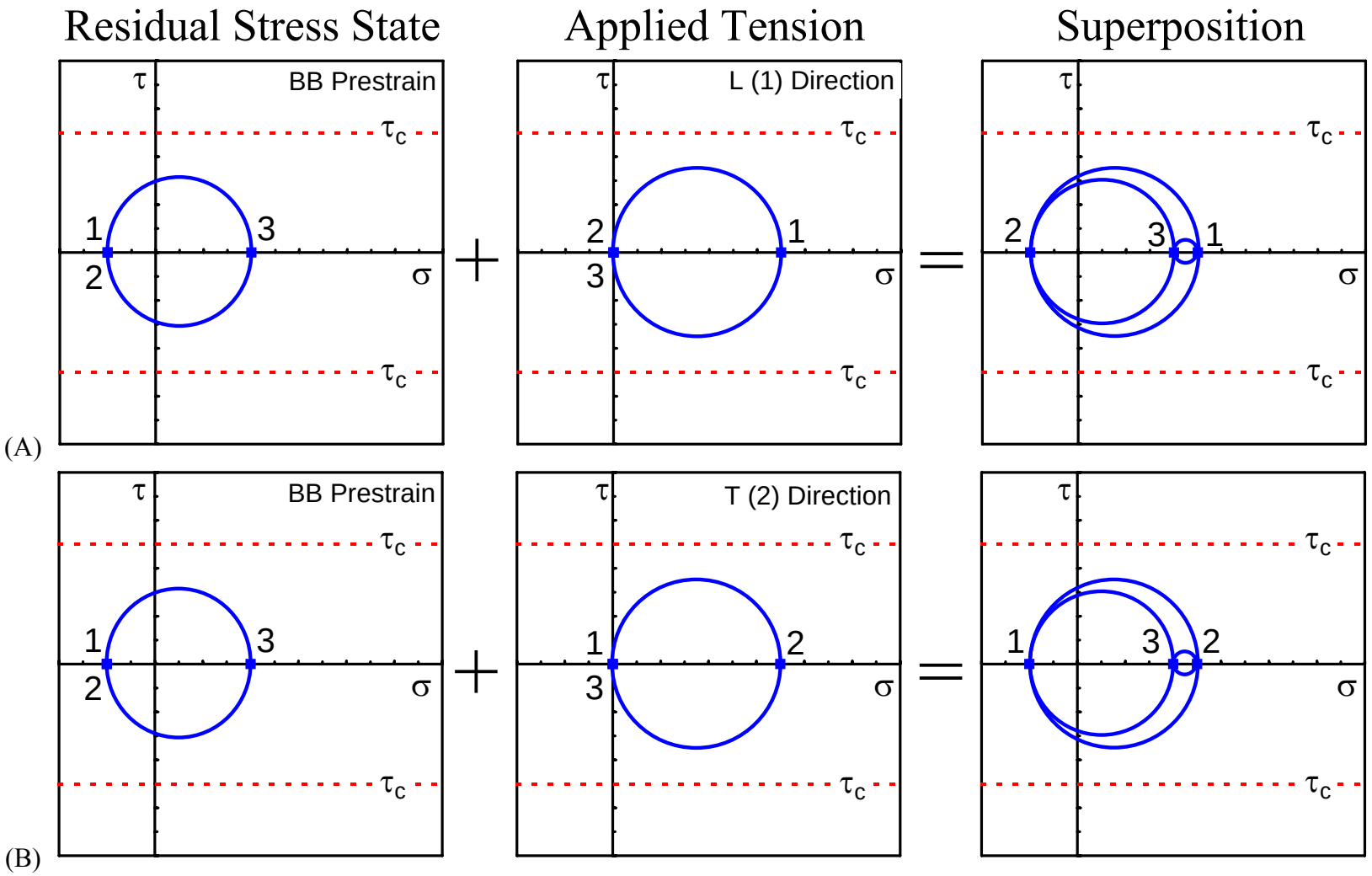

Figure 85: Superposition of applied tension and residual stress states for (A) balanced biaxial prestrain followed by uniaxial tension in the longitudinal direction ($< 2\tau_c$), and (B) balanced biaxial prestrain followed by uniaxial tension in the T direction ($< 2\tau_c$). [1 = longitudinal (L) direction; 2 = transverse (T) direction; and 3 = thickness direction.]

6.2.3 **Prestrain-Induced Residual Stresses and Differential Hardening**

Recall the maximum shear stress (Tresca) yield criterion (discussed in Section 5.2), where

$$\sigma_{max} - \sigma_{min} = 2\tau_c . \qquad [36]$$

Clearly, in order to predict yielding, by this or any other similar yield criterion, knowledge of the critical shear stress, τ_c, is essential. In simple cases such as non-previously-deformed, isotropic materials, such knowledge becomes readily available simply by doing a tensile test, where the measured yield strength in tension is equal to twice the critical shear stress (Equation 26). However, once a material is deformed, the critical shear stress changes as the material undergoes work hardening. The evolution of the critical shear stress with deformation along various strain paths may be estimated by measuring the stress/strain response in tension and extrapolating the behavior, with consideration of effective stress and effective strain, to other modes of deformation (also discussed in Section 5.2). However, with effects such as latent work hardening, the Bauschinger Effect and deformation-induced residual stresses, precise determination of the critical shear stress becomes increasingly dubious in situations involving significant deformation along complex strain paths (84). In the presence of a triaxial deformation-induced residual stress distribution, it is a non-trivial task to predict the post-forming tensile yield strength, for example. With a few simplifying assumptions, however, the *difference* in the tensile yield strength (*i.e.*, differential hardening) between two principal directions may be estimated if knowledge of the prestrain-induced residual stress distribution is known, as discussed below.

With the convention that principal direction 1 is the longitudinal (L) direction (rolling direction); principal direction 2 is the transverse (T) direction; and principal direction 3 is the sheet thickness direction, the following two expressions follow from the Tresca yield criterion and the principle of superposition:

$$\left(YS_L - \sigma_{dr,1}\right) - \min\left(\sigma_{dr,2}, \sigma_{dr,3}\right) = 2\tau_c \text{, and} \quad [37a]$$

$$\left(YS_T - \sigma_{dr,2}\right) - \min\left(\sigma_{dr,1}, \sigma_{dr,3}\right) = 2\tau_c \text{,} \quad [37b]$$

where YS_L and YS_T are the measured (applied) tensile yield stresses in the L-direction and in the T-direction, respectively, and $\sigma_{dr,1}$, $\sigma_{dr,2}$ and $\sigma_{dr,3}$ are the principal components of $\sigma_{dr,ij}$. The expression "min(A, B)" means the minimum value between principal residual stress components A and B. In Equation 37a, $(YS_L - \sigma_{dr,1})$ is σ_{max} at yielding during an L-direction tensile test (see Equation 36). Similarly, in Equation 37b, $(YS_T - \sigma_{dr,2})$ is σ_{max} at yielding during a T-direction tensile test. So, with no specific knowledge of the critical shear stress, τ_c, for a general prestrained condition, Equation 37 results in two equations with three unknowns (*i.e.*, YS_L, YS_T and τ_c). However, as the *difference* in tensile yield strength in the L-direction and the T-direction is of interest here, Equations 37a and 37b may be combined to get

$$\Delta YS = YS_T - YS_L = \sigma_{dr,1} - \sigma_{dr,2} + \min\left(\sigma_{dr,1}, \sigma_{dr,3}\right) - \min\left(\sigma_{dr,2}, \sigma_{dr,3}\right), \quad [38]$$

where ΔYS is the difference between the tensile yield strength in the T-direction and in the L-direction. So, with this convention, $\Delta YS > 0$ means cross-hardening, while $\Delta YS < 0$ means cross-softening. In formulating Equation 38, it was assumed that, in the absence of a deformation-induced residual stress distribution, the material is isotropic (no crystallographic texture effects, for example). It was also assumed that the only source of post-forming

anisotropy is a distribution of deformation-induced residual stresses (no latent work hardening, for example).

If the hypothetical deformation-induced residual stress distributions of Figure 82 are assumed, estimations of differential hardening (ΔYS) can be made. For example, the hypothetical UT prestrain condition (β = -0.5) has the following principal components of deformation induced residual stress: $\sigma_{dr,1}$ = -100 MPa, $\sigma_{dr,2} = \sigma_{dr,3}$ = 50 MPa. Inserting these values into Equation 38 gives ΔYS = (-100) – 50 – 50 + (-100) = -300 MPa (strong cross-softening effect). Similarly, for the PS prestrain condition, ΔYS = -200 MPa (milder, yet significant cross-softening effect), and for the BB prestrain condition, ΔYS = 0 (isotropic hardening). The predicted influence of prestrain path on differential hardening behavior is shown in Figure 86. In this figure, a critical shear stress of 250 MPa is assumed for each prestrain condition, for illustrative purposes. As discussed above in Section 6.2.2, the magnitude of the cross-softening effect in DP steels is expected to decrease and approach isotropic hardening as the surface strain ratio, β, increases.

6.3 IMPLICATIONS OF NEUTRON DIFFRACTION RESULTS

In this section, the calculated deformation-induced residual stresses, based on neutron diffraction data (Section 5.5.2) are directly related to the post-forming tensile yield behavior of prestrained samples of IF steel, HSLA steel and DP steel. Specifically, the 5% major strain condition ($\varepsilon_{maj} = \varepsilon_L$ = 0.05) is considered for the prestrain modes of uniaxial tension (UT), plane strain (PS) and balanced biaxial stretching (BB).

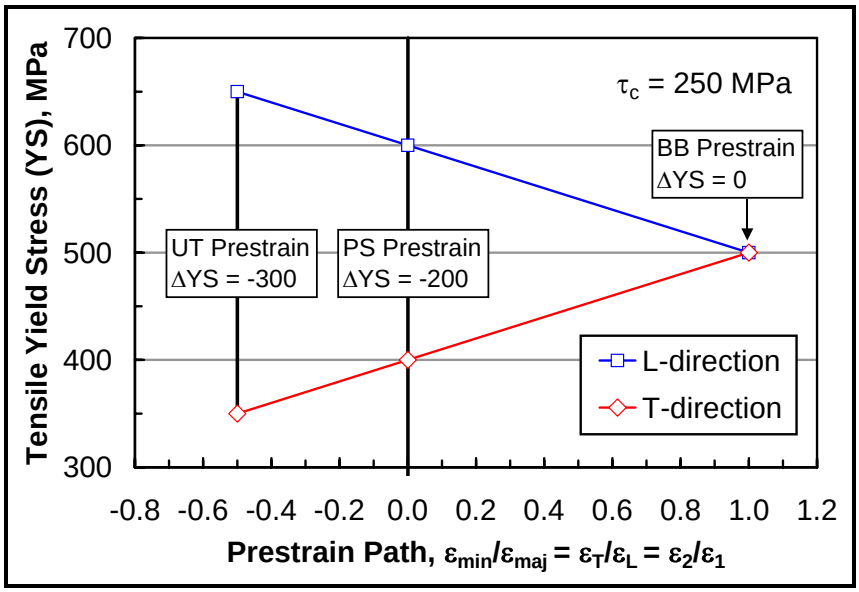

Figure 86: Schematic illustration of the influence of prestrain path on the post-forming tensile yield strength (YS) of a dual-phase steel. A critical shear stress, τ_c, of 250 MPa and the hypothetical residual stress distributions shown in Figure 82 are assumed.

6.3.1 **Predicted Differential Hardening Based on Diffraction Data**

The deviatoric components, $\sigma'_{dr,ij}$, of the calculated deformation-induced residual stresses (shown in Figure 75) were entered into Equation 38 to predict the differential hardening behavior (ΔYS) for each prestrain condition listed in Table XI. For this portion of the analysis, recall that the average values based on {200} and {211} reflections were used for the residual stress calculations (see Section 5.5.2). To account for the large concentration of martensite (0.15 volume fraction—see Section 5.1.1) the deformation-induced residual stress components were multiplied by 0.85 for the DP steel, as the measured stresses pertain only to the ferrite phase. The predicted differential hardening behavior, based on neutron diffraction residual stress measurements, is summarized in Figure 87. For all materials in the 5% prestrain condition (UT, PS and BB prestrain modes), the predicted differential hardening response (ΔYS) increases as β increases (as the minor strain increases), as predicted in Section 6.2.3.

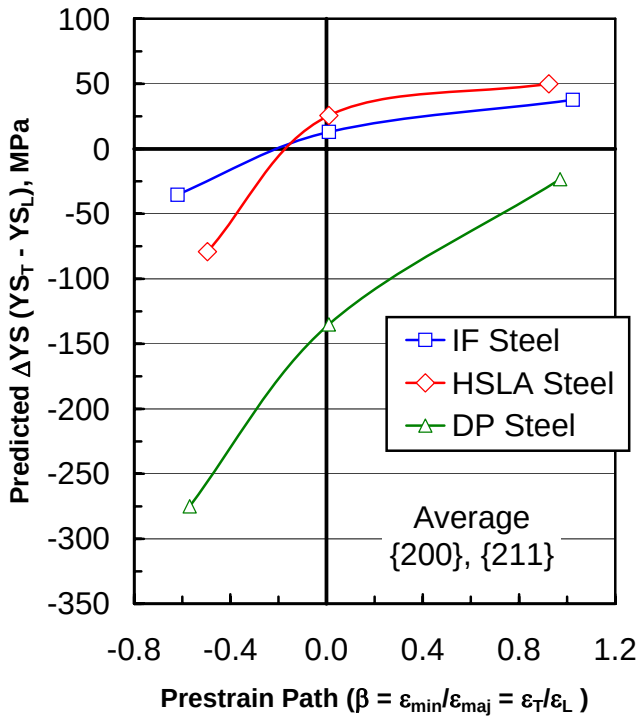

Figure 87: Predicted differential hardening behavior for various prestrain modes ($\varepsilon_{maj} = \varepsilon_L = 0.05$). Predictions are based on deformation-induced residual stress calculations that are based on neutron diffraction measurements. See text for details of the analysis.

For the UT prestrain condition ($\beta \sim -0.5$), negative differential hardening (cross-softening) is predicted for the IF steel, the HSLA steel, and the DP steel. The DP steel is expected to exhibit the largest cross-softening effect (as was shown experimentally in Section 5.4.4). For the IF steel and the HSLA steel, nearly isotropic hardening (based on the 0.2 % offset flow stress, $\sigma_{0.2\%OFS}$) or even a mild cross-hardening response (based on the flow stress at 1% tensile elongation, $\sigma_{1\%FS}$) was observed experimentally for the UT prestrain mode (see Figure 68). Recall the unique and unexpected initial cross-softening effect (immediately after yielding) exhibited by the IF steel and the HSLA steel for the UT prestrain condition (see Figure 79A). It appears that this behavior is reflected in the neutron diffraction measurements, and that the initial post-forming tensile yielding behavior (*i.e.*, at very low tensile strains) is strongly influenced by

residual stresses induced by prestraining. An alternate way to characterize the initial yielding behavior, in light of this observation, is discussed in 6.3.2 below.

For the PS prestrain condition ($\beta \sim 0$ in Figure 87) it is predicted that the IF steel and the HSLA steel exhibit a mild cross-hardening effect and that the DP steel exhibits a significant cross-softening response (albeit smaller than that predicted for the UT prestrain condition)—consistent with experimental observations (see Figure 69).

For the BB prestrain condition ($\beta \sim 1$ in Figure 87) a cross-hardening response is predicted for the IF steel and the HSLA steel (larger than that predicted for the PS prestrain condition) and a small cross-softening response is predicted for the DP steel. These observations generally conflict with experimental observations for the IF steel and the DP steel, where the post-forming tensile response after BB prestrain is generally isotropic ($\Delta YS \sim 0$, see Figure 70). The experimentally observed cross-hardening response of the HSLA steel, for the BB prestrain mode, was attributed to larger intrinsic anisotropy (Table VII). The correlation between predicted and experimental differential hardening behavior is discussed in further detail in Section 6.3.3.

6.3.2 **Various Measures of Tensile Yield Stress**

In Section 6.1.4 through 6.1.6, the post-forming tensile yielding behavior was discussed. It was recognized that, depending upon the method used to measure the yield strength, different conclusions might be reached when assessing the relative intensities of the various differential hardening effects observed in this analysis. Figure 79A (UT prestrain condition, $\varepsilon_{maj} = \varepsilon_L = 0.05$) gives the clearest example, where, for the IF steel and the HSLA steel, one might measure a cross-softening response (at very low tensile strains—immediately after yielding); or an isotropic

hardening response (when the 0.2% offset flow stress is considered); or a mild cross-hardening response (when the flow stress at 1% tensile strain is considered). For the DP steel, the cross-softening response is very large initially (a few hundred MPa, by inspection), but diminishes very quickly as tensile deformation continues. It is recognized that an alternate measure of "yield strength" is needed to account for the very-low-strain differential hardening effects that may be overlooked by conventional measures of "yield strength".

In evaluating and assessing the connection between prestrain-induced residual stresses and the post-forming tensile yielding response, it is important to consider the flow behavior *immediately* after yielding for the following two reasons: 1) as tensile deformation continues beyond yielding, the residual stress distributions induced during prestraining are likely disturbed, and other internal stress distributions develop as a result of the tensile deformation (see discussion in Section 6.1.4), and 2) other competing phenomena such as latent work hardening are manifested by dislocation interactions and become more prominent as deformation continues—thereby obscuring the connection between the measured post-forming tensile response and the measured residual stresses induced by prestrain (see discussion in Section 5.4.4).

As an alternative measure of tensile yield strength, the flow stress at a specified tangent modulus value (the instantaneous slope of the stress/strain curve) may be used to reflect the transition from elastic deformation to plastic deformation in cases of continuous yielding. As an example for the DP steel, the post-forming L-direction and T-direction tensile s/e curves from Figure 79A (UT prestrain condition: $\varepsilon_{maj} = \varepsilon_L = 0.05$) are re-plotted in Figure 88, where various ways to measure differential hardening ($\Delta YS = YS_T - YS_L$) are shown. Figure 88A shows ΔYS based on the 1% tensile flow stress ($\sigma_{1\%FS}$), where ΔYS ($\Delta\sigma_{1\%FS}$) = -80 MPa—a significant

cross-softening effect. A substantially larger cross-softening effect is measured (Figure 88B) when ΔYS is based on the 0.2% offset flow stress ($\sigma_{0.2\%OFS}$), where ΔYS ($\Delta\sigma_{0.2\%OFS}$) = -189 MPa. However, it appears that the cross-softening effect, at very low strains (*immediately* after yielding) is even larger than that determined by $\Delta\sigma_{0.2\%OFS}$. Because of the gradual, continuous transition from elastic deformation to plastic deformation, it is difficult to define the precise stress value that defines "yielding". As such, the stress value that corresponds to a tangent modulus (TM) value of 100 GPa (half of the bulk Young's modulus) was arbitrarily chosen to reflect the very-low-strain elastic-to-plastic transition in the post-forming tensile stress/strain curves. This alternate definition of "yield stress" is called $\sigma_{TM=100}$, and $\Delta\sigma_{TM=100}$ is the difference between the T-direction and L-direction tensile flow stresses at TM = 100 GPa. Thus, $\Delta\sigma_{TM=100}$ is a truer reflection of the initial differential hardening response at very low strains and is expected to relate more directly to the measured residual stress distributions in the prestrained samples. Figure 88C shows how $\Delta\sigma_{TM=100}$ is calculated, where ΔYS = $\Delta\sigma_{TM=100}$ = -250 MPa in this example. In the following section, the predicted differential hardening behavior, based on the neutron diffraction residual stress measurements (Figure 87), is compared to the experimentally determined ΔYS values based on $\Delta\sigma_{1\%FS}$, $\Delta\sigma_{0.2\%OFS}$, and $\Delta\sigma_{TM=100}$.

6.3.3 **Predicted vs. Experimental Differential Hardening**

The experimental differential hardening behavior (UT, PS and BB prestrain modes: $\varepsilon_{maj} = \varepsilon_L$ = 0.05) is shown in contrast to the predicted behavior (based on neutron diffraction data) in Figure 89 (a separate plot for the IF steel, the HSLA steel and the DP steel). For each material, the predicted ΔYS values from Figure 87 are shown along with the experimental ΔYS values based on $\sigma_{1\%FS}$, $\sigma_{0.2\%OFS}$, and $\sigma_{TM=100}$ (see section 6.3.2 above for explanation of these terms).

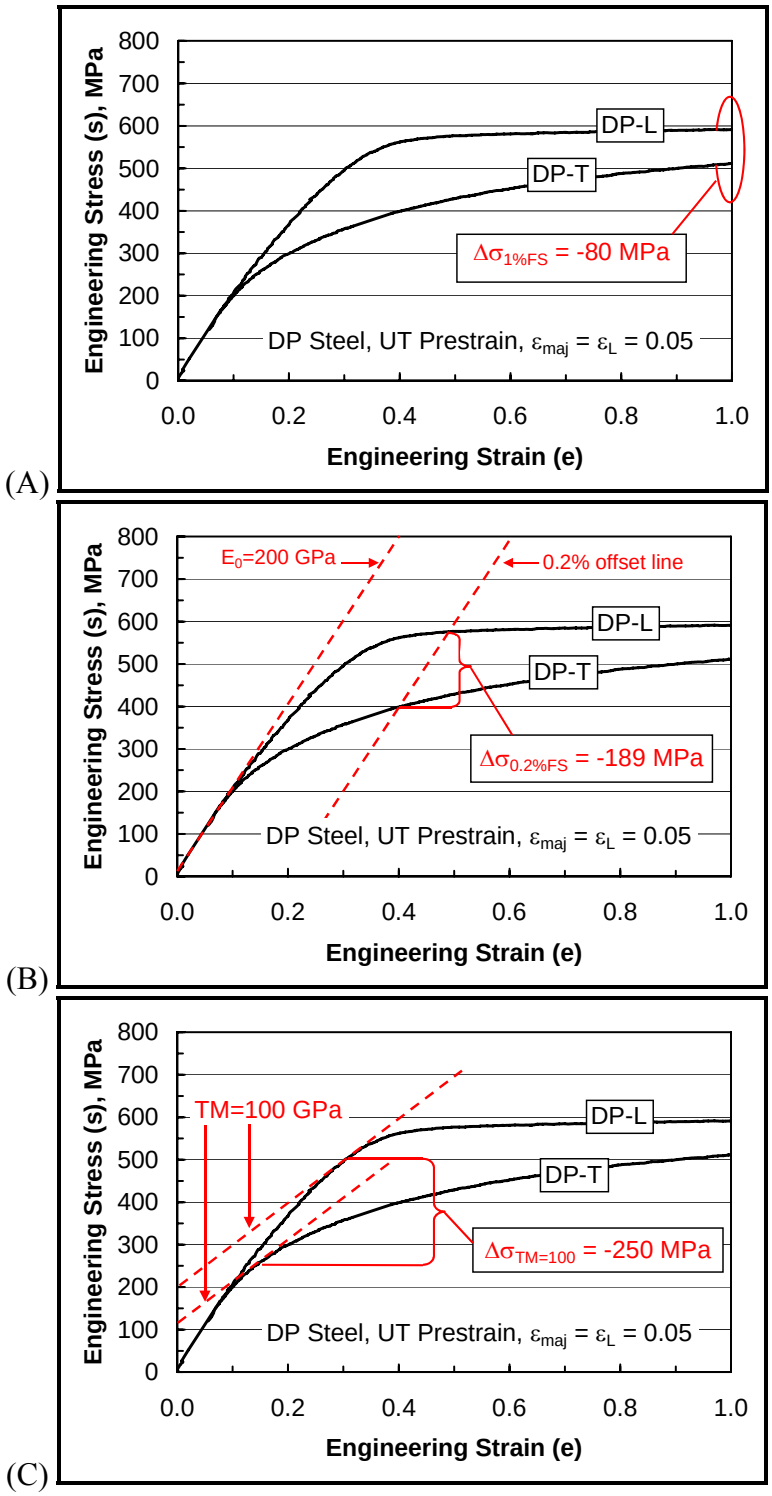

Figure 88: Various ways to measure differential hardening ($\Delta YS = YS_T - YS_L$)—(A) $\Delta\sigma_{1\%FS}$, (B) $\Delta\sigma_{0.2\%OFS}$, and (C) $\Delta\sigma_{TM=100}$. Here, the DP steel prestrained in uniaxial tension ($\varepsilon_{maj} = \varepsilon_L = 0.05$) is used as an example (see Figure 79A).

(A)

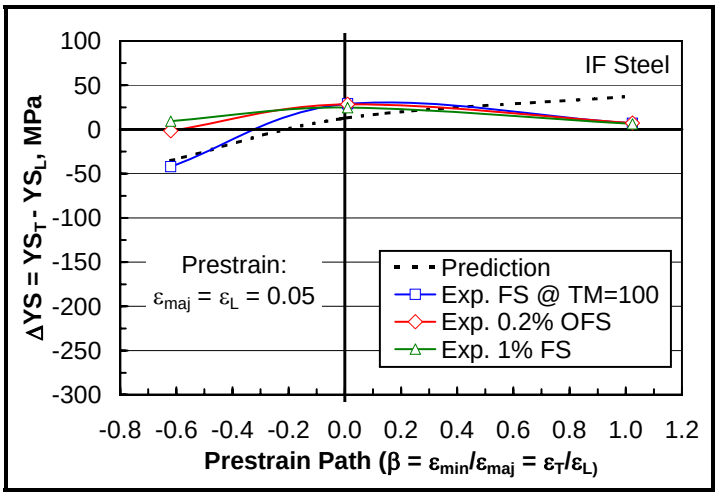

(B)

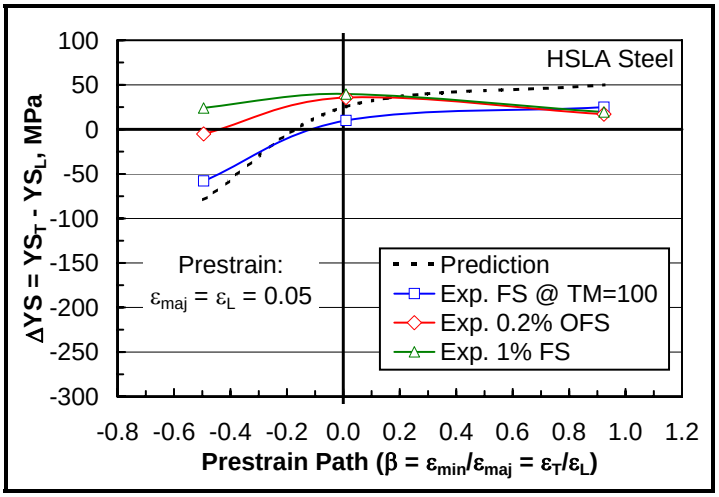

(C)

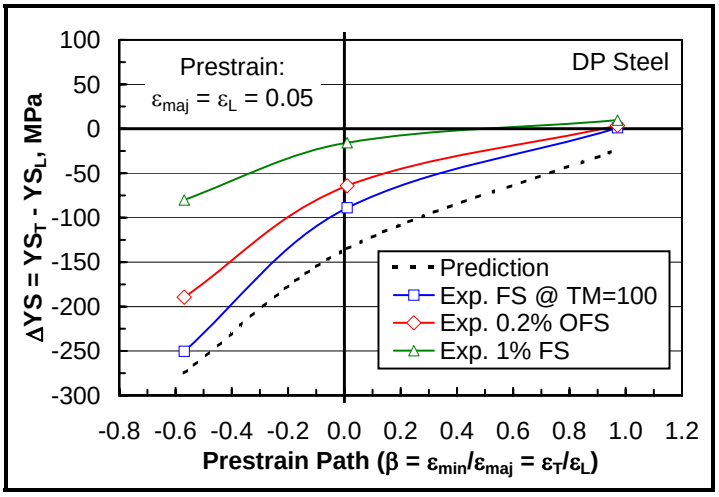

Figure 89: Predicted and experimentally measured differential hardening for (A) IF steel, (B) HSLA steel and (C) DP steel. The predictions are those shown in Figure 87 (based on neutron diffraction data), and the various measures of differential hardening are illustrated in Figure 88.

For the IF steel (Figure 89A) and the HSLA steel (Figure 89B), nearly identical relationships are shown. For the UT prestrain condition ($\beta \sim -0.5$), $\Delta\sigma_{TM=100}$ (negative) < $\Delta\sigma_{0.2\%OFS}$ (~ 0) < $\Delta\sigma_{1\%FS}$ (positive), and the predicted ΔYS value (dashed curve) corresponds most closely to $\Delta\sigma_{TM=100}$ (recall the complex post-forming tensile yielding behavior of the IF steel and the HSLA steel for the UT prestrain condition: Figure 79A). For the PS prestrain condition ($\beta \sim 0$), ΔYS depends much less on the choice of yield strength measurement than in the UT prestrain case. For the PS prestrain condition, the deformation-induced residual stress distribution is expected to contribute very little to the overall differential hardening response of the IF and HSLA steels (the predicted ΔYS value, based on neutron diffraction, is effectively zero). The differential hardening behavior is dominated by latent work hardening for the PS prestrain condition (not reflected in the residual stress measurements). For the BB prestrain condition, the neutron diffraction based predictions of ΔYS tend to overestimate the experimental values by about 30 MPa. Considering the assumptions made (*e.g.*, Tresca yield criterion, superposition of residual and applied stress states, isotropic materials) and the arbitrariness of $\sigma_{TM=100}$ as a measure of the initial flow stress, the agreement between the predicted ΔYS values and the experimentally determined $\Delta\sigma_{TM=100}$ values for the IF steel and the HSLA steel is very encouraging. Although the deformation-induced residual stresses are small in comparison to those measured for the DP steel, the trends in differential hardening behavior, with respect to prestrain mode, are satisfactorily predicted by the neutron-diffraction based post-forming residual stress measurements.

For the DP steel (Figure 89C), the predicted trends in differential hardening, with respect to overall prestrain mode effects, are again in satisfactory agreement with experimental values. It is also clear that the experimental ΔYS value depends very strongly on the choice of

yield strength parameter, and that $\Delta\sigma_{TM=100}$ generally correlates best to the predicted values. The very large initial cross-softening effects (negative $\Delta\sigma_{TM=100}$ values) for the UT and PS prestrain conditions, and the isotropic hardening response for the BB prestrain condition, are predicted to within 50 MPa by use of Equation 38 ($YS_L = \sigma_{TM=100,L}$ and $YS_T = \sigma_{TM=100,T}$). Again, these results are extremely encouraging, as the large deformation-induced mechanical anisotropy of DP steels has been directly related to measured deformation-induced residual stresses for the first time. It is also now understood how residual stresses affect post-forming tensile behavior in DP steels (and to a lesser extent, in convention single phase steels). Prestrain induced residual stresses affect primarily the initial tensile yielding behavior and diminish as tensile deformation progresses and other mechanisms (*e.g.*, latent work hardening) become more important. It appears that the deformation-induced residual stresses in the DP steel are of such large magnitude (in contrast to the IF steel and the HSLA steel) that the effects of latent work hardening (*e.g.*, cross-hardening and the associated Type 2 tensile stress/strain behavior) are masked.

As discussed in Section 5.5.2, the average deformation-induced residual stress measurements (*i.e.*, the average values given by the {200} and {211} reflections) were considered throughout the discussion for clarity (see Figure 75, Figure 87 and Figure 89). In reviewing Table IX and Table X, there are, in some instances, significant differences between the calculated deviatoric residual stress components ($\sigma'_{dr,ij}$) based on {200} reflections and those based on {211} reflections. In Figure 90 through Figure 92, the experimental $\Delta\sigma_{TM=100}$ values are re-plotted along with the predicted values of ΔYS based on neutron diffraction data, for each material (IF steel: Figure 90; HSLA steel: Figure 91; and DP steel Figure 92). Included in each figure are the average {200}/{211} predictions (shown earlier) along with the individual

predictions based on {200} and {211} reflections (dashed curves). The separation between the individual {200} and {211} prediction curves attests to the uncertainty of the residual stress measurements as they are applicable to the bulk behavior of the materials. The predicted ΔYS values based on {200} reflection data are consistently higher than the corresponding predictions based on {211} reflections. This occurrence may be related, in part, to the choice of diffraction elastic constants used in Equation 22 to calculate residual stresses (Section 4.4.3). Considering the uncertainty related to the type of reflection used for the residual stress measurements, the measured $\Delta\sigma_{TM=100}$ values are within 25 MPa of the "nearest" predicted value (either based on {200} or {211} reflection data) for each material in each prestrain condition.

Van Houtte *et al*. (67) made the astute and seemingly inarguable observation that, for prediction of deformation behavior in complex (changing) strain paths, a crystallographic texture-based (anisotropic) yield criterion must be used that also takes the effect of dislocation substructure development on work hardening (and work softening) into account. Based on the results of this research program, it is clear that deformation-induced residual stresses must also be included in any appropriate, advanced material deformation model. This assessment is especially true for DP steels (and likely for other multiphase steels). The aforementioned texture and substructure development effects are seemingly overshadowed in DP steels by the effects of deformation-induced residual stresses. For the conventional steels considered in this analysis (the IF steel and the HSLA steel), the measured deformation-induced residual stresses, and their associated effects on post-forming tensile behavior are relatively small in magnitude, albeit measurable. It seems that, for these materials, residual stresses induced by prestrain only affect the initial yielding response (at very low plastic strains) during subsequent deformation, and that the overall strength evolution and residual ductility are dominated by other factors.

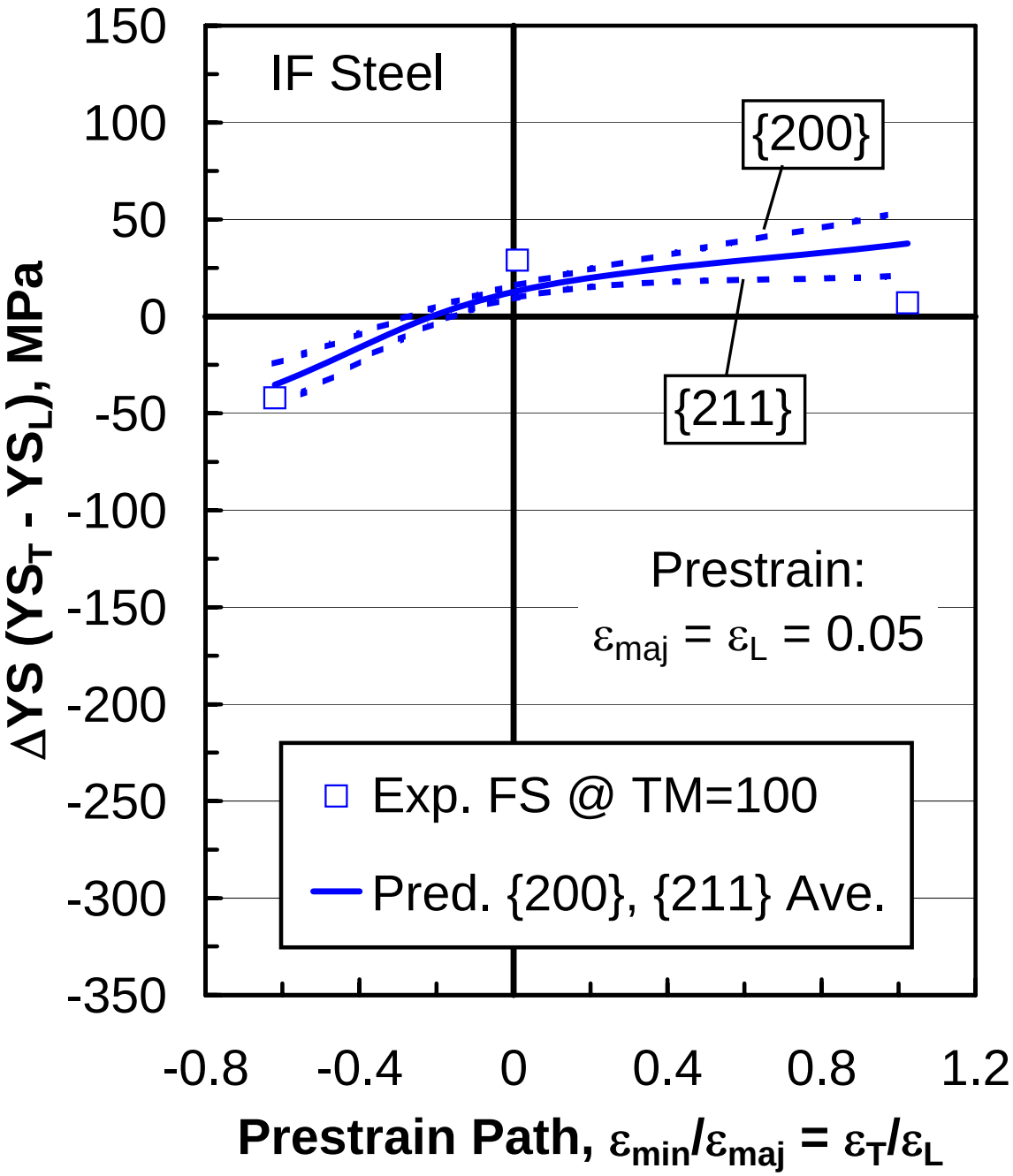

Figure 90: Predicted and experimentally determined differential hardening ($\Delta\sigma_{TM=100}$) for various prestrain modes (IF steel, $\varepsilon_{maj} = \varepsilon_L = 0.05$). Here, the individual {200} and {211} predictions are shown by dashed curves as indicated, and the average values (from Figure 87 and Figure 89A) are shown by the continuous curve.

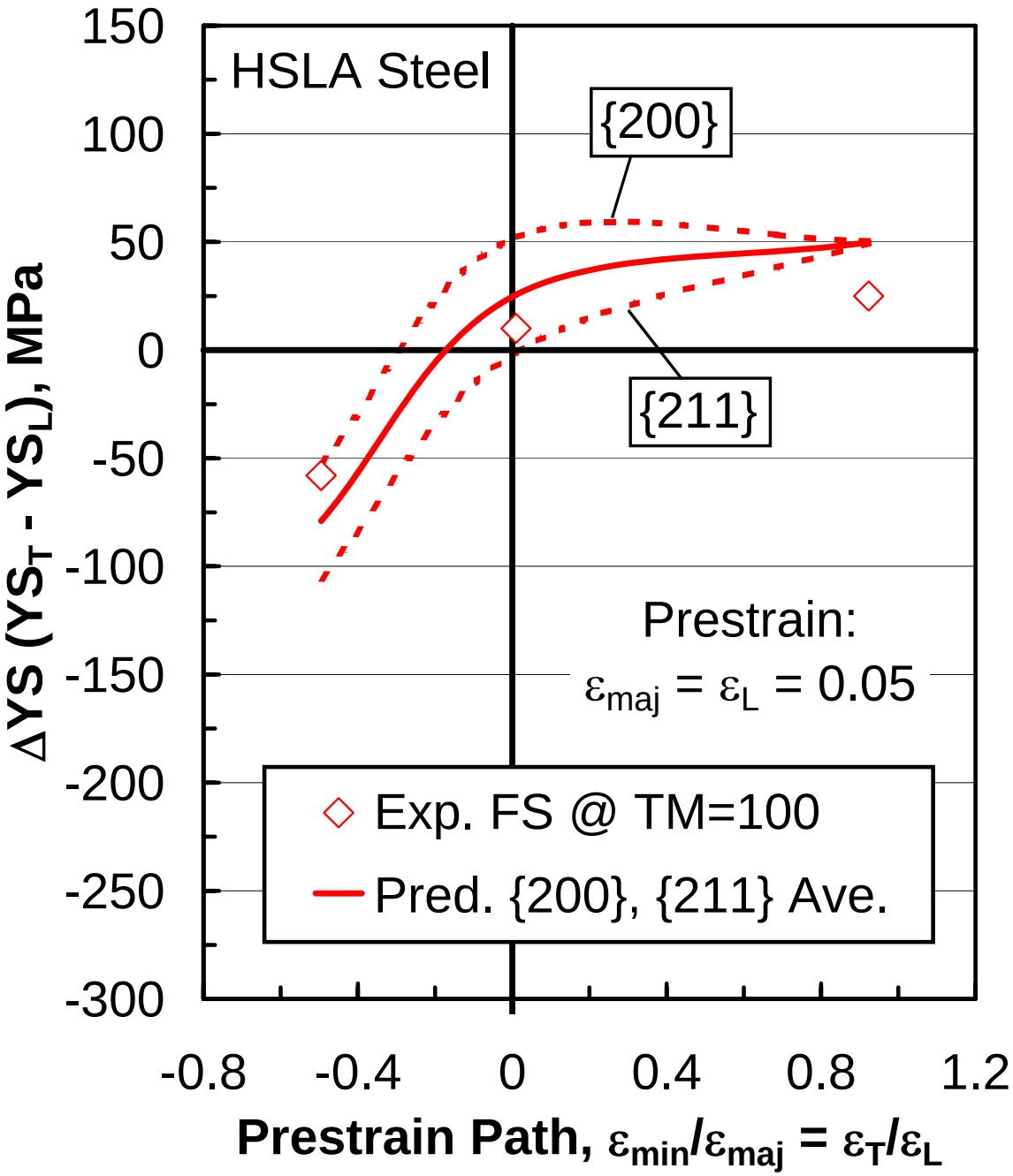

Figure 91: Predicted and experimentally determined differential hardening ($\Delta\sigma_{TM=100}$) for various prestrain modes (HSLA steel, $\varepsilon_{maj} = \varepsilon_L = 0.05$). Here, the individual {200} and {211} predictions are shown by dashed curves as indicated, and the average values (from Figure 87 and Figure 89B) are shown by the continuous curve.

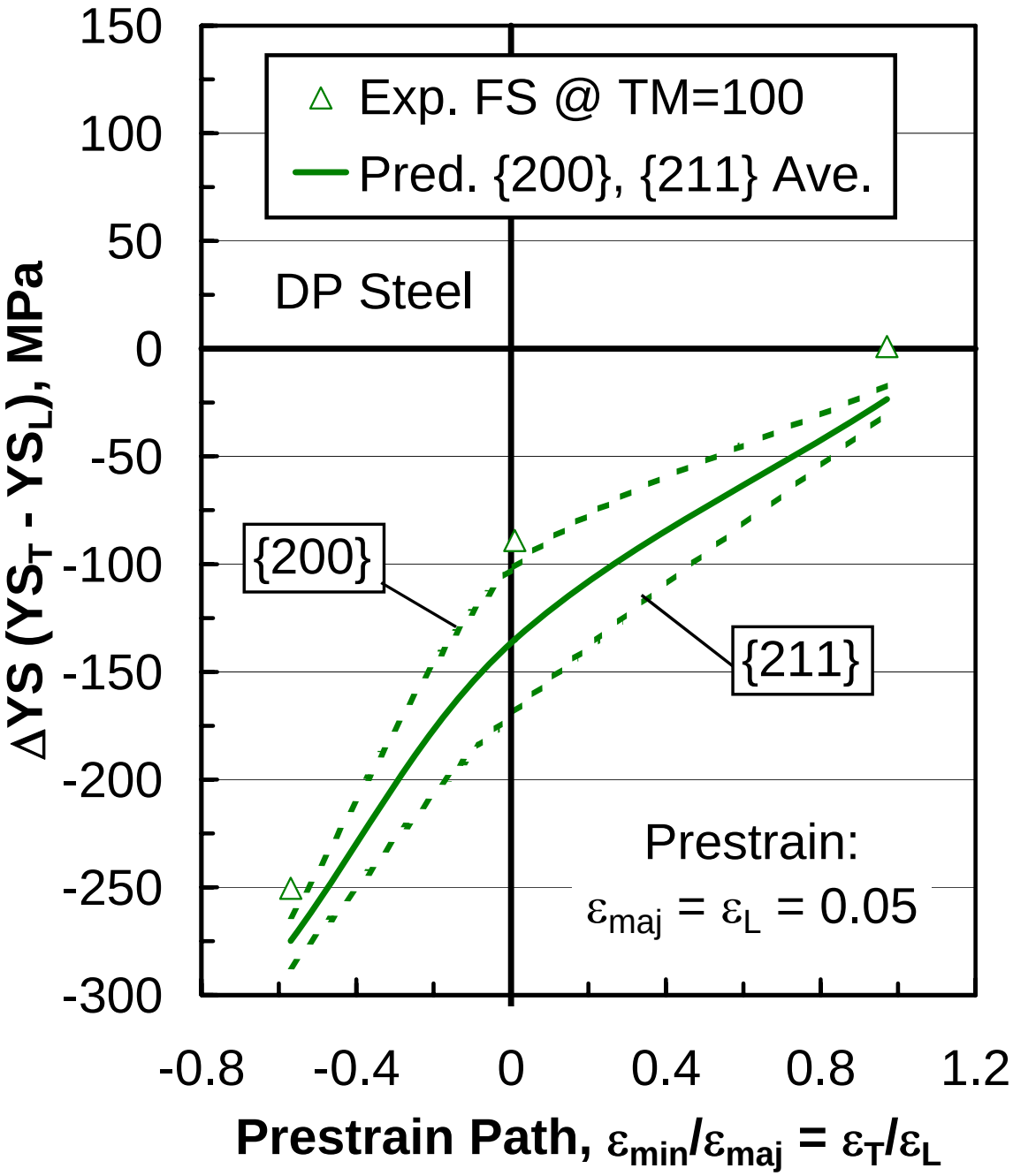

Figure 92: Predicted and experimentally determined differential hardening ($\Delta\sigma_{TM=100}$) for various prestrain modes (DP steel, $\varepsilon_{maj} = \varepsilon_L = 0.05$). Here, the individual {200} and {211} predictions are shown by dashed curves as indicated, and the average values (from Figure 87 and Figure 89C) are shown by the continuous curve.

As an extension of this research program, it would be appropriate to consider the statistically preferred ferrite crystallographic orientation (*i.e.*, orientation distribution function, ODF) of the DP steel. In conjunction with grain size and grain shape distributions for the various textural components (such as those obtainable by electron back-scattered diffraction techniques), one could conceivably determine the most appropriate {hkl} reflections to use for calculating deformation-induced residual stresses over the bulk of the deformed sample. In other words, with a complete knowledge of deformation texture and grain size/shape distributions in a prestrained DP steel, an abundance algorithm could be applied to the individual residual stress values determined by various {hkl} reflections. Additionally, with greater knowledge of crystallographic texture (annealing texture and deformation texture), intrinsic mechanical anisotropy could be factored into the relationship between deformation-induced residual stresses and post-forming tensile stress strain behavior.

6.4 PRACTICAL CONSIDERATIONS

The findings of this research program bear several implications toward the practical application of DP steels in terms of formability, manufacturability, and in-service performance. Each of these aspects is addressed separately in the following sections (Sections 6.4.1 through 6.4.3).

6.4.1 **Formability**

The enhanced work hardening behavior and excellent formability of DP steels have been known since the earliest references to these unique materials were made (Section 2.1.2). The analysis of post-forming residual tensile ductility for the IF steel, the HSLA steel, and the DP steel (Section 5.3) suggests a potential advantage of DP steels in complex strain paths where abrupt strain path

changes occur. In cases of orthogonal strain path changes (*i.e.*, the major strain direction of the prestrain path is perpendicular to the major strain direction of the secondary strain path), the most severe reductions in post-forming tensile ductility were observed for the IF steel and the HSLA steel. Such orthogonal strain path changes have very little effect on the residual tensile ductility of DP steels. It is anticipated that DP steels are particularly well suited for sequential multi-stage forming operations—such as tube hydroforming—where strain path changes are inherent to the process. The enhanced post-forming ductility (formability) of DP steels likely will improve design flexibility where, otherwise, design limits are dictated by the deterioration of formability in complex strain modes. A particularly important and natural extension of this research program would focus on the specific strain modes associated with the various stages of tube hydroforming such as tube making, pre-bending, and hydroforming (with and without end feeding) (90).

6.4.2 **Manufacturability**

With the increasing application of DP steels in the automotive sector, springback and springback variability awareness have heightened throughout the industry. Much attention has recently been focused on predicting, controlling and reducing springback (and springback variability) in high strength steel forming applications. The significant deformation-induced residual stresses measured in the DP steel (and to a lesser extent in the IF and HSLA steels) are expected to influence elastic recovery mechanics. Another level of complexity (and uncertainty) is introduced by the realization that post-forming residual stress distributions depend highly upon the deformation mode (strain path). Springback itself is expected to be a directional property in the presence of deformation-induced residual stresses. In real world situations, where sheet metal is fabricated into three-dimensional shapes, the distribution of residual stresses in DP

steels, and the associated effects on springback, would likely become exceedingly complex. The results of this analysis suggest that deformation-induced internal stresses must be considered in any material model used to predict and understand springback displacements. The respective analyses of Zhongua and Haicheng (16) and of Sugimoto *et al*. (65) are certainly good benchmarks for the development of advanced material models that are capable of addressing the effects of stress and strain partitioning in DP steels and other multi-phase advanced high strength steels.

6.4.3 **In-Service Performance**

It was shown in Figure 71 through Figure 73 that conventional effective strain models (*e.g.*, that based on the Tresca yield criterion) are incapable of predicting tensile yield strength evolution in deformation modes other than uniaxial tension. Factors such as intrinsic anisotropy (associated with annealing texture and microstructural variations, for example), evolution of deformation textures, dislocation interactions (*e.g.*, latent work hardening), and deformation-induced residual stresses, must all be taken into account when constructing an appropriate constitutive material model. More importantly however, in the context of this research program, is the observation that conventional effective strain models tend to over predict the post-forming tensile yield strength of DP steels, while they under predict the post-forming tensile yield strength of conventional steels (*e.g.*, the IF steel and the HSLA steel). The implication is that the post-forming yield strength of a component made from DP steel may be lower than expected from experience based on conventional high strength steel behavior. From a practical standpoint, automotive design engineers need to consider not only incoming materials properties (before forming) but also final part strength (after forming)—especially for load-bearing structural components, for example. Additionally, as residual stresses generally are known to have a

profound effect on fatigue performance (77), it is foreseeable that deformation-induced residual stresses affect the in-service fatigue performance of DP steels (and of other steels—to a lesser extent).

7.0 CONCLUSIONS

The primary objective of this research program was to understand the influence of deformation-induced residual stresses on the post-forming tensile stress/strain behavior of dual-phase (DP) steels. The following commercially produced materials were included in the analysis: 1) a DP steel with approximately 15 vol. % martensite, 2) a conventional high-strength, low-alloy (HSLA) steel, and 3) a conventional, ultra-low-carbon interstitial-free (IF) steel.

Samples of each material were prestrained to various levels in the uniaxial tension (UT), plane strain (PS) and balanced biaxial stretching (BB) prestrain modes, where the major strain axis (ε_{maj}) was aligned in the longitudinal (L) direction (sheet rolling direction), and the minor strain axis (ε_{min}) was aligned in the sheet transverse (T) direction. For each prestrain condition, the post-forming tensile stress/strain behavior was examined in L-direction and T-direction tensile tests. Additionally, for each material, neutron diffraction residual stress measurements were made in the 5% major strain condition ($\varepsilon_{maj} = 0.05$) for the UT, PS and BB prestrain modes. The following major conclusions were drawn from this analysis.

- Neutron diffraction experiments confirmed the presence of large post-forming deformation-induced residual stresses in the ferrite phase of the DP steel.
- The deformation-induced residual stress state in the ferrite phase of the DP steel depends upon the prestrain mode, where the principal residual stress components are

generally proportional to the principal strain components of the prestrain, but opposite in sign.

- Deformation-induced residual stresses greatly affect the post-forming tensile stress/strain behavior of DP steels.
- As previously reported in the literature, the formability (residual tensile ductility) of the IF steel and the HSLA steel was adversely affected by strain path changes.
- The DP steel displays an advantage over the conventional IF and HSLA steels, in terms of post-forming residual tensile ductility and is expected to be particularly well suited for complex forming operations that involve abrupt strain path changes.
- For the UT and PS prestrain modes, the IF, HSLA and DP steels exhibit directional (anisotropic) hardening behavior, where the post-forming tensile yield strength is different in the L and T directions (parallel and perpendicular to the major prestrain axis, respectively).
  - The DP steel exhibits cross-softening behavior, where the post-forming tensile yield strength is lower in the T-direction (perpendicular to the major strain). The degree of cross-softening increases as prestrain increases, and is more pronounced for the UT prestrain mode.
  - The IF steel and the HSLA steel exhibit cross-hardening behavior, where the post-forming tensile yield strength is higher in the T-direction (as reported previously for other conventional steels). The degree of cross-hardening increases as prestrain increases, and is more prominent for the PS prestrain mode.
- The IF, HSLA and DP steels exhibit nearly isotropic hardening behavior for the BB prestrain mode—a reflection of the symmetry of the prestrain mode.

- Two distinct types of post-forming tensile stress-strain behavior were observed:
  - Type 1 Tensile Behavior – "Normal" stress/strain behavior where the total elongation is more or less comprised of similar contributions of uniform and post-uniform elongation.
  - Type 2 Tensile Behavior – Characterized by grossly unbalanced contributions of uniform and post-uniform elongation, where the ultimate tensile strength occurs at a very low strain value.
- The DP steel showed Type 1 behavior for all prestrain conditions, in both L-direction and T-direction tensile tests.
- The IF and HSLA steels exhibited Type 1 and Type 2 behavior—depending on the amount of prestrain, the prestrain mode, and the tensile test direction. The tendency toward Type 2 tensile stress/strain behavior increases as the amount of prestrain increases and the minor strain (ε_{min}) increases (for a given major strain, ε_{maj}). Type 2 behavior is more prominent in T-direction (orthogonal) tensile tests.
- Deformation-induced residual stresses were measured in the IF steel and the HSLA steel; however, the magnitudes of which are such that post-forming tensile stress/strain behavior is not significantly affected.
- The IF steel and the HSLA steel showed remarkably similar post-forming stress/strain behavior for all prestrain modes considered. This observation is especially remarkable considering the vast differences in mechanical properties (including anisotropy), microstructure, and composition between the two steels.

REFERENCES

1. S. Hayami and T. Furukawa, "A Family of High-Strength, Cold-Rolled Steels," Proceedings of Micro Alloying '75, Union Carbide Corp., New York, 1977, pp. 311-321.

2. Formable HSLA and Dual-Phase Steel, Conference Proceedings (Chicago, 1977), A.T. Davenport, ed., Met. Soc. of AIME, New York, 1979.

3. Structure and Properties of Dual-Phase Steels, Conference Proceedings (New Orleans, 1979), R.A. Kot and J.W. Morris, eds., Met. Soc. of AIME, New York, 1979.

4. Fundamentals of Dual-Phase Steels, Conference Proceedings (Chicago, 1981), R.A. Kot and B.L. Bramfitt, eds., Met. Soc. of AIME, New York, 1981.

5. Technology of Continuously Annealed Cold-Rolled Sheet Steel (Detroit, 1984), R. Pradhan, ed., Met. Soc. of AIME, New York, 1985.

6. R.W.K. Honeycombe, Steels: Microstructure and Properties, ASM, 1982.

7. Dr. J.D. Defilippi, United States Steel Corporation, Research & Technology Center, Monroeville, Pennsylvania, Personal Communication.

8. Prof. A.J. DeArdo, University of Pittsburgh, Personal Communication

9. G.R. Speich and R.L. Miller, "Mechanical Properties of Ferrite-Martensite Steel," in Ref. 3, pp. 145-182.

10. N.K. Balliger and T. Gladman, "Work Hardening Behavior of Dual-phase Steels," *Metal Science*, vol. 15, March 1981, pp. 95-108.

11. D.K. Matlock, G. Krauss, L.F. Ramos and Glenn S. Huppi, "A Correlation of Processing Variables with Deformation Behavior of Dual-Phase Steels," in Reference 3, pp. 62-90.

12. S. Sadagopan, C. Wong, M. Huang, B. Yan and D. Urban, Formability Characterization of a New Generation of High Strength Steels, AISI, March 2003.

13. K. Sugimoto, M. Kobayashi, S. Yasuki and S. Hashimoto, "Influence of Deformation Temperature on the Bauschinger Effect of a TRIP-Aided Dual-Phase Steel," *Met. Trans. JIM*, vol. 36, no. 5, 1995, pp. 632-638.

14. A.M. Streicher, Examination Using X-Ray Diffraction of the Forming Response of Ferrite and Austenite in a TRIP Sheet Steel, Master of Science Thesis, Colorado School of Mines, November 2002.

15. K. Sugimoto, M. Kobayashi, H. Matsushima and S. Hashimoto, "X-Ray Residual Stress and Strain-Induced Transformation of Retained Austenite in a TRIP-Aided Dual-phase Steels," *Trans. Japan Soc. Mech. Eng.*, vol. 61, no. 581, 1995, pp. 80-86.

16. L. Zhonghua and G. Haicheng, "Bauschinger Effect and Residual-phase Stresses in Two Ductile-Phase Steels: Part I and Part II," *Met. Trans. A*, vol. 21A, March 1990, pp. 717-724, and 725-732.

17. M.F. Ashby, "Deformation of Plastically Non-Homgeneous Materials," *Phil. Mag.*, vol. 21, no. 170, 1970, pp. 399-424.

18. J. Gerbase, J.D. Embury and R.M. Hobbs, "The Mechanical Behavior of Some Dual-phase Steels – With Emphasis on the Initial Work Hardening Rate," in Reference 3, pp. 118-144.

19. S.S. Hansen and R.R. Pradhan, "Structure/Property Relationships and Continuous Yielding Behavior in Dual-phase Steels," in Reference 4, pp. 113- 144.

20. G.T. Hahn, "A Model for Yielding with Special Reference to the Yield-Point Phenomena of Iron and Related BCC Metals," *Acta Met.*, vol. 10, 1962, pp. 727-738.

21. A.H. Cottrell, Report of the Bristol Conference on Strength of Solids, Physical Society, London, 1948, p. 30.

22. M.S. Rashid, "Relationhsip between Steel Microstructure and Formability, in Reference 2, pp. 1-24.

23. A.F. Crawley, M.T. Shehata, N. Pussegoda, "Processing, Properties and Modelling of Experimental Batch-Annealed Dual-Phase Steels," in Reference 4, pp. 181-197.

24. G.R. Speich, "Physical Metallurgy of Dual-Phase Steels," in Reference 4, pp. 3-45.

25. R.G. Davies and C.L. Magee, "Physical Metallurgy of Automotive High Strength Steels," in Reference 3, pp. 1-19.

26. J.M. Rigsbee, P.J. VanderArend, "Laboratory Studies of Microstructures and Structure-Property Relationships in Dual-Phase Steels," in Reference 2, pp. 56-86.

27. W.R. Cribb and J.M. Rigsbee, "Work-Hardening Behavior and Its Relationship to the Microstructure and Mechanical Properties of Dual-Phase Steels," in Reference 3, pp. 91-117.

28. P.E. Repas, "Physical Metallurgy of Dual-Phase Steels, in Mechanical Working and Steel Processing Conference XVII, AIME, New York, 1979, pp. 277-305.

29. J.J. Jonas and R.A. Nascimento, "Effect of Deformation on the γ to α Transformation in Two High Silicon Dual-Phase Steels," in Reference 4, pp. 95-112.

30. J. Becker and E. Hornbogen, "Microscopic Analysis of the Formation of Dual-Phase Microstructures," in Reference 3, pp. 20-39.

31. J. Becker, E. Hornbogen and F. Wendl, "Analysis of Mechanical Properties of a Low-Alloyed Mo-Steel with Differenct Phosphorous Additions," in Reference 4, pp. 383-398.

32. A.M. Sherman, R.G. Davies, W.T. Donlon, "Electron Microscopic Study of Deformed Dual-Phase Steels," in Reference 4, pp. 85-94.

33. T. Furukawa, H. Morikawa, H. Takechi and K. Koyama, "Process Factors for Highly Ductile Dual-Phase Sheet Steels," in Reference 3 pp. 281-303.

34. J.M. Rigsbee, J.K. Abraham and A.T. Davenport, "Structure-Processing and Structure-Property Relationships in Commercially Processed Dual-Phase Steels," in Reference 3, pp. 304-329.

35. A.R. Marder, "Factors Affecting the Ductility of 'Dual-Phase' Alloys," in Reference 2, pp. 87-98.

36. I.Y. Pychmintsev, R.A. Savrai and B.D. De Cooman, "Effect of Stress State on the Transformation Behaviour and Mechanical Properties of TRIP-Aided Automotive Sheet Steels," International Conference on TRIP-Aided High Strength Ferrous Alloys, Conference Proceedings, 2002, pp. 79-84.

37. R. Pradhan, "Metallurgical Aspects of Quenched and Tempered Dual-Phase Steels Produced via Continuous Annealing," in Reference 5 , pp. 297-317.

38. D. Tseng an F.H. Vitovec, "The Bauschinger Effect and Workhardening of Dual-Phase Steel," in Reference 4, pp. 399-411.

39. R.D. Lawson, D.K. Matlock and G. Krauss, "The Effect of Microstructure on the Deformation Behavior and Mechanical Properties of a Dual-Phase Steel," in Reference 4, pp. 347-381.

40. Tamura, Y. Tomata, A. Akao, Y. Yamaoha, M. Ozawa and S. Kanotoni, "On the Strength and Ductility of Two-Phase Iron Alloys," *Trans. ISIJ*, vol. 13, 1973, pp. 283-292.

41. Tamura, Y. Tomota, H. Ozawa, "Strength and Ductility of Fe-Ni-C Alloys Composed of Austenite and Martensite with Various Strengths," in Proceedings fo the 3rd International Conference on the Strength of Metals and Alloys, Cambridge, vol. 1, 1973, pp. 611-615.

42. W.C. Leslie, R.J. Sober, "The Strength of Ferrite and of Martensite as Functions of Composition, Temperature, and Strain Rate," *Trans. ASM*, vol. 60, 1967, pp. 459-484.

43. P.R. Rios, J.R.C. Guimarães and K.K. Chawla, "Modelling the Stress-Strain Curves of Dual-Phase Steels," *Scripta Met.*, vol. 15, 1981, pp. 899-904.

44. Y.W. Chang and R.J. Asaro, "Bauschinger Effects and Work Hardening in Shperoidized Steels," *Metal Science*, vol. 12, 1978, pp. 277-284.

45. L.M. Brown and W.M. Stobbs, "Work Hardening of Copper Silica—Role of Plastic Relaxation," *Phil. Mag.*, vol. 23, 1971, pp. 1201-1233 and vol. 34(3), 1967, pp. 351-372.

46. M.F. Ashby, Strengthening Mechanisms of Crystals, A. Kelly and R.B. Nicholson, eds., Elsevier, London, 1971.

47. G.R. Speich, U.S. Steel Research Center, Monroeville, PA, Personal Communication (Cited in Reference 18).

48. J.D. Embury, J.L. Duncan, "Formability of Dual-Phase Steels," in Reference 4, pp. 333-345.

49. J. Bauschinger, *Zivilingur (Civilingenieur)*, vol. 27, 1881, pp. 289-347.

50. E. Orowan, Internal Stresses and Fatigue of Metals, Elsevier, New York, 1959.

51. L. Duprez, B.C. DeCooman and N. Akdut, "High-Temperature Stress and Strain Partitioning in Duplex Stainless Steel," *Zeitschrift fur Metallkunde*, vol. 93, no. 3, March 2002, pp. 236-243 (pre-print).

52. K.-I. Sugimoto, M. Kobayashi, H. Matsushima and S.-I. Hashimoto, "X-Ray Residual Stress and Strain-Induced Transformation of Retained Austenite in TRIP-aided Dual-Phase Steels," *Trans. Jap. Soc. of Mech. Eng., Part A*, vol. 61, no. 581, 1995, pp. 80-86.

53. K.C. Chan and W.B. Lee, "A Theoretical Prediction of the Strain Path of Anisotropic Sheet Metal Deformed under Uniaxial and Biaxial Stress State," *Int. J. Mech. Sci.*, vol. 12, no. 6, 1990, pp. 497-511.

54. J.H. Chung and D.N. Lee, "Effects of Changes in Strain Path on the Anisotropy of Yield Stresses of Low-Carbon Steel and 70-30 Brass Sheets," *J. of Mat. Sci.*, vol. 28, 1993, pp. 4704-4712.

55. F.J. Humphreys and M. Hatherly, Recrystallization and Related Annealing Phenomena, Pergamon Press, Elsevier Science Ltd., Oxford, 1996.

56. A.B. Lopes, F. Barlat, J.J. Gracio, J.F. Ferreira Duarte and E.F. Rauch, " Effect of Texture and Microstructure on Strain Hardening Anisotropy for Aluminum Deformed in Uniaxial Tension and Simple Shear," *Int. J. Plasticity*, vol. 19, 2003, pp. 1-22.

57. Y. Bergstrom and S. Olund, "The Forming Limit Diagram of Sheet Metals and Effects of Strain Path Changes on Formability: A Dislocation Treatment," *Mat. Sci. Eng.*, vol. 56, 1982, pp. 47-61.

58. Prof. H.R. Piehler, Carnegie-Mellon University, Personal Communication.

59. T. Kikuma, K. Nakazima, "Effects of Deforming Conditions and Mechanical Properties on the Stretch Forming Limits of Steel Sheets," *Trans. ISIJ*, vol. 11, 1971, pp. 827-832.

60. F. Ronde-Oustau and B. Baudelet, "Microstructure and Strain Path in Deep Drawing," *Acta Met.*, vol. 25, 1977, pp. 1523-1529.

61. B.M. Hance, Effects of Strain Path on Formability and Microstructural Evolution in Low-Carbon Sheet Steel, Master of Science Thesis, Colorado School of Mines, September 1996.

62. B. Yan, P. Belanger and K. Citrin, "Effect of Forming Strain on Fatigue Performance of a Mild Automotive Steel," *SAE Technical Paper Series*, no. 2001-01-0083, 2001.

63. S. Toyoda, Y. Kawabata, K. Sujuki, K. Sakata, S. Yabumoto, M. Gunji and A. Sato, "Effects of Microstructure and Aging Property on Formability in ERW Steel Tubes for Automobile Structural Parts," *SAE Technical Paper Series*, no. 2004-01-0829, 2004.

64. T. Hasebe, "Cross Hardening Effect of IF Steels," IF Steels 2003, Proceedings of the International Forum for the Properties and Application of IF Steels, H. Takechi, ed., Tokyo, ISIJ, May 2003, pp. 128-137.

65. K. Sugimoto, T. Sakaki, O. Miyagawa and H. Kuramoto, "Mechanical Anisotropy of Prestrained Sheets of a Dual-Phase Steel," HSLA Steels: Metallurgy and Applications, Proceedings of the International Conference on HSLA Steels '85, J.M. Gray, T. Ko, Z. Shouhua, W. Baorong and X. Xishan, eds., Beijing, ASM International, November 1985, pp. 809-816.

66. A. Wasilkowska, W. Loos, C. Krempaszky, E.A. Werner, R. Petrov, S. Traint and A. Pichler, "Plastic Anisotropy of TRIP-aided Steel Sheets Induced by Prestraining," in Proceedings of Mechanical Engineering '04, Varna, Bulgaria, September 2004, Preprint—publisher and pages unknown.

67. P. Van Houtte, S. Hiwatashi, E. Hoferlin, B. Peeters and C. Teodosiu, " Physics-Based Material Modelling of the Deformation Process in Deep Drawing of IF Steel," IF Steels 2003, Proceedings of the International Forum for the Properties and Application of IF Steels, H. Takechi, ed., Tokyo, ISIJ, May 2003, pp. 82-91.

68. A.B. Lopes, E.F. Rauch and J.J. Gracio, "Textural vs Structural Plastic Instabilities in Sheet Metal Forming," *Acta Mater*., vol. 47, no. 3, 1999, pp. 859-866.

69. J.V. Sharp and M. Makin, "Slip Behavior in Copper Crystals previously Deformed on another Slip System," *Can. J. Phys*., vol. 45, 1967, pp. 519-522.

70. E.F. Rauch and C. G'Sell, "Flow Localization Induced by a Change in Strain Path in Mild Steel," *Mat. Sci. Eng. A*, vol. A111, May 1989, pp. 71-80.

71. B. Bacroix, E. Nesterova and C. Teodosiu, "Relationships between Deformation Microstructures and Grain Orientations in Low Carbon Steels Subjected to Strain-Path Changes," Plasticity, Damage and Fracture at Macro, Micro and Nano Scales, Proceedings of Plasticity '02, A.S. Khan and O. Lopez-Pamies, eds., NEAT Press, 2002, pp. 292-294.

72. E.V. Nesterova, B. Bacroix and C. Teodosiu, "Microstructure and Texture Evolution under Strain-Path Changes in Low-Carbon Interstitial-Free Steel," *Met. Mat. Trans. A*, vol. 32A, October 2001, pp. 2527-2538.

73. G. Vincze, E.F. Rauch, J.J. Gracio, F. Barlat and A.B. Lopes, "A Comparison of the Mechanical Behaviour of an AA1050 and a Low Carbon Steel Deformed under Strain Reversal," *Acta Mat.*, vol. 53, 2005, pp. 1005-1013.

74. E.F. Rauch, "The Relationship between Dislocation Substructure and Mechanical Behavior for a Low Carbon Steel," *La Revue de Métallurgie-CIT/Science et Génie Matériaux*, September 1997, pp. 1030-1036.

75. Z. Jeffries, "Grain Size Measurements," Chem. & Met. Eng., vol. 18, 1918, pp. unknown.

76. F.B. Pickering, Physical Metallurgy and Design of Steels, Applied Science Publishers, Ltd., London, 1978.

77. G.E. Dieter, Mechanical Metallurgy, 3rd Edition, McGraw-Hill, New York, 1986.

78. M.G. Stout and A.D. Rollett, "Large-Strain Bauschinger Effects in FCC Metals and Alloys," Met. Trans. A, vol. 21A, December 1990, pp. 3201-3213.

79. C. Hammond, The Basics of Crystallography and Diffraction, Oxford University Press, Oxford, UK, 1998.

80. Dr. Henry J. Prask and Thomas Gnaupel-Herold, NIST Center for Neutron Research, Gaithersburg, Maryland, Personal Communication.

81. P.J. Withers and H.K.D.H. Bhadeshia, "Residual Stress, Part 1 – Measurement Techniques," *Mat. Sci. Tech.*, vol. 17, April 2001, pp. 355-365.

82. C. O. Ruud, "Residual Stress Measurements," in ASM Handbook, ASM International, vol. unkown, date unknown.

83. S.L. Semiatin and J.J. Jonas, Formability and Workability of Metals—Plastic Instability & Flow Localization, ASM, Metals Park, OH, 1984.

84. W.F. Hosford, R.M. Caddell, Metal Forming—Mechanics and Metallurgy, Prentice-Hall, Englewood Cliffs, NJ, 1983.

85. T.B. Stoughton, "The Influence of Material Model on the Stress-Based Forming Limit Criterion," *SAE Technical Paper Series*, no. 2002-01-0157, 2002.

86. D. Banabic, O. Cazacu, F. Barlat, D.-S. Comsa, S. Wagner and K. Seigert, "Recent Anisotropic Yield Criteria for Sheet Metals," *Proc. Romanian Acad. A*, vol. 3, no. 3, 2002, pp. 1-9.

87. Z. Mroz, "On the Description of Anisotropic Workhardening," *J. Mech. Phys. Solids*, vol. 15, 1967, pp. 163-175.

88. R.M. Cleveland and A.K. Ghosh, "Inelastic Effects on Springback in Metals," *Int. J. Plasticity*, vol. 18, 2002, pp. 769-785.

89. M.-G. Lee, D. Kim, C. Kim, M.L. Wenner, R.H. Wagoner and K. Chung, "Spring-back Evaluation of Automotive Sheets Based on Isotropic-Kinematic Hardening Laws and Non-Quadratic Anisotropic Yield Functions, Part II: Characterization of Material Properties," *Int. J. Plasticity*, vol. 21, 2005, pp. 883-914.

90. X.M. Chen and S.D. Liu, "Experimental and Simulation Study on Tube Bending and Hydroforming," *SAE Technical Paper Series*, no. 200-01-1114, 2000.